Enhancing the Power Density of Bearingless Slice Motors Through Custom Power Electronics and Control Strategies

by

Hosam Ibrahim

BASc., The University of British Columbia, 2021

A THESIS SUBMITTED IN PARTIAL FULFILLMENT OF

THE REQUIREMENTS FOR THE DEGREE OF

MASTER OF APPLIED SCIENCE

in

The Faculty of Graduate and Postdoctoral Studies

(Mechanical Engineering)

THE UNIVERSITY OF BRITISH COLUMBIA

(Vancouver)

August 2023

The following individuals certify that they have read, and recommend to the Faculty of Graduate and Postdoctoral Studies for acceptance, the thesis entitled:

Enhancing the Power Density of Bearingless Slice Motors Through Custom Power Electronics and Control Strategies

submitted by **Hosam Ibrahim** in partial fulfilment of the requirements for the degree of **Master of Applied Science** in **Mechanical Engineering**

Examining Committee:

Ryozo Nagamune, Professor, Mechanical Engineering, UBC
Co-supervisor

Minkyun Noh, Professor, Mechanical Engineering, KAIST
Co-supervisor

Yusuf Altintas, Professor, Mechanical Engineering, UBC
Supervisory Committee Member

Boris Stoeber, Professor, Mechanical Engineering, UBC
Supervisory Committee Member

Abstract

Bearingless motors are an emerging class of electric machines that combines the functionality of an active magnetic bearing (AMB) and an electric motor into the same stator structure. This integration benefits from the advantages of AMBs while addressing their shortcomings, resulting in more compact magnetically levitated systems with reduced system complexity and cost. However, despite these advantages, the relatively low power density of bearingless motors has primarily limited their use to research settings and niche applications with low power demands.

The operation of a bearingless motor necessitates the generation of two distinct field components in the airgap for torque and radial force generation. Traditionally, this was achieved using separate suspension and torque windings. However, this results in an inefficient winding volume utilization and reduced power density. Consequently, a shift has emerged towards combined windings, utilizing the same windings for both suspension and rotation. This is achievable through the use of multiphase windings, offering additional degrees of freedom to simultaneously generate torque and suspension forces.

To support research on multiphase bearingless motors and exploit the advantages of combined windings, we develop a custom multiphase motor control platform that integrates the controller, sensor interface, and power electronics into a reconfigurable system. The design consists of a two-level twelve-leg inverter with isolated inline shunt-based phase current sensing and isolated DC bus voltage sensing. A 12-phase inverter is realized using GaNFET-based half-bridge power stages. The DC bus voltage and the phase currents are measured using isolated delta-sigma modulators. An FPGA is used to implement a sophisticated motor control algorithm with high temporal determinism.

The performance of the motor drive is evaluated with a homopolar bearingless motor prototype. Development of the drive enables the use of custom control strategies, such as sensorless control, which allows the prototype mo-

tor to operate up to its rated speed (36000 r/min) as limited by the available DC link voltage (30 V). This represents an almost fourfold increase in the maximum no-load speed of 9500 r/min reached when using off-the-shelf power electronics and a DC link voltage of 48 V.

Lay Summary

Bearingless motors incorporate the functionality of magnetic bearings into an electric motor in a compact form factor. This versatile technology finds applications across a wide speed range owing to its contact-free operation, and high levels of reliability. Examples of mature applications for bearingless motors include the development of ultra-pure fluid handling pumps and artificial hearts.

The objective of this research project is to develop a custom prototyping platform for bearingless motor research. This platform serves as a foundation for exploring and implementing novel control strategies to maximize the power density of bearingless motors. Power density, a key performance metric, refers to the amount of power that can be delivered by a motor relative to its size and weight. Enhancing the power density of bearingless motors results in more compact and efficient designs, enabling their use in a wider range of applications.

Preface

This thesis is the original, unpublished, independent work by the author Hosam Ibrahim.

A condensed version of Chapters 3 and 4 has been accepted for presentation as follows

H. Ibrahim, R. Nagamune, and M. Noh, "FPGA-based Multi-phase Motor Control Platform for Bearingless Motor Research," 2023 IEEE Energy Conversion Congress and Exposition (ECCE), Nashville, TN, USA, 2023

Table of Contents

List of Tables

List of Figures

Acknowledgements

I would like to express my gratitude to my supervisor, Dr. Minkyun Noh, for his guidance, and support throughout my research. I am grateful for his expertise, patience, and for all the time he dedicated to helping me even after accepting a new position at KAIST.

I would also like to thank Dr. Ryozo Nagamune for agreeing to supervise my research following Dr. Noh's departure and for always providing valuable feedback and suggestions to improve my work.

I am also grateful to my lab mates, who provided me with fun company and valuable insights throughout my degree.

Finally, I would like to thank my family, who have been a constant source of love, encouragement, and support throughout my academic journey.

Chapter 1

Introduction

1.1 Background

Mechanical contact-type bearings are typically responsible for the majority of maintenance issues in motor drive systems. These bearings require regular lubrication, are susceptible to wear and failure, and necessitate periodic replacement, leading to increased maintenance costs and downtime. These limitations become more pronounced at high rotational speeds where exposure to significant mechanical stresses greatly limits the operational lifetimes of a machine. Additionally, the use of bearing lubricants poses certain limitations on the applications of mechanical bearings. In many industries, especially those requiring high purity or exposure to corrosive and toxic chemicals, the presence of lubricants is deemed unacceptable due to the risks of contamination. These shortcomings highlight the need for alternative solutions that offer improved reliability and reduced maintenance requirements.

To address these limitations, alternative bearing technologies such as active magnetic bearings (AMBs) have emerged. An AMB works by actively generating electromagnetic forces to suspend and control the rotor in a closed-loop feedback scheme. By eliminating mechanical contact and the associated lubrication requirements, these systems offer advantages in terms of maintenance, cleanliness, and high-speed capabilities making them suitable for applications where mechanical bearings face inherent limitations. AMBs have been successfully deployed in various applications across a wide range of speed and power requirements. Some examples include use cases in gas turbine engines, high-speed machine tools, flywheel energy storage, and compressors for natural gas transportation, wastewater aeration, and HVAC systems [15, 18, 29].

However, AMBs do have certain drawbacks, such as their size, cost, complexity, and low radial force density compared to traditional mechanical

bearings [9]. A typical arrangement of a magnetically levitated rotating shaft is depicted in Figure 1.1a. Two radial AMBs and an axial AMB are used for supporting shaft loads and a separate electric motor is used for torque generation. Each AMB requires dedicated custom power electronics and occupies a significant portion of the shaft length to produce sufficient radial forces. This limits their practicality in certain applications.

To address these challenges, bearingless motors have emerged as a promising solution. Bearingless motors are an emerging class of electric machines that combines the functionality of an active magnetic bearing (AMB) and an electric motor into the same stator structure. The integration of the two technologies offers the advantages of AMBs such as contact-free operation and the ability to monitor and actively alter rotor dynamics while addressing its shortcomings. By leveraging the motor's preexisting magnetic field for generating suspension forces, bearingless motors can replace the function of one or more AMBs. Figure 1.1b illustrates a magnetically levitated system where the function of the radial AMBs and conventional motor is fulfilled by bearingless motors resulting in a more compact design with reduced system complexity and cost. Moreover, bearingless motors can be powered using readily available motor drives and benefit from well-established control techniques, facilitating their widespread adoption in various applications.

Bearingless motors are a versatile technology that finds applications across a wide speed range due to their contact-free operation. At low speeds, bearingless motors have found uses in blood pumps [24], artificial hearts [1], and mixers/stirrers in the chemical and pharmaceutical industries [81]. These applications make use of the bearingless motor's inherent ability to create hermetically sealed systems without the need for seals or lubricants. This is particularly useful in applications requiring high levels of purity or where exposure to corrosive and toxic chemicals is a concern as it eliminates the risk of contamination from lubricants or the potential failure of mechanical seals.

At high speeds, the elimination of mechanical contact and its associated drawbacks such as friction, wear, frequent maintenance, and reliability concerns opens up opportunities for the increased adoption of magnetically levitated systems in various applications. Bearingless motors with rotor speeds exceeding 100 kRPM have been reported in [44, 62] with a maximum reported speed of 500 kRPM in [4]. Target applications for the developed motors include centrifuges, high-speed spindle tools, and optical scanning systems. However, despite these breakthroughs in speed, bearingless mo-

(a)

(b)
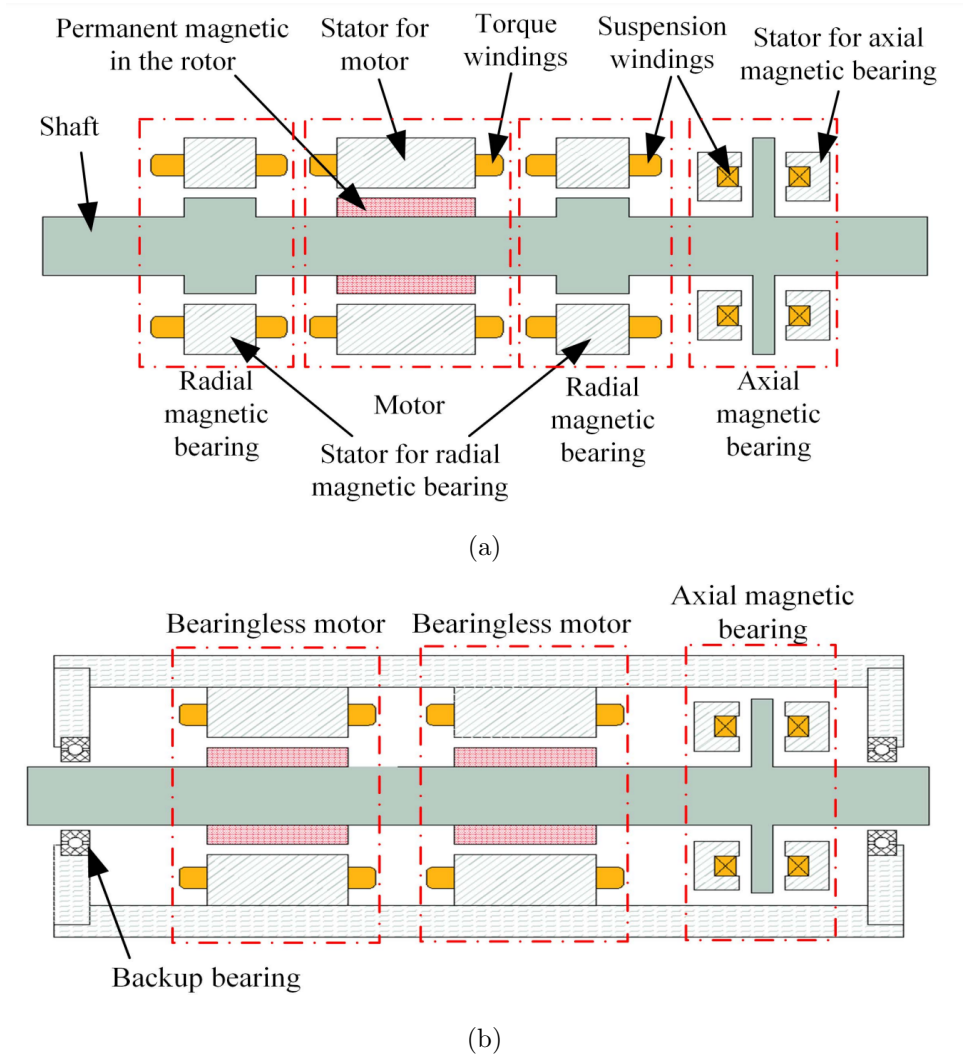
Figure 1.1: Comparison of a magnetically levitated shaft supported by (a) AMBs and (b) bearingless motors in conjunction with axial AMB [61].

tors have been primarily limited to research settings and niche applications with low power demands.

While a few experimental studies have demonstrated high-power bearingless motors exceeding 10 kW [36, 48], the current state of the art does not yet meet the power requirements and efficiencies necessary for widespread industrial adoption. In reference [11], the authors investigate the potential of bearingless motors to complement or even replace AMBs in transportation and industrial applications and highlight some of the challenges associated with developing bearingless motors for high-power applications and recent advancements made toward addressing these challenges.

Nonetheless, ongoing research and technological advancements are continuously pushing the boundaries of bearingless motor technology. As the field evolves, it holds the potential to revolutionize various industries by enabling the development of more efficient, reliable, and high-performance machines.

The remainder of this section serves to provide a review of some of the relevant literature and recent trends and developments in technologies applicable to this research project and highlight research gaps that remain unexplored.

1.1.1 Multiphase Machines

The past few years have seen an increase in the adoption of multiphase machines in a variety of applications. Compared to their three-phase counterparts multiphase machines offer a number of added benefits such as a reduction in the amplitude of torque pulsations and the distribution of power across more phases resulting in an improved power density [59] and reduced power switch ratings. Moreover, the added number of phases not only provides some redundancy enabling fault-tolerant operation for safety-critical applications but also offers additional electrical degrees of freedom. These extra degrees of freedom have been harnessed for various secondary purposes, such as torque enhancement through the injection of higher-order stator current harmonics for machines with concentrated windings [60], the control of multiple machines using a single multiphase inverter [33], and for controlling bearingless motors [51].

All these distinct advantages have attracted significant interest and research into the area of multiphase machines where several survey papers [3, 17, 33] have been published on the topic, covering topics like modeling, control, and the applications of multiphase drives.
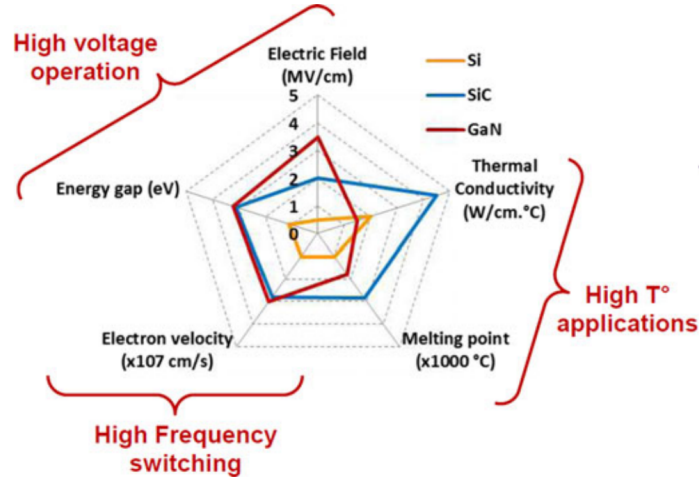
Figure 1.2: Summary of relevant material properties for wide bandgap technologies compared to silicon [43].

1.1.2 Wide Bandgap Devices

As silicon-based power devices reach a point of technological maturity characterized by marginal advancements and incremental improvements over time, there is an increasing demand for new and improved technologies to meet the high power and efficiency requirements of modern systems. Wide bandgap semiconductors such as gallium nitride (GaN) and silicon carbide (SiC) have emerged as promising alternatives capable of outperforming silicon-based devices owing to their superior material properties.

As the name suggests, wide bandgap semiconductors are characterized by a large bandgap and high electron mobility compared to conventional silicon semiconductors. These characteristics directly translate to higher voltage-blocking capabilities, higher operating temperatures, faster switching speeds, and reduced losses. These advantages allow power switches to be more compact and run cooler and faster, resulting in cost savings and improved power densities. A summary of relevant material properties for wide bandgap technologies compared to silicon is compared in Figure 1.2.

Wide bandgap technologies, although still in their early stages of development, hold immense potential for further advancements. Harnessing the capabilities of these semiconductors can result in significant energy savings in industrial processing and consumer appliances, promote the widespread

adoption of electric vehicles [47], and facilitate the integration of renewable energy sources into the electric grid [22].

Moreover, in the context of bearingless motors, the introduction of commercial wide-bandgap semiconductor switching devices enables motor drives to efficiently operate at higher fundamental frequencies. This capability allows motor designs to feature a higher number of poles, facilitating higher rotational speeds and power densities.

1.1.3 Bearingless Motors

The concept of a bearingless motor was first proposed in the late 1980s. Since then, fueled by developments in vector control theory, digital signal processing, and power electronics, bearingless motor technology has undergone significant advancements and has attracted attention from researchers and industry professionals, leading to further innovations and improvements in the field. The key theoretical concepts and principles of bearingless motors are summarized in two textbooks [14, 40].

Bearingless motors have been realized using various motor architectures, including hysteresis [54], switched reluctance [74], synchronous including both synchronous reluctance [69], and permanent magnet [37, 52, 73] types, and induction motors [82]. Among these, the permanent magnet bearingless machine has received the most research attention owing to its high efficiencies, power densities, and simplified control. In this thesis, we restrict our discussion to bearingless synchronous machines. Next, we discuss different categories of bearingless motors to provide the necessary background for the remainder of the thesis.

Combined and Separated Windings

The operation of a bearingless motor requires the creation of two different field components in the airgap, a p-pole pair field and a p_s-pole pair field. The p-pole pair field corresponds to the number of rotor poles and is used for generating torque, and a p_s-pole pair field is used for generating the radial suspension force. These two distinct fields can be generated using different winding schemes which can be broadly divided into two major categories: separated windings and combined windings.

Traditionally, bearingless motors have employed two separate sets of three-phase windings dedicated exclusively to generating torque or suspension forces. Despite being easier to control, as it physically decouples the torque

6

and suspension force regulation, multiple publications have pointed out that such a separated winding scheme leads to an inefficient winding volume utilization and a subsequent reduction in power density [16, 63]. Typically machines with separated windings reserve 25-40% of the available stator slot space for suspension windings despite using less than 5% during normal operation [48, 68]. This design approach incorporates a safety margin to account for worst-case conditions occurring during initial rotor takeoff which require large suspension currents.

Due to these shortcomings, there is a growing trend towards a combined winding scheme that uses the same set of winding for both suspension and rotation. Such a winding configuration leads to simpler manufacturing, reduced copper losses, and improved power densities by enabling the full utilization of the available stator winding slot space during operation. By using a combined winding, we are able to eliminate the slot space design tradeoff by dynamically allocating slot space to levitation or torque during runtime, leading to improved performance and more compact motor designs. However, to the best of our knowledge, such an allocation procedure has not been explored in the literature. In this research, we aim to propose an allocation procedure that prioritizes the safety-critical suspension performance of the machine.

Combined windings are broadly categorized into multiphase combined windings and dual purpose no voltage (DPNV) windings. Multiphase combined windings, also referred to as "split windings" [14], utilize the additional degrees of freedom offered by multiphase machines to simultaneously generate both torque and suspension field components.

However, an inherent limitation of the multiphase combined winding scheme is that the rotation-induced back emf lowers the available differential voltage margin for regulating suspension currents at high speeds. This may compromise the stability of the rotor suspension potentially leading to touchdowns during operation. To overcome this problem [67] proposes a "Dual Purpose No Voltage" winding scheme which aims at canceling out the effects of the rotation-induced back emf seen by the suspension terminals, allowing for the reduction of the DC bus voltage requirement. Two main variations of this winding scheme exist in the literature: bridge winding configuration [31] and parallel winding configuration [56]. Despite its advantages, this winding scheme increases the hardware complexity and requires a modified control strategy [66]. The scope of this thesis will be limited to the multiphase combined winding architecture. Schematics of the different winding schemes are
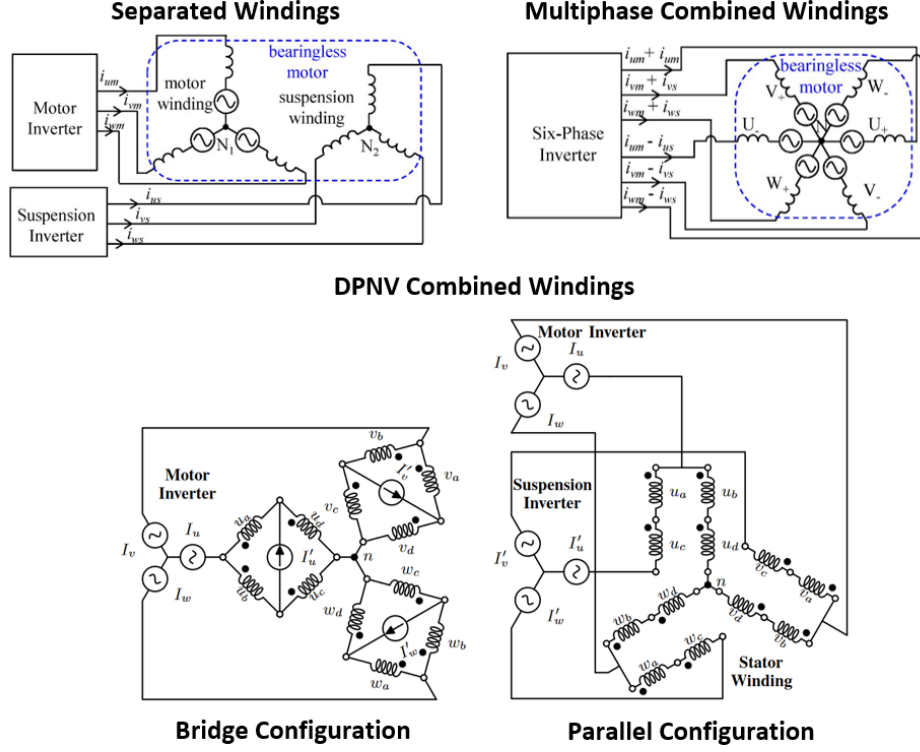
Figure 1.3: Schematics of different winding schemes. Figure adapted from [56] and [67].

presented in Figure 1.3.

Homopolar and Heteropolar Rotor

In bearingless motors, suspension forces are generated by deliberately perturbing a symmetric air gap flux distribution established by a bias field. These motors can be generally classified into two main categories based on the nature of the bias flux field: homopolar and heteropolar motors.

Homopolar motors are characterized by a static unidirectional bias field as seen from the rotor/stator. This bias field is established using permanent magnets or field windings normally placed at the stator. Suspension forces are generated by superimposing a 2-pole suspension flux onto the bias flux field. The resulting imbalance of the airgap flux imparts a radial force on the rotor. By controlling the magnitude and direction of the 2-pole suspension
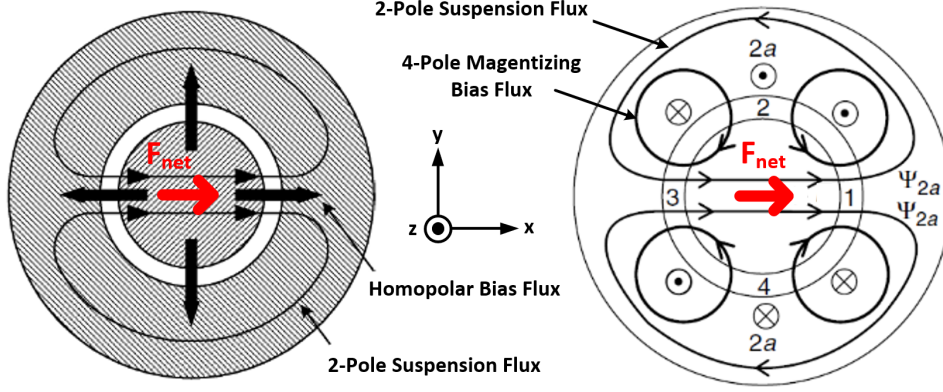
Figure 1.4: Suspension force generation in homopolar (left) and heteropolar bearingless Motors. net force generated in the positive x direction in both instances. Figure adapted from [14].

flux in a negative feedback loop we are able to actively stabilize and regulate the position of the rotor.

In contrast, heteropolar motors leverage the pre-existing p-pole pair magnetizing field of the motor as the bias field. Suspension forces are generated by superimposing a $p \pm 1$ pole pair suspension flux field onto the rotating bias flux field. An important distinction between the two motor types is that in heteropolar motors the bias field is synchronously rotating with the rotor and therefore accurate real-time knowledge of the rotor's angular position is required to correctly align the superimposed suspension flux and achieve successful levitation. Errors or delays in the rotor angle measurement manifest as a radial disturbance force that cross-couples the x and y-axis motions [28]. This has a destabilizing effect on the suspension control and is more pronounced at high speeds. This is contrary to homopolar motors where suspension operation is decoupled from the rotor angle, allowing for a simple and robust control strategy. The force generation mechanism for both motor types is illustrated in Figure 1.4.

Slice Motors

Conventionally, achieving magnetic levitation or suspension of a motor shaft necessitates active control over all six degrees of freedom (DOFs). This is typically accomplished by utilizing a pair of two-degree-of-freedom (2DOF)

9
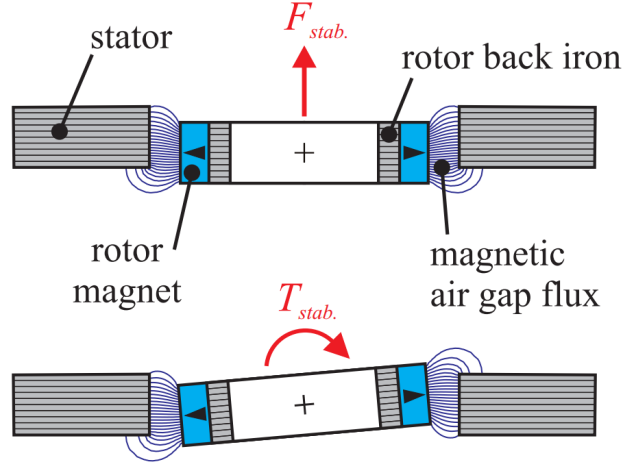
Figure 1.5: Passive stability of bearingless slice motor [21].

bearingless motors to control the radial and tilting motions, along with an axial active magnetic bearing (AMB) to regulate the axial motion.

Slice motors are characterized by a small rotor axial length-to-diameter ratio. This rotor geometry was first proposed in [65] and is capable of passively stabilizing the axial and tilting motions through reluctance forces. This leaves only the inherently unstable radial DOFs and the rotor angle in need of active control. Such a motor topology reduces the overall footprint, control complexity, and instrumentation requirements by eliminating the need for auxiliary radial and thrust bearings to control all 6 DOFs. The passive stabilization mechanism is visually depicted in Figure 1.5. Bearingless slice motors have been developed for low power ratings across a broad speed range and have been successfully commercialized by companies like Levitronix for their ultrapure fluid handling pumps [35] and BiVACOR [5] for their artificial hearts.

1.1.4 Sensorless Control

The control of an AC motor's instantaneous torque is the primary objective of motor drive systems. One widely adopted control technique to achieve that is field-oriented control (FOC) also commonly referred to as vector control. The idea behind FOC is to conceptually decompose the multiphase currents into torque and flux-producing components that can be independently regulated. This is accomplished by using mathematical transformations,

such as Park's and Clarke's transformation, to represent the multiphase motor currents in a rotating reference frame. However, performing these transformations requires knowledge of the rotor angle, and as such motor drives are normally equipped with angular position sensors such as encoders, resolvers, or Hall effect sensors. In addition to the angular position sensors bearingless motors also employ displacement sensors for sensing the radial position of the rotor. Some common types of displacement sensors include eddy current sensors, optical sensors, and capacitive sensors.

The inclusion of such sensors brings many problems such as an increase in cost and complexity, susceptibility to noise and harsh operating conditions, and a need for frequent maintenance which degrades the overall reliability and robustness of the system. To overcome these issues significant research efforts have been made in developing sensorless drives with comparable dynamic performance to sensor-based systems. In the context of motor control, the term sensorless control refers to operation without position sensors. Instead, information regarding the rotor's position and speed is indirectly inferred from the phase current and voltage information.

Efforts aimed at simplifying the instrumentation requirements, be it through sensor elimination or simplification, can yield significant advantages such as cost savings and improved reliability. Additionally, the sensorless estimation techniques can also be used for fault monitoring of sensor-based control systems and even act as a viable backup in case of sensor failure thus reducing downtime.

Sensorless control schemes can be broadly categorized into model-based methods and saliency-based methods. Model-based methods use the dynamic model of the motor as a basis to estimate certain signals of interest. However, these methods often lack observability to detect low-frequency information. To overcome these limitations, saliency-based methods were developed enabling reliable estimation of low-frequency information. These methods exploit the position-dependent variation of rotor characteristics such as inductance and flux linkage to estimate its position. Most often, these methods work by analyzing the response of the machine under a high-frequency excitation signal to extract relevant rotor position information.

Extensive research has been conducted on angle sensorless control for conventional motors, with comprehensive findings summarized in numerous review papers [7, 58, 83]. In contrast, radial position sensorless control specific to bearingless motors remains in its early stages of development with limited published experimental results [25, 75]. Nonetheless, ongoing research

and advancements in sensorless control continue to improve the accuracy and performance of these techniques, driving their widespread adoption in a wide range of applications.

1.2 Objective and Outline of the Thesis

This research complements and builds upon prior work done by former UBC graduate student Simon Szoke who designed and built a prototype bearingless motor for his MASc thesis. The motor is a homopolar bearingless slice motor with a solid steel reluctance rotor and a quadruple three-phase combined winding scheme. This motor was primarily based on Dr. Minkyun Noh's previous work [53] with a number of proposed improvements focused primarily on improving the power density of the machine. These improvements included novel stator and rotor designs, as well as a transition from a separated winding scheme to a combined multiphase winding scheme. However, these improvements were exclusively from a motor design standpoint.

As part of his project, Simon utilized 4 off-the-shelf three-phase servo amplifiers for motor control. The setup used by Simon is shown in Figure 1.6a. However, relying solely on commercially available motor drives poses limitations in terms of research possibilities. Since commercially available motor drives support only three phases and obscure the internal workings of the system, they are not well suited for use in a research-oriented setting where a low level of algorithmic control is required.

Recognizing these limitations, a goal set forth by our lab is to create a custom motor control platform to advance research on multiphase machines and more specifically multiphase combined winding bearingless motors. In pursuit of this goal, we developed a custom multiphase motor drive solution that integrates the controller, sensor circuitry, and power stages, thereby facilitating prototyping and research efforts.

The development of this board allows us to revisit this problem from a controls-oriented standpoint by exploring and implementing different control strategies aiming to maximize the power density of the bearingless motor. Power density, a key performance metric for motors, refers to the amount of power that can be converted by the motor per its size and weight. By enhancing the power density of the bearingless motor, we can achieve more compact motor designs, enabling their use in a wider range of applications.

The performance of the motor drive was evaluated by connecting it to the
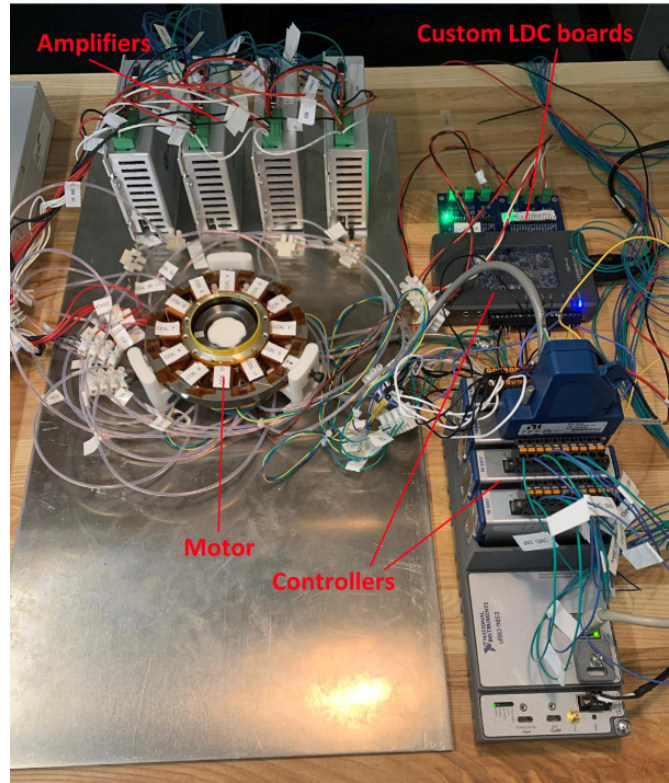
(a) Old setup [72].
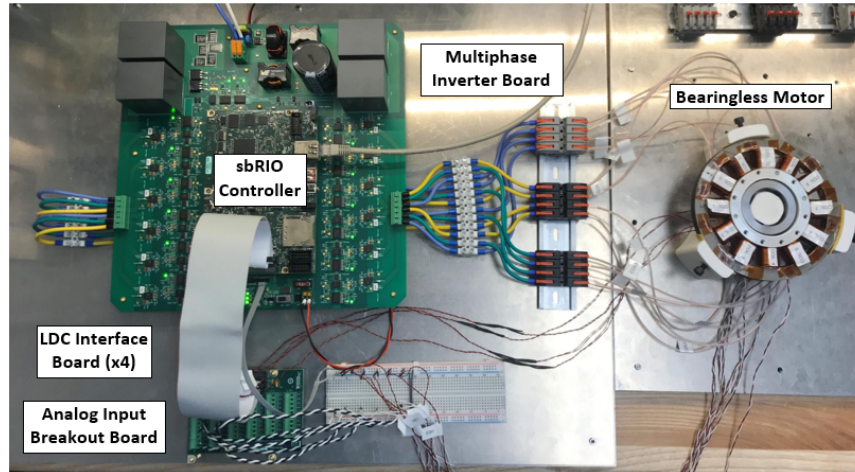
(b) Current setup.

Figure 1.6: Photo of old and current experimental setups.

bearingless motor prototype developed by Simon. The maximum speed achieved in [6] was limited to 9500 RPM. The results presented in this thesis are based on an improved motor drive system and control strategy. This allows operating the prototype up to its rated speed as limited by the available DC link voltage. The developed multiphase motor drive board and the prototype bearingless motor are presented in Figure 1.6b.

The remainder of this thesis is organized as follows. We strongly recommend reading the chapters in the order they appear to gain a better understanding of the content.

- **Chapter 2 - System Modelling:** This chapter establishes the mathematical models of the bearingless slice motor. These models serve as the basis for designing and tuning relevant control schemes.

- **Chapter 3 - Hardware Design:** In this chapter, details of the designed multiphase motor drive platform are documented.

- **Chapter 4 - Implementation and Testing:** This chapter presents the application of the developed motor drive to the prototype bearingless motor. It outlines the control scheme, its implementation, and presents test results.

- **Chapter 5 - Conclusion and Future Work:** In this chapter, the overall contributions are summarized and some suggestions for future work are given.

Chapter 2

Modeling and Analysis of Bearingless Slice Motors

This chapter focuses on establishing the mathematical model of multiphase combined winding bearingless motors and serves as the basis for designing and tuning applicable control schemes.

We begin by explaining a procedure for decoupling the torque and suspension systems in combined winding bearingless motors. We then separately investigate the rotation and suspension dynamics of a 2 DOF bearingless slice motor. The chapter finally concludes with the theory of model-based sensorless control strategies for rotor angular and radial position estimation.

2.1 Rotation and Suspension Decoupling Transformation

In contrast to conventional separated winding schemes, the utilization of combined multiphase windings in bearingless motors offers notable advantages such as simplified manufacturing and the ability to dynamically allocate the winding for torque-producing current or force-producing current as needed during runtime. However, in order to independently regulate the rotation and suspension of the motor, a decoupling procedure is necessary. This procedure involves a conceptual decomposition of the multiphase variables into a new set of variables responsible for generating torque and radial forces.

This is achieved using a generalized Clarke transformation matrix that transforms the original set of multiphase variables of an n-phase machine into $n/2$, or $(n-1)/2$ for odd n, independent space vectors residing in two-dimensional subspaces. These new subspaces are orthogonal and decoupled from one another leading to a simplified modeling and control of multiphase machines

[34]. The generalized Clarke transformation matrix C for an n-phase symmetrical machine characterized by a spatial displacement of $\phi = 2\pi/n$ between consecutive phases is given as

$$
C = \frac{2}{n}
\begin{bmatrix}
1 & \cos\phi & \cos 2\phi & \dots & \cos 2\phi & \cos\phi \\
0 & \sin\phi & \sin 2\phi & \dots & -\sin 2\phi & -\sin\phi \\
1 & \cos 2\phi & \cos 4\phi & \dots & \cos 4\phi & \cos 2\phi \\
0 & \sin 2\phi & \sin 4\phi & \dots & -\sin 4\phi & -\sin 2\phi \\
\vdots & \vdots & \vdots & \ddots & \vdots & \vdots \\
1 & \cos\left(\frac{n-2}{2}\right)\phi & \cos\left(\frac{n-2}{2}\right)2\phi & \dots & \cos\left(\frac{n-2}{2}\right)2\phi & \cos\left(\frac{n-2}{2}\right)\phi \\
0 & \sin\left(\frac{n-2}{2}\right)\phi & \sin\left(\frac{n-2}{2}\right)2\phi & \dots & -\sin\left(\frac{n-2}{2}\right)2\phi & -\sin\left(\frac{n-2}{2}\right)\phi \\
1/2 & 1/2 & 1/2 & \dots & 1/2 & 1/2 \\
1/2 & -1/2 & 1/2 & \dots & 1/2 & -1/2
\end{bmatrix}
$$

where the application of the matrix to transform the original set of n-phase variables to their decoupled representation in orthogonal subspaces is carried out as

$$
\begin{bmatrix}
f_{\alpha_1} \\
f_{\beta_1} \\
\vdots \\
f_{\alpha_{(n-2)/2}} \\
f_{\alpha_{(n-2)/2}} \\
f_{0+} \\
f_{0-}
\end{bmatrix}
= C
\begin{bmatrix}
f_1 \\
f_2 \\
\vdots \\
f_{n-1} \\
f_n
\end{bmatrix}
$$

The transformed variables denoted by $(\alpha_k\beta_k)$ subscripts represent the orthogonal components of the space vector in the k-th subspace. Control of these current components in each subspace leads to the production of a $2k$-pole field in the air gap. For instance, currents denoted by $i_{\alpha 4}, i_{\beta 4}$ will induce an 8-pole field in the air gap. It is important to note that this is only applicable provided that motor windings are designed such these current components map to the desired air gap field components. A winding design procedure to achieve that is outlined in [51].

The numeric subscript convention is adopted from this point onwards. The last two elements correspond to the positive and negative zero-sequence components $0+$ and $0-$ respectively. The $0+$ component represents the

average of the multiphase variables. For star-connected windings with a floating neutral point, the zero-sequence current components evaluate to zero. In the case of an even phase number, only the $0-$ component exists, however, this is a one-dimensional quantity with limited practical use in control and is therefore disregarded.

In multiphase motors, one subspace is used for the primary purpose of torque production, while the remaining subspaces provide additional degrees of freedom that can be leveraged for secondary purposes such as torque enhancement or post-fault operation [34].

To summarize, the generalized Clarke transformation transforms the original set of n variables into a new set of variables in decoupled subspaces with clear harmonic mapping of the induced spatial frequencies. However, this new set of variables is still attached to a stationary reference frame. When analyzing electrical machines, it is often beneficial to use a rotating coordinate system. This choice is motivated by the fact that sinusoidally varying quantities in stator fixed coordinates are transformed into DC quantities in rotor fixed coordinates. By using a rotational transformation, we can convert a vector expressed in the stationary frame $(\alpha_k \beta_k)$ to an equivalent representation in a rotor fixed reference frame $(d_k q_k)$ by rotating it with an electrical angle of $\theta_e = k\theta_m$, where θ_m represents the mechanical/physical rotor angle. Depending on the application, the rotational transformations are applied to specific $2k$ harmonic components as follows

$$\begin{bmatrix} f_{d_k} \\ f_{q_k} \end{bmatrix} = \begin{bmatrix} \cos(k\theta_m) & \sin(k\theta_m) \\ -\sin(k\theta_m) & \cos(k\theta_m) \end{bmatrix} \begin{bmatrix} f_{\alpha_k} \\ f_{\beta_k} \end{bmatrix}$$

The dq reference frame consists of two orthogonal axes: the d-axis and the q-axis. The d-axis is aligned with the rotor magnetizing flux, while the q-axis is perpendicular to the d-axis in electrical coordinates. This transformation to rotor fixed coordinates not only simplifies the machine model and analysis by eliminating rotor angle-dependent terms but also simplifies the control strategy by decoupling the torque-producing current component (i_q) along the q-axis from the flux-producing current component (i_d) along the d-axis. It also enables the use of simple PI controllers in tracking high-frequency sinusoidal references without the need for resonant controllers commonly used in single-phase systems. This simplified and decoupled control allows us to treat an AC machine as a separately excited DC motor and is the basis of field-oriented control also commonly referred to as vector control.
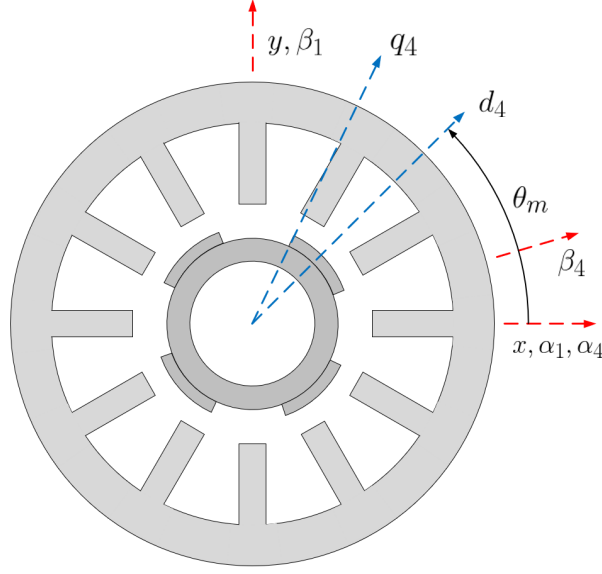
Figure 2.1: Coordinate systems in homopolar reference motor (not to scale).

The operation of a bearingless motor necessitates the generation of two distinct field components in the airgap: a synchronously rotating p-pole pair field for torque generation and a p_s-pole pair field for suspension force generation. This is accomplished by regulating the phase variables in the p and p_s subspaces for controlling the rotation and suspension of the rotor respectively. Using standard vector control theory we are able to control the magnitude and orientation/phase of these harmonic components to simultaneously levitate and rotate the rotor.

For instance, taking the reference prototype homopolar motor ($p = 4$, $p_s = 1$, $n = 12$) as an example, a synchronously rotating 8-pole field is required for torque generation, and a stationary 2-pole field that interacts with a preexisting homopolar bias field is required to generate levitation forces. Generation of these spatial field components is achieved by regulating the current vector components in the decoupled $\alpha_4\beta_4$ and $\alpha_1\beta_1$ subspaces respectively. Additionally, a rotational transformation is used to transform the rotating space vector in the stationary $\alpha_4\beta_4$ frame to an equivalent stationary vector expressed in the rotating d_4q_4 frame. A visual depiction of the different coordinate systems is presented in Figure 2.1. Here the stator fixed and the rotor fixed reference frames are denoted with red and blue lines respectively.

Transforming the original set of multiphase variables f_{1-n} into their decoupled representation in orthogonal subspaces and vice versa is carried out as

$$
\begin{bmatrix} f_{\alpha_{ps}} \\ f_{\beta_{ps}} \\ f_{d_p} \\ f_{q_p} \end{bmatrix} = [T_r]\ [T_c]\ f_{1-n}
$$

$$
f_{1-n} = [T_c]^{-1}\ [T_r]^{-1} \begin{bmatrix} f_{\alpha_{ps}} \\ f_{\beta_{ps}} \\ f_{d_p} \\ f_{q_p} \end{bmatrix} = \frac{n}{2}\ [T_c]^T\ [T_r]^T \begin{bmatrix} f_{\alpha_{ps}} \\ f_{\beta_{ps}} \\ f_{d_p} \\ f_{q_p} \end{bmatrix}
$$

where T_c and T_r are matrices of dimension $4{\times}n$ and $4{\times}4$ respectively

$$
T_c = \frac{2}{n} \begin{bmatrix}
1 & \cos p_s\phi & \cos 2p_s\phi & \dots & \cos 2p_s\phi & \cos p_s\phi \\
0 & \sin p_s\phi & \sin 2p_s\phi & \dots & -\sin 2p_s\phi & -\sin p_s\phi \\
1 & \cos p\phi & \cos 2p\phi & \dots & \cos 2p\phi & \cos p\phi \\
0 & \sin p\phi & \sin 2p\phi & \dots & -\sin 2p\phi & -\sin p\phi
\end{bmatrix}
$$

$$
T_r = \begin{bmatrix}
1 & 0 & 0 & 0 \\
0 & 1 & 0 & 0 \\
0 & 0 & \cos p\theta_m & \sin p\theta_m \\
0 & 0 & -\sin p\theta_m & \cos p\theta_m
\end{bmatrix}
$$

The matrix T_c represents the generalized Clarke transformation responsible for the decoupling of the multiphase variables into different subspaces, while T_r represents the rotational transformation matrix.

By employing this decoupling procedure, we effectively separate the analysis of suspension and rotation in a combined winding machine, treating it as if it had separate windings. This enables a simplified approach to the modeling and control of bearingless motors. From this point onwards, we refer to the $\alpha_p\beta_p$ and $\alpha_{p_s}\beta_{p_s}$ subspaces as rotation and suspension windings respectively. However, it is important to note that these are fictitious windings and this naming convention, although not technically correct, is simply used for its convenience.

2.2 Bearingless Motor Model

Having explained the concept of space vectors and their uses in the control and analysis of multiphase machines we now shift our attention to the mathematical model of the bearingless slice motor. The equations presented will be specific to the reference prototype homopolar motor but the general principles and methodology apply and can be extended to most bearingless machines.

2.2.1 Mechanical Dynamics

When modeling the mechanical motions of the motor for the ultimate purpose of designing and tuning suitable control schemes we are only concerned with capturing the dynamics of the controllable DOFs. For a bearingless slice motor, this consists of the linear displacements along the x and y-axes and rotations about the z-axis, where all motions are assumed to be decoupled from one another.

The dynamics of the linear motions are similar to that of a two-axis magnetic bearing system. A typical differential magnetic bearing system is modeled as a mass-spring system with a destabilizing negative spring stiffness. This spring force is representative of the unbalance pull force that grows in proportion to the rotor's eccentricity. A stabilizing controller should be able to compensate for this effect in order to achieve successful levitation. The equations of motion are expressed in a stationary reference frame where no cross-coupling terms due to fictitious forces appear. The dynamics are described using Newton's second law of motion as

$$F_{ex} + K_x x = K_{ix}i_\alpha + K_x x = m\ddot{x}$$
$$F_{ey} + K_y y = K_{iy}i_\alpha + K_y y = m\ddot{y}$$
$$T_e - T_l = J\ddot{\omega}_m$$

where m and J are the mass and rotational inertia of the rotor, x and y are the linear displacements of the rotor relative to the magnetic center of the stator, ω_m is the angular speed of the motor, T_e and T_l are the electromagnetic and load torques, $K_{x,y}$ are the equivalent spring constants for each corresponding axis, and $F_{ex,ey}$ are the electromagnetic radial forces established by the windings. This force is modeled as the product of the suspension current $i_{\alpha,\beta}$ and a force constant $K_{ix,iy}$. This force constant is

proportional to the bias flux and can vary as a function of the rotor angle depending on the type of bearingless motor being modeled. The bias field in the heteropolar motor category is established using the motor's rotating p-pole pair magnetizing flux. Therefore the force constant exhibits a dependency on the rotor angle. This is contrary to homopolar motors that have a fixed force constant in principle. Due to this angle dependency, heteropolar motors require an appropriate current commutation procedure to linearize the force-current relationship for controller implementation. To this end, Chiba outlines a decoupling method in [14].

It is important to note that the presented models are linearized about the rotor-centric position. In reality, the force and spring constants also exhibit a dependency on the rotor's radial position but this effect is neglected for our linear controller implementation. Attempts at arriving at more comprehensive models that include effects of eccentricity, and field saturation are presented in [64] however that is beyond the scope of this project and is not addressed any further.

2.2.2 Electrical Dynamics

The electrical dynamics of a motor are governed by the voltage and flux linkage equations. The voltage and flux linkage equations of the stator windings are expressed as

$$v_{1-n} = R_s\, i_{1-n} + \frac{\mathrm{d}\lambda_{1-n}}{\mathrm{d}t}$$
$$\lambda_{1-n} = [L_n]\, i_{1-n} + \lambda_f$$

where R_s is the phase winding resistance, $[L_n]$ is the $n \times n$ inductance matrix, and $v_{1-n} = [v_1 \dots v_n]^T$ is the phase voltage vector. The phase current i_{1-n} and flux linkage λ_{1-n} vectors are similarly defined. The resistance of the different phase windings are assumed to be identical, and as such it is treated as a scalar quantity. By using the generalized Clarke transformation matrix $[T_c]$ defined earlier, the voltage equations of the fictitious rotation and suspension windings are derived as

$$\underbrace{[T_c]\, v_{1-n}}_{v_{\alpha\beta}} = R_s \underbrace{[T_c]\, i_{1-n}}_{i_{\alpha\beta}} + \underbrace{[T_c]\, \frac{\mathrm{d}\lambda_{1-n}}{\mathrm{d}t}}_{\frac{\mathrm{d}\lambda_{\alpha\beta}}{\mathrm{d}t}}$$

$$v_{\alpha\beta} = R_s\, i_{\alpha\beta} + \frac{\mathrm{d}\lambda_{\alpha\beta}}{\mathrm{d}t}$$

Similarly, the flux linkage equations of the fictitious windings are derived as

$$\underbrace{[T_c]\, \lambda_{1-n}}_{\lambda_{\alpha\beta}} = \underbrace{[T_c]\, [L_n]\, [T_c]^{-1}}_{L_{\alpha\beta}}\, i_{\alpha\beta} + \underbrace{[T_c]\, \lambda_f}_{\lambda_{f_{\alpha\beta}}}$$

Rewriting the voltage equations in matrix form yields

$$\underbrace{\begin{bmatrix} v_{\alpha_p\beta_p} \\ v_{\alpha_{ps}\beta_{ps}} \end{bmatrix}}_{v_{\alpha\beta}} = R_s \underbrace{\begin{bmatrix} i_{\alpha_p\beta_p} \\ i_{\alpha_{ps}\beta_{ps}} \end{bmatrix}}_{i_{\alpha\beta}} + \frac{\mathrm{d}}{\mathrm{d}t} \underbrace{\begin{bmatrix} \lambda_{\alpha_p\beta_p} \\ \lambda_{\alpha_{ps}\beta_{ps}} \end{bmatrix}}_{\lambda_{\alpha\beta}}$$

where $v_{\alpha_{ps}\beta_{ps}} = [v_{\alpha_{ps}}\ v_{\alpha_{ps}}]^T$ and $v_{\alpha_p\beta_p} = [v_{\alpha_p}\ v_{\alpha_p}]^T$ are the suspension and rotation winding voltage vectors respectively. The current and flux linkage vectors are similarly defined. The flux linkage equations are further expanded in block matrix form as

$$\begin{bmatrix} \lambda_{\alpha_p\beta_p} \\ \lambda_{\alpha_{ps}\beta_{ps}} \end{bmatrix} = \underbrace{\begin{bmatrix} L_{\alpha_p\beta_p} & M \\ M^T & L_{\alpha_{ps}\beta_{ps}} \end{bmatrix}}_{L_{\alpha\beta}} \begin{bmatrix} i_{\alpha_p\beta_p} \\ i_{\alpha_{ps}\beta_{ps}} \end{bmatrix} + \underbrace{\begin{bmatrix} \lambda_{f_{\alpha_p\beta_p}} \\ \lambda_{f_{\alpha_{ps}\beta_{ps}}} \end{bmatrix}}_{\lambda_{f_{\alpha\beta}}}$$

where the inductance matrices and the permanent magnet flux linkage vectors are given as

$$L_{\alpha_p\beta_p} = \begin{bmatrix} L_{\alpha_p} & 0 \\ 0 & L_{\beta_p} \end{bmatrix} \quad L_{\alpha_{ps}\beta_{ps}} = \begin{bmatrix} L_{\alpha_{ps}} & 0 \\ 0 & L_{\beta_{ps}} \end{bmatrix} \quad M = \begin{bmatrix} M_{\alpha_p\alpha_{ps}} & M_{\alpha_p\beta_{ps}} \\ M_{\beta_p\alpha_{ps}} & M_{\beta_p\beta_{ps}} \end{bmatrix}$$

$$\lambda_{f_{\alpha_p\beta_p}} = K_e \begin{bmatrix} \cos p\theta_m \\ \sin p\theta_m \end{bmatrix} \quad \lambda_{f_{\alpha_{ps}\beta_{ps}}} = \begin{bmatrix} \lambda'_{f_{\alpha_{ps}}} x \\ \lambda'_{f_{\beta_{ps}}} y \end{bmatrix}$$

$(L_{\alpha_p}, L_{\beta_p})$ and $(L_{\alpha_{ps}}, L_{\beta_{ps}})$ are the rotation and suspension winding self inductances respectively; M is the mutual inductance matrix; K_e is the rotation winding permanent magnet flux linkage; and $(\lambda'_{f_{\alpha_{ps}}}, \lambda'_{f_{\beta_{ps}}})$ are the derivatives of the suspension winding permanent magnet flux linkage $(\mathrm{Wb\,m^{-1}})$ with respect to the x and y directions respectively.

Suspension Windings

In heteropolar motors, the suspension forces are generated by the interaction of the fields produced by the suspension and rotation windings. This interaction occurs via the mutual inductance matrix M which plays a crucial role in establishing the suspension force characteristics of heteropolar motors. In the reference homopolar motor, this matrix approximates to zero, as validated by FEA simulations, offering minor contributions to the suspension force, and therefore is neglected in our analysis.

By neglecting the effects of the mutual inductance matrix we can decouple and separate the flux linkage equations of the rotation and suspension windings for separate analysis. Substituting back the decoupled flux linkage equations into the voltage equations yields our final suspension winding voltage equation as

$$v_{\alpha_{ps}} = R_s i_{\alpha_{ps}} + L_{\alpha_{ps}} \frac{di_{\alpha_{ps}}}{dt} + \lambda'_{f_{\alpha_{ps}}} \dot{x}$$
$$v_{\beta_{ps}} = R_s i_{\beta_{ps}} + L_{\beta_{ps}} \frac{di_{\beta_{ps}}}{dt} + \lambda'_{f_{\beta_{ps}}} \dot{y}$$

Expressions for the electromagnetic radial force can be obtained using the co-energy method. The magnetic co-energy W'_m is given as

$$W'_m = \frac{n}{2} \left(\frac{1}{2} i^T_{\alpha\beta} L_{\alpha\beta} i_{\alpha\beta} + \lambda^T_{f_{\alpha\beta}} i_{\alpha\beta} \right)$$

By taking the partial derivative of the co-energy with respect to x and y displacements, the force expressions in the corresponding axes are obtained as
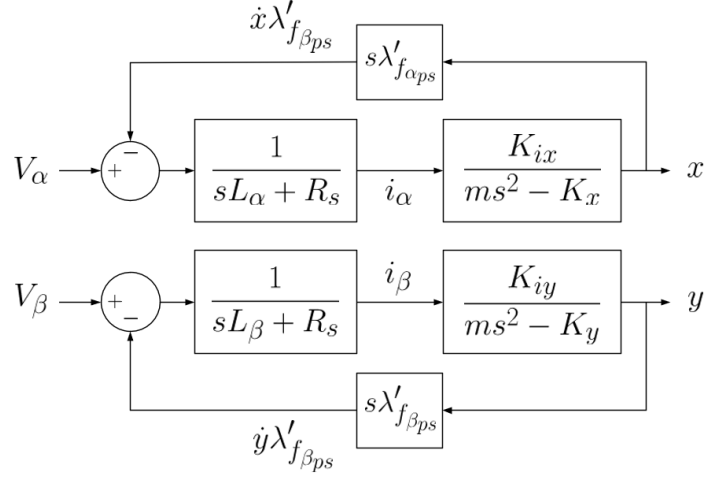
Figure 2.2: Suspension plant block diagram.

$$F_{ex} = \frac{n}{2} \lambda'_{f_{\alpha ps}} i_{\alpha ps} = K_{ix} i_{\alpha ps}$$
$$F_{ey} = \frac{n}{2} \lambda'_{f_{\beta ps}} i_{\beta ps} = K_{iy} i_{\beta ps}$$

It is important to note that due to the neglection of the mutual inductance terms, this is not a general procedure that can be extended to any homopolar motor. A generalized analytical procedure for computing the suspension force constants using the Maxwell stress tensor method in homopolar bearingless motors is presented in [26]. A block diagram representation of the suspension subsystem is presented in Figure 2.2.

Rotation Windings

The voltage and flux linkage equations of the rotation windings are transformed to a synchronously rotating reference frame $d_p q_p$ where the sinusoidally varying quantities appear as DC quantities. Substituting the flux linkage equations into the voltage expression yields the following voltage equations

$$v_{d_p} = R_s i_{d_p} + L_{d_p} \frac{di_{d_p}}{dt} - \omega_e L_{q_p} i_{q_p}$$

$$v_{q_p} = R_s i_{q_p} + L_{q_p} \frac{di_{q_p}}{dt} + \omega_e L_{d_p} i_{d_p} + \omega_e K_e$$

where L_{d_p} and L_{q_p} are the inductances expressed in the $d_p q_p$ reference frame and $\omega_e = p\omega_m$ is the rotor electrical speed. The first two terms in the rotation winding voltage equations are the resistive and inductive voltage drops respectively. The remaining terms are speed-induced voltage terms that grow in proportion to the rotor's speed. These terms emerge as we transform from a stationary reference frame to a rotating one.

Assuming the rotor is maintained in the magnetic center position, The torque generation principle is identical to that of a permanent magnet synchronous motor (PMSM) and thereby it is treated as such. Due to rotor eccentricity, there can be a coupling between the suspension and rotation which may generate parasitic torque disturbances however that effect is often neglected for a simplified controller implementation. The torque equation is given as

$$T_e = \frac{np}{2} \left[\lambda_{d_p} i_{q_p} - \lambda_{q_p} i_{d_p} \right] = \frac{np}{2} [\ \underbrace{K_e i_{q_p}}_{\text{PM Torque}} + \underbrace{(L_{d_p} - L_{q_p}) i_{d_p} i_{q_p}}_{\text{Reluctance Torque}}]$$

From this, we see that the net torque developed by a PMSM motor consists of two components. The first term is the permanent magnet torque which arises from the interaction of the magnetic fields established by the permanent magnets with the magnetic fields induced by the stator windings. The second term is a reluctance torque that arises due to saliency $(L_{d_p} - L_{q_p})$. This torque is produced as the rotor tends to align itself with the stator's magnetic field to minimize the magnetic reluctance.

Furthermore, we observe that there is no unique mapping from the commanded current reference vector to the resulting output torque, indicating the possibility for optimization. To address this, control strategies such as MTPA (Maximum Torque per Ampere) aim to maximize the motor's efficiency by minimizing copper losses. This is done by selecting an optimum current reference vector that maximizes the torque per unit of current

supplied to the motor. Successful application of the MTPA strategy requires accurate knowledge of the motor's parameters. Motors that exhibit no saliency ($L_{d_p} = L_{q_p}$) have a simple MTPA strategy where the i_{d_p} current is maintained at zero since it does not contribute to torque production.

The MTPA control strategy is effective when the motor operates within its base speed. The motor's base speed denotes the angular velocity at which the maximum line to neutral voltage v_{max} is supplied by the inverter. This speed is dependent on the available DC bus voltage V_{DC} and the loading conditions and can be derived from the steady state voltage equations as follows

$$v_{d_p} = R_s i_{d_p} - \omega_e L_{q_p} i_{q_p}$$
$$v_{q_p} = R_s i_{q_p} + \omega_e L_{d_p} i_{d_p} + \omega_e K_e$$

By neglecting the resistive voltage drop terms due to their small contributions at high speeds, the base speed is approximated as

$$v_{max} = \frac{1}{\sqrt{3}} V_{DC} \geq \sqrt{v_{d_p}^2 + v_{q_p}^2}$$
$$\omega = \frac{v_{max}}{\sqrt{\left(L_{q_p} i_{q_p}\right)^2 + \left(L_{d_p} i_{d_p} + K_e\right)^2}}$$

As the motor approaches its base speed, as dictated by the available DC bus voltage and the loading conditions, the increasing speed-induced voltage terms progressively reduce the differential voltage margin available for controlling the stator currents. Consequently, operation beyond the rated speed necessitates the implementation of a flux-weakening control strategy.

Flux weakening involves the reduction of the back electromotive force (EMF) by injecting negative i_{d_p} currents to reduce the flux linkage in the d-axis. This approach aims to maintain a voltage margin that allows for effective control of the stator currents. Operating in the flux weakening regime entails a trade-off between torque and speed, with a reduction in torque in exchange for increased rotational speed.

2.3 Sensorless Control

Having established the mathematical model of the bearingless slice motor, we now examine how these models can be used to construct state observers for estimating the rotor angular and radial positions.

2.3.1 Angle Estimation

Angle sensorless control of PMSM motors can be mainly grouped into two main categories: model-based methods and saliency-based methods.

Model-based methods use the dynamic model of the motor to estimate certain states of interest (eg. back emf or rotor flux linkage) from which the rotor angular position and speed information can be extracted. However, the magnitude of these position-related states is proportional to the rotor speed. Consequently, these methods suffer from a degradation in performance at low speeds due to the low signal-to-noise ratio (SNR).

Model-based methods have been realized using both open-loop calculations and closed-loop observers. Open-loop methods use the mathematical model of the motor to predict the position-related states of interest. These methods are sensitive to machine parameter variations, are susceptible to drift and measurement noise, and exhibit unsatisfactory transient performance. Closed-loop observers overcome these shortcomings by having a feedback correction scheme that minimizes prediction errors in measured states thereby facilitating the convergence of unmeasured states of interest towards their true values. Several observer schemes such as linear state observers [12], sliding mode observers (SMO) [13], and extended Kalman filters (EKF) [8] have been proposed in the literature. Among these methods, the linear state observer strikes a balance between computational efficiency, performance, and robustness to parameter variations.

Saliency-based methods were developed to overcome the low-speed limitations of model-based methods and enable reliable sensorless control at low speeds and stand still. These methods exploit the magnetic saliency, which refers to the spatial variation of inductance based on rotor position, present in certain motor constructions. By injecting a high-frequency excitation signal into the motor, saliency-based methods can extract and utilize this saliency to estimate the rotor position. Motors that exhibit no saliency are not good candidates for this sensorless estimation method. To address this, there is ongoing research on developing sensorless estimation methods for nonsalient machines.

However, in contrast to model-based methods, the use of a high-frequency excitation signal in saliency-based methods presents a number of challenges that render them less favorable. For instance, injection of the high-frequency voltage incurs losses and consumes a portion of the available voltage margin, limiting high-speed operation. Additionally, saliency-based methods require complex signal processing procedures to estimate the rotor position information. To address this limitation, hybrid schemes have been proposed, combining both model-based and saliency-based methods. This hybrid approach uses saliency-based methods at low speeds and standstill, where they are necessary, and transitions to model-based methods at medium to high speeds. By doing so, reliable sensorless performance is ensured across the entire operating speed range of the motor.

For the reference homopolar motor, a lack of sufficient saliency ($L_{d_p} \approx L_{q_p}$) rules out the possibility of using saliency-based methods. As such we focus on model-based methods. In particular, we experiment with two variants of the linear state observer and highlight the differences in testing. To enable complete sensorless operation we employ an open loop startup method which brings up the motor up to a speed where the model-based methods perform reliably.

Stationary Frame Back Emf Observer [12]

The voltage equations of the rotation windings in the synchronously rotating $d_p q_p$ frame are repeated here for convenience. The following analysis applies to the rotation windings and thus the subscript p is omitted for convenience and better readability

$$\begin{bmatrix} V_d \\ V_q \end{bmatrix} = \begin{bmatrix} R + sL_d & -\omega_e L_q \\ \omega_e L_d & R + sL_q \end{bmatrix} \begin{bmatrix} i_d \\ i_q \end{bmatrix} + \begin{bmatrix} 0 \\ \omega_e K_e \end{bmatrix}$$

where s is the time differential operator and K_e is the back emf constant of the machine. Rewriting the voltage equations such that the impedance matrix is in skew-symmetric form we obtain the following

$$\begin{bmatrix} V_d \\ V_q \end{bmatrix} = \begin{bmatrix} R + sL_d & -\omega_e L_q \\ \omega_e L_q & R + sL_d \end{bmatrix} \begin{bmatrix} i_d \\ i_q \end{bmatrix} + \underbrace{\begin{bmatrix} 0 \\ E_{ex} \end{bmatrix}}_{e_{dq}} \tag{2.1}$$

$$E_{ex} = (L_d - L_q)(\omega_e i_d - \dot{i_q}) + \omega_e K_e$$

28

The dot operator $\dot{i}_q$ means that it is only effective for i_q. This usage is different from the differential operator s which acts on any terms it is multiplied by. Moreover, the vector $[0 \ E_{ex}]^T$ is known as the extended EMF (EEMF). The extended EMF is an extension of the back EMF concept which aims to generalize the analysis to salient machines. In the case of nonsalient machine with $(L_{d_p} = L_{q_p})$, this term simply evaluates to the well known back EMF $[0 \ \omega_e K_e]^T$ resulting in a simpler model. Transforming the voltage equations to the stationary $\alpha_p \beta_p$ frame yields

$$\begin{bmatrix} V_\alpha \\ V_\beta \end{bmatrix} = \begin{bmatrix} R + sL_d & \omega_e(L_d - L_q) \\ \omega_e(L_d - L_q) & R + sL_d \end{bmatrix} \begin{bmatrix} i_\alpha \\ i_\beta \end{bmatrix} + \begin{bmatrix} e_\alpha \\ e_\beta \end{bmatrix}$$

$$e_{\alpha\beta} = \begin{bmatrix} e_\alpha \\ e_\beta \end{bmatrix} = E_{ex} \begin{bmatrix} -\sin\theta_e \\ \cos\theta_e \end{bmatrix}$$

Rewriting the impedance matrix in a skew-symmetric form prior to the coordinate transformation cleverly eliminates any rotor angular position-dependent terms, that arise from magnetic saliency, in the corresponding impedance matrix expressed in the $\alpha_p \beta_p$ reference frame. This simplifies the estimation problem. More details on this procedure can be found in [12].

By examining the voltage equations, we observe that the rotor angle information θ_e is contained within the extended back emf term $e_{\alpha_p\beta_p}$. By regarding the extended emf terms as a disturbance with simplified dynamics, we can construct a disturbance observer to estimate these signals. The observer is constructed based on the following augmented state space model

$$\dot{e}_{\alpha\beta} = \omega_e E_{ex} \begin{bmatrix} -\cos\theta_e \\ -\sin\theta_e \end{bmatrix} + \dot{E}_{ex} \begin{bmatrix} -\sin\theta_e \\ \cos\theta_e \end{bmatrix} \approx \omega_e \begin{bmatrix} 0 & -1 \\ 1 & 0 \end{bmatrix} e_{\alpha\beta}$$

$$\frac{\mathrm{d}}{\mathrm{d}t} \begin{bmatrix} i_{\alpha\beta} \\ \hline e_{\alpha\beta} \end{bmatrix} = \begin{bmatrix} A_{11} & A_{12} \\ \hline A_{21} & A_{22} \end{bmatrix} \begin{bmatrix} i_{\alpha\beta} \\ \hline e_{\alpha\beta} \end{bmatrix} + \begin{bmatrix} B_1 \\ \hline B_2 \end{bmatrix} \begin{bmatrix} V_{\alpha\beta} \end{bmatrix}$$

$$A_{11} = -\left(\frac{R_s}{L_d}\right) I_{2\times 2} + \omega_e \left(\frac{L_d - L_q}{L_d}\right) J$$

$$A_{12} = -\left(\frac{1}{L_d}\right) I_{2\times 2}, \qquad A_{21} = B_2 = 0_{2\times 2}$$

$$A_{22} = \omega_e J \qquad B_1 = \left(\frac{1}{L_d}\right) I_{2\times 2}, \qquad J = \begin{bmatrix} 0 & -1 \\ 1 & 0 \end{bmatrix}$$

This state space model has four states of which the two current states $i_{\alpha_p \beta_p}$ are measured using sensors. A partition between the measured and unmeasured states is indicated by the lines seen in the state vector.

In developing the state space model a number of simplifying assumptions are made. Firstly, the rotor angular speed ω_e is regarded as a constant parameter in the model. This is based on the assumption that the electrical system time constant is far smaller than the mechanical time constant. Secondly, the dynamics of the extended emf term are simplified by ignoring the $\dot{E}_{ex}$ term. This simplification is justified by the fact that this term only arises when the currents i_d or i_q are changing. However, due to the high bandwidth of the current control loop, these changes occur rapidly, and their impact on the observer is limited by its bandwidth.

Instead of using a full-order observer, we use a reduced-order observer to solely estimate the unmeasured extended emf signals. This allows for a simpler and more efficient implementation in practice. The reduced order observer to estimate $e_{\alpha\beta}$ is constructed as follows

$$\dot{\hat{e}}_{\alpha\beta} - L\dot{i}_{\alpha\beta} = (A_{22} - LA_{12})\,\hat{e}_{\alpha\beta}$$
$$+ (A_{21} - LA_{12})\,i_{\alpha\beta} + (B_2 - LB_1)\,V_{\alpha\beta}$$

where $L = \begin{bmatrix} l_{11} & l_{12} \\ l_{21} & l_{22} \end{bmatrix}$ is the observer gain matrix designed using a pole placement procedure. The hat symbol indicates an estimated quantity. A block diagram representation of the reduced order observer is presented in Figure 2.4. The dynamics of the estimation error are described as

$$\Delta \dot{\hat{e}}_{\alpha\beta} = (A_{22} - LA_{12})\Delta\hat{e}_{\alpha\beta}$$

Therefore, provided that (A_{22}, A_{12}) are observable, the eigenvalues of $(A_{22} - LA_{12})$ can be freely assigned by a suitable choice of the observer gain matrix L. Expanding $(A_{22} - LA_{12})$ as

$$A_{22} - LA_{12} = \begin{bmatrix} \frac{l_{11}}{L_d} & -\omega_e + \frac{l_{12}}{L_d} \\ \frac{l_{21}}{L_d} + \omega_e & \frac{l_{22}}{L_d} \end{bmatrix}$$

It is apparent that the matrix elements, and consequently the eigenvalues, are dependent on the rotor's electrical speed. This dependency on rotor speed introduces some uncertainty regarding the observer's performance and stability across a wide speed range. For instance, by fixing the rotor speed ω_e at 100 rad/s we can design the observer gain matrix to place both closed-loop poles at -500 rad/s using the pole placement command **place()** in MATLAB. After designing the L matrix we plot the closed-loop pole locations as a function of rotor speed by evaluating the eigenvalues of $(A_{22} - LA_{12})$. The resulting plot is presented in Figure 2.3. The plot demonstrates that while the real parts of the poles remain unchanged, the imaginary parts grow proportionally with speed.

To mitigate the drift of the closed-loop pole locations, some experimentation was conducted with parameter-varying L matrices to maintain fixed pole locations regardless of speed. The design procedure for the variable L matrices involved evaluating the characteristic polynomial of the desired closed-loop pole locations (p_1, p_2) and using its associated companion matrix to determine the elements of the gain matrix:

$$A_{22} - LA_{12} = \begin{bmatrix} \frac{l_{11}}{L_d} & -\omega_e + \frac{l_{12}}{L_d} \\ \frac{l_{21}}{L_d} + \omega_e & \frac{l_{22}}{L_d} \end{bmatrix} = \begin{bmatrix} 0 & 1 \\ -(p_1 p_2) & (p_1 + p_2) \end{bmatrix}$$

$$L = \begin{bmatrix} l_{11} & l_{12} \\ l_{21} & l_{22} \end{bmatrix} = L_d \begin{bmatrix} 0 & 1 + \omega_e \\ -(p_1 p_2 + \omega_e) & (p_1 + p_2) \end{bmatrix}$$

However, the results obtained through simulations in Simulink using this variable gain matrix approach were generally unsatisfactory or exhibited noticeably inferior performance, characterized by sustained oscillations, compared to using a fixed gain matrix designed in MATLAB. Therefore, this approach was not further pursued.

Due to the sinusoidal nature of the extended back emf signals in the stationary reference frame, high bandwidth observers are required to successfully
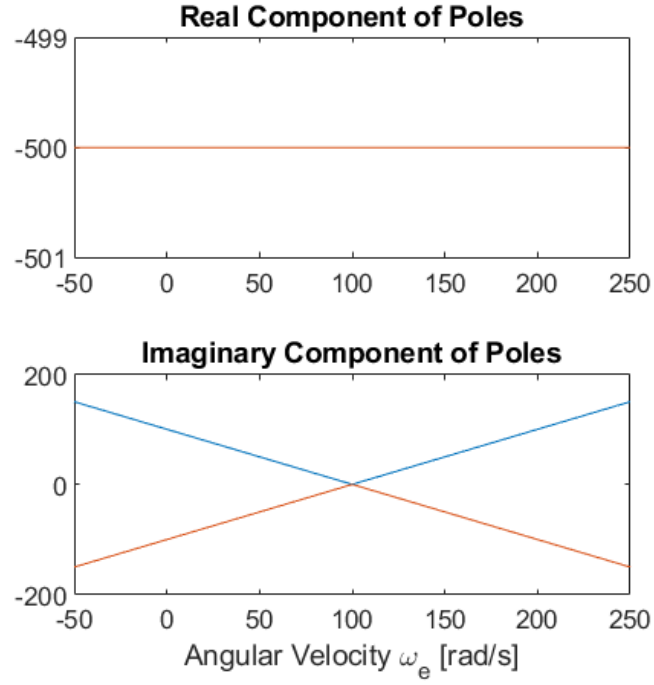
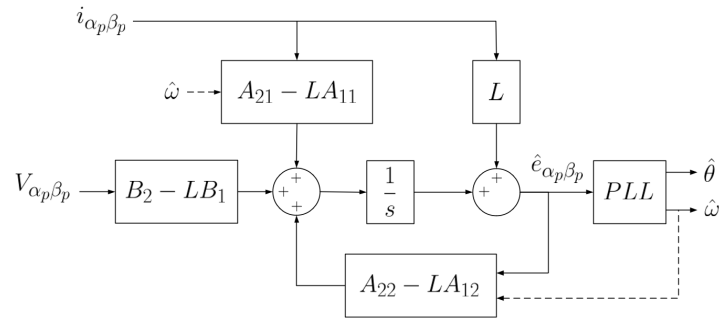Figure 2.3: Closed loop pole locations as a function of speed ω_e.

Figure 2.4: Stationary frame EEMF observer.

estimate these signals at high speeds with a low amplitude attenuation and phase lag. However, tuning the observer to have an arbitrarily high bandwidth limits its ability to reject noise effectively.

To overcome the limitations of this inherent tradeoff, [46] proposes a rotating frame back emf observer which aims to estimate the extended emf signals in the estimated rotor frame instead, where they appear as slowly varying DC quantities that are easy to track using low-bandwidth observers.

Rotating Frame Back Emf Observer [46]

In order to establish the new state space model in the estimated rotor frame we first transform the voltage equations 2.1 using the following transformation matrix and its inverse

$$\begin{bmatrix} f_{\hat{d}_p} \\ f_{\hat{q}_p} \end{bmatrix} = \begin{bmatrix} \cos(\Delta\theta_e) & -\sin(\Delta\theta_e) \\ \sin(\Delta\theta_e) & \cos(\Delta\theta_e) \end{bmatrix} \begin{bmatrix} f_{d_p} \\ f_{q_p} \end{bmatrix} \tag{2.2}$$

where $\Delta\theta_e = \theta_e - \hat{\theta}_e$ is the error between the estimated and actual electrical angle and the subscript $\hat{d}_p \hat{q}_p$ denotes the estimated rotor reference frame. Once again the p subscripts are omitted in the analysis that follows. Transforming the voltage equations to the estimated rotor reference frame yields

$$\begin{bmatrix} V_{\hat{d}} \\ V_{\hat{q}} \end{bmatrix} = \begin{bmatrix} R_s + pL_d & -\omega_{re}L_q \\ \omega_{re}L_q & R + pL_d \end{bmatrix} \begin{bmatrix} i_{\hat{d}} \\ i_{\hat{q}} \end{bmatrix} + \begin{bmatrix} e_{\hat{d}} \\ e_{\hat{q}} \end{bmatrix} \tag{2.3}$$

$$\begin{bmatrix} e_{\hat{d}} \\ e_{\hat{q}} \end{bmatrix} = E_{ex} \begin{bmatrix} -\sin(\Delta\theta_e) \\ \cos(\Delta\theta_e) \end{bmatrix} - \Delta\omega_e L_d \begin{bmatrix} -i_{\hat{d}} \\ i_{\hat{q}} \end{bmatrix} \tag{2.4}$$

Contrary to its equivalent representation in the stationary reference frame, the extended emf term in the estimated rotor reference frame is a function of the position error signal rather than the position itself.

From here we follow the same procedure as with the stationary frame observer. By regarding the extended emf terms as a disturbance with ignorable dynamics, we can construct a disturbance observer to estimate these signals. The observer is constructed based on the following augmented state space model

$$
\frac{\mathrm{d}}{\mathrm{d}t}
\begin{bmatrix} i_{\hat{d}\hat{q}} \\ e_{\hat{d}\hat{q}} \end{bmatrix}
=
\left[
\begin{array}{c|c} A_{11} & A_{12} \\ \hline A_{21} & A_{22} \end{array}
\right]
\begin{bmatrix} i_{\hat{d}\hat{q}} \\ e_{\hat{d}\hat{q}} \end{bmatrix}
+
\begin{bmatrix} B_1 \\ B_2 \end{bmatrix}
\begin{bmatrix} V_{\hat{d}\hat{q}} \end{bmatrix}
$$

$$
A_{11} = -\left(\frac{R_s}{L_d}\right) I_{2\times 2} + \omega_e \left(\frac{L_q}{L_d}\right) J
$$

$$
A_{12} = -\left(\frac{1}{L_d}\right) I_{2\times 2}, \qquad A_{21} = A_{22} = B_2 = 0_{2\times 2}
$$

$$
B_1 = \left(\frac{1}{L_d}\right) I_{2\times 2}, \qquad J = \begin{bmatrix} 0 & 1 \\ -1 & 0 \end{bmatrix}
$$

This state space model has four states of which the two current states $i_{\hat{d}\hat{q}}$ are measured using sensors. A partition between the measured and unmeasured states is indicated by the lines seen in the state vector.

As with the stationary frame observer, a number of simplifying assumptions are made in developing the state space model. Firstly, the rotor angular speed ω_e is regarded as a constant parameter in the model. Secondly, the dynamics of the extended emf term are assumed to be zero. This level of simplification may not be justifiable at rapidly accelerating or transient conditions. Reference [32] proposes a refined state space model which captures the effects of these neglected dynamics. However, their analysis is restricted to nonsalient machines with simpler models.

A reduced order observer to estimate the unmeasured EEMF signals $e_{\hat{d}_p\hat{q}_p}$ is constructed as follows

$$
\dot{\hat{e}}_{\hat{d}_p\hat{q}_p} - L\dot{i}_{\hat{d}_p\hat{q}_p} = (A_{22} - LA_{12})\,\hat{e}_{\hat{d}_p\hat{q}_p}
$$
$$
+ (A_{21} - LA_{12})\,i_{\hat{d}_p\hat{q}_p} + (B_2 - LB_1)\,V_{\hat{d}_p\hat{q}_p}
$$

where L is the observer gain matrix designed using a pole placement procedure. A block diagram representation of the reduced order observer is presented in Figure 2.5 The dynamics of the estimation error are described as
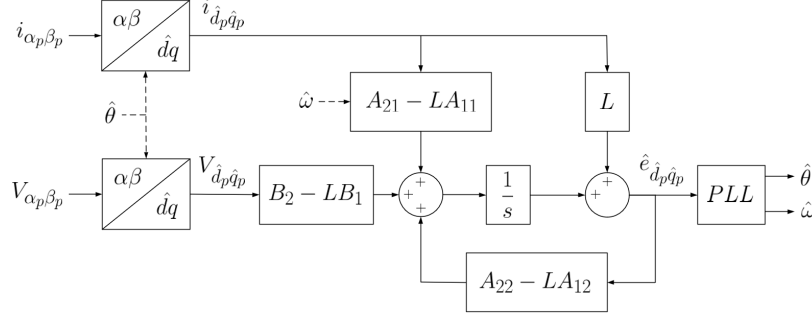
Figure 2.5: Rotating frame EEMF observer.

$$\Delta \dot{\hat{e}}_{\hat{d}_p \hat{q}_p} = (A_{22} - LA_{12})\Delta \hat{e}_{\hat{d}_p \hat{q}_p}$$

Contrary to the stationary frame observer, the matrix $(A_{22} - LA_{12})$ shows no dependence on rotor speed, thereby a fixed gain matrix can be designed to achieve the desired closed-loop pole locations.

Angle Tracking Observer

Having estimated the components of the EEMF signal the next step is to extract the rotor position information contained within them. Given the quadrature nature of the estimated signals, a simple and commonly employed strategy is to use an open loop inverse tangent calculation. However, this method is susceptible to noise, particularly near the zero crossing of the EEMF signals, and cannot be used if the output of the observer is a function of the position error signal as is the case with the rotating frame observer. Additionally, this method does not provide an estimate of the rotor speed on its own, requiring additional means to determine it.

An alternative method is to use a PLL-based angle-tracking observer to estimate the rotor position and speed. The basic idea of a PLL is to generate an output signal that is synchronized to some input reference signal. The PLL structure consists of a phase detection step followed by an error regulation loop. The phase detector compares the phases of the reference and output signals, yielding an error signal that indicates the phase difference between the two. The error regulation stage adjusts the frequency of the output signal to minimize the phase difference, thus achieving synchronization between the two signals.

Depending on the nature of the estimated EEMF signal the phase detection step may or may not be necessary. Starting with the stationary frame observer, a block diagram representation of the angle tracking observer is presented in Figure 2.6. Assuming the error between the estimated and actual rotor positions is small, the following trigonometric identity can be used to compute the phase difference between the input and output signals

$$E_{ex} \sin(\theta_e) \cos(\hat{\theta}_e) - E_{ex} \cos(\theta_e) \sin(\hat{\theta}_e) = E_{ex} \sin(\theta_e - \hat{\theta}_e) \approx E_{ex} \Delta\theta_e$$

Based on this error term a PI regulator can be designed to estimate the rotor speed $\hat{\omega}_e$ which is then integrated to estimate the rotor position $\hat{\theta}_e$. In the case of the rotating frame observer, the phase detection step is not necessary since the estimated EEMF is already a function of $\Delta\theta_e$. From the estimated EEMF signals the position error estimate can be derived in one of two ways

$$\Delta\theta_e = \tan^{-1}\left(\frac{-e_{\hat{d}_p}}{e_{\hat{q}_p}}\right) \quad \text{or} \quad \Delta\theta_e \approx \left(\frac{-e_{\hat{d}_p}}{E_{ex}}\right)$$

From here the same PLL structure excluding the phase detection step can be used. Neglecting the dynamics of the phase detection stage the closed-loop transfer function can be expressed as

$$G_{PLL} = \frac{\hat{\theta}(s)}{\Delta\theta(s)} = \frac{K_p s + K_i}{s^2 + K_p s + K_i}$$

Since the input to the error regulation loop $E_{ex}\Delta\theta$ grows in proportion to the rotor speed the normalization procedure, shown in Figure 2.6, is done to desensitize the tracking performance of the PLL to the motor speed.

Tuning of the controller parameters is done in accordance with the design procedure presented in [80]. This procedure aims to limit the maximum estimation error $\Delta\theta$ subject to a maximum acceleration of a. The derivation details are omitted but the final result is presented below

$$\rho = \sqrt{\frac{a}{\Delta\theta_{max}}} \quad K_p = 2\rho \quad K_i = \rho/2$$
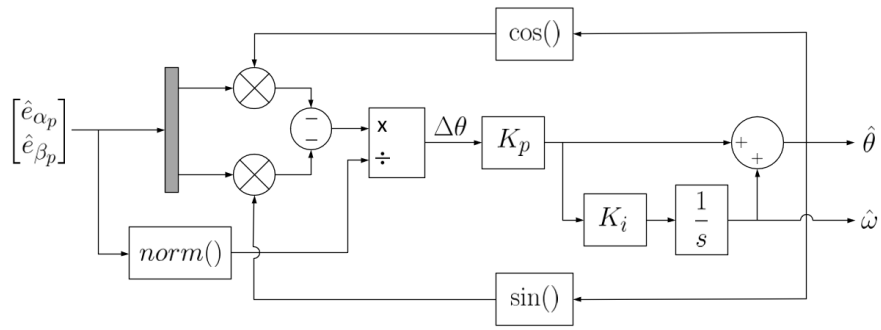
(a)
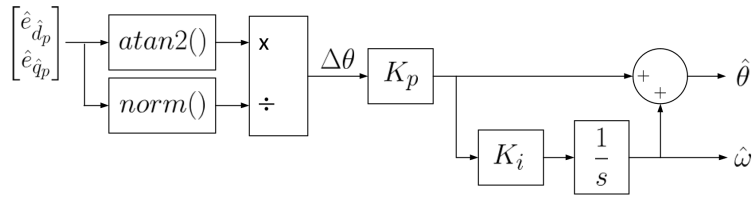
(b)

Figure 2.6: PLL-based angle tracking observers for (a) stationary and (b) rotating frame EEMF observer implementations.

2.3.2 Radial Displacement Estimation

Similar to the categorization of angle sensorless control methods there are two main approaches for estimating the rotor radial position; model-based methods and methods that exploit position-dependent variations in the machine parameters and their observable effects on measured states.

Model-based methods exhibit a number of drawbacks including their inability to estimate the rotor's absolute position and susceptibility to instability with slight parameter variations and uncertainties [40]. To address these challenges, there is ongoing research on alternative schemes providing robust estimation performance such as high-frequency injection methods [49, 50].

Nevertheless, despite their shortcomings, model-based methods have been successfully demonstrated on AMBs [45]. However, to the best of our knowledge, they have not been applied to homopolar bearingless motors which motivated us to extend their application to this domain.

To construct a state observer for estimating the rotor position we first develop a linear state space model using the suspension winding voltage equations and the radial displacement equations of motion. Since the dynamics of the two axes are assumed to be decoupled only a single axis is shown to avoid redundancy. The state space model is formulated as follows:

$$
\frac{\mathrm{d}}{\mathrm{d}t}
\begin{bmatrix}
i_{\alpha_{ps}} \\
x \\
\dot{x}
\end{bmatrix}
=
\left[
\begin{array}{cc|c}
-\frac{R_s}{L_{\alpha_{ps}}} & 0 & -\frac{\lambda'_{f_{\alpha_{ps}}}}{L_{\alpha_{ps}}} \\
0 & 0 & 1 \\
\frac{K_{ix}}{m} & \frac{K_x}{m} & 0
\end{array}
\right]
\begin{bmatrix}
i_{\alpha_{ps}} \\
x \\
\dot{x}
\end{bmatrix}
+
\begin{bmatrix}
\frac{1}{L_{\alpha_{ps}}} \\
0 \\
0
\end{bmatrix}
v_{\alpha_{ps}}
$$

This state space model has three states of which only the suspension current component $i_{\alpha_{ps}}$ is measured using a sensor. A partition between the measured and unmeasured states is indicated by the lines seen in the state vector.

We experimented with both full-order and reduced-order state observers for radial position estimation. The estimated outputs of the observers, in particular the linear displacement $\hat{x}$, did seem to converge onto the measured radial position signals in both simulation and practice. However, attempts at

using the estimated position for feedback destabilized the suspension control in practice causing the rotor to crash.

A number of strategies were experimented with to attempt to achieve successful levitation using the estimated position. We summarize those strategies in the following bullet points

- The transition from sensor-based feedback control to observer-based control was done in a gradual manner by computing the position signal used for feedback control x_{fb} as a weighted sum of the measured and estimated position signals, x and $\hat{x}$ respectively

$$x_{fb} = w_1 x + w_2 \hat{x}$$

  where the weights w_1 and w_2 were assigned using a complementary filtering approach.

- We experimented with voltage control and the classical current control architecture. Technically speaking both are voltage-controlled as they produce voltage commands for regulating the stator winding currents but the difference lies in the control implementation. The current control scheme consists of a nested control structure with an inner current loop and an outer motion control. The dynamics of the inner current loop are neglected when designing the motion controller with current being treated as the plant input. In contrast, the voltage control scheme uses a full-state feedback control structure where the current is treated as a state variable and voltage is the input to the plant. The voltage control architecture is shown to be more robust and easier to stabilize in [76].

- Different controller and observer tunings were experimented with for both controller and observer implementations.

However, despite these attempts, radial position sensorless operation was unsuccessful and requires a more thorough investigation and will not be discussed further.

Chapter 3

Hardware Design

This chapter provides a comprehensive review of the hardware developed for this thesis. We begin by presenting a brief background on the reference bearingless motor and the off-the-shelf setup used for motor control, highlighting their limitations and justifying the need for a custom motor drive. The chapter proceeds with a detailed examination of the developed multiphase motor drive, covering power distribution, sensing schemes, controller selection, and PCB design.

3.1 Overview of Previous Experimental Setup

Figure 3.1 shows the experimental setup used by former graduate student Simon Szoke in his MASc research. The setup includes a homopolar bearingless slice motor and the associated controllers and power electronics employed for its control.

3.1.1 Homopolar Bearingless Motor

The presented motor is a homopolar bearingless slice motor with a solid steel reluctance rotor, a flat stator winding structure, and a quadruple three-phase combined winding scheme. This motor was primarily based on Dr. Noh's previous work as for his PhD thesis [53] with a number of proposed changes focused primarily on improving the power density and efficiency of the machine. These changes include novel stator and rotor designs, a transition from using linear power amplifiers to switching power amplifiers, and a shift from a separated winding scheme to a combined multiphase winding scheme. A CAD rendering of the homopolar bearingless motor is presented in figure 3.2.

A circular permanent magnet Hallbach array placed along the tips of the stator teeth establishes a homopolar bias flux in the air gap. Suspension

Figure 3.1: Former experimental setup [72].
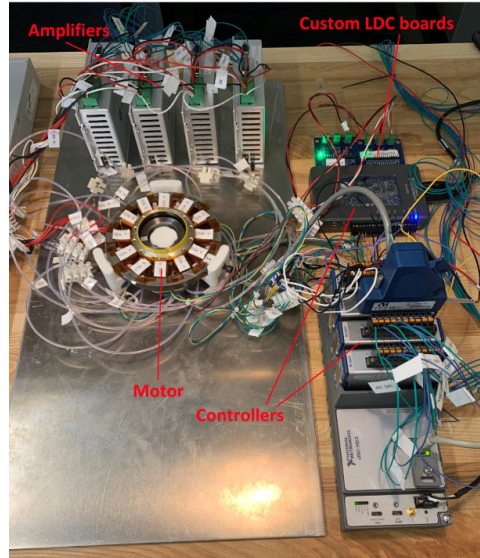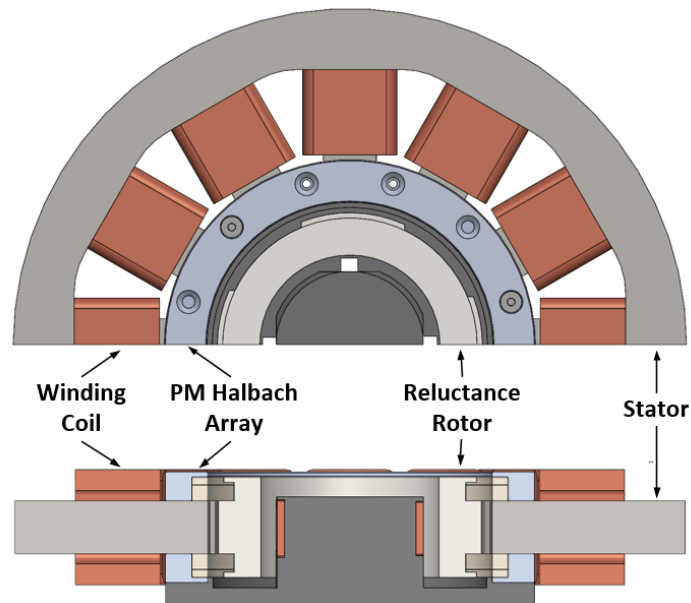

Figure 3.2: Prototype homopolar bearingless motor cross-section.

Figure 3.3: Engineering drawing of reluctance rotor [72].

regulation is achieved by superimposing a two-pole flux to perturb the symmetric air gap flux distribution, thereby imparting a net force on the rotor. The elimination of the magnets from the rotor allows for a cheap and disposable rotor construction that is well suited for operation at high speeds where quadratically increasing centrifugal forces present problems to rotors with embedded slots and brittle magnets.

The rotor features four salient teeth distributed symmetrically along the circumference of the rotor. These teeth modulate the bias airgap flux with an 8-pole field component. From a torque generation standpoint, the resulting field distribution resembles that of an 8-pole rotor that can be rotated using a synchronously rotating 8-pole field generated by the stator windings. A detailed drawing of the rotor is presented in Figure 3.3.

The stator has 12 slots with a simple winding arrangement consisting of 12 concentrated coils connected as 4 sets of three-phase windings with 4 different isolated neutral points. This winding configuration is capable of generating 2, 4, 8, and 10-pole fluxes and was designed to accommodate different bearingless motor architectures. An identical stator was used by former UBC graduate student Taryn Loutit in her MASc research on a dipole interior permanent magnet bearingless motor which uses a 2-pole field for torque generation and a 4-pole field for suspension force generation. Comprehensive details on the design and construction of the stator and
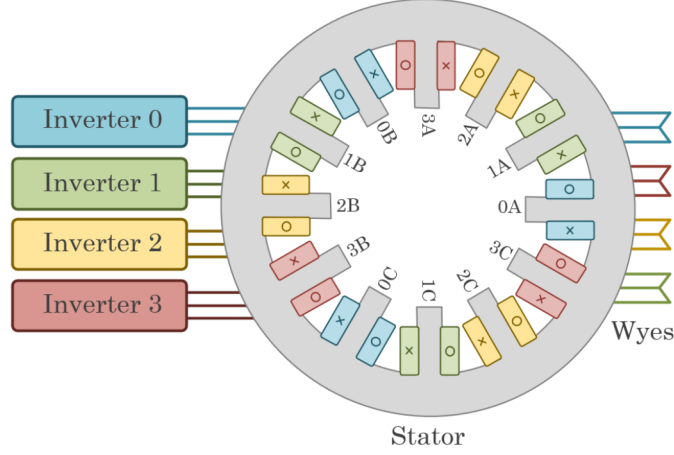
Figure 3.4: Bearingless motor winding scheme [38].
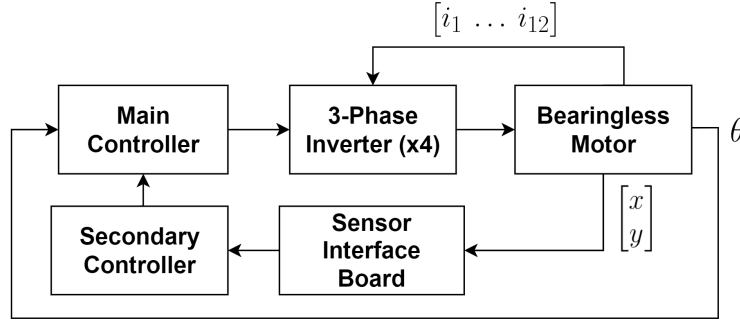
Figure 3.5: Previous system architecture.

rotor can be found in their MASc theses [38, 72]. An illustration of the stator winding scheme is presented in Figure 3.4.

3.1.2 Motor Control System

The previous motor control system architecture is depicted in Figure 3.5. Two separate controllers were used due to a lack of sufficient I/O: a main controller (cRIO 9068) and a secondary controller (myRIO 1900). Additionally, 4 off-the-shelf three-phase PWM switching amplifiers (VSA1-510) were used for regulating the phase winding currents.

The main controller receives measurements of the radial and angular po-

sitions of the rotor. The angle measurement is fed directly to the main controller via analog Hall effect sensors while the radial position information is sent to the main controller through the secondary controller. The main controller implements the motion control algorithms and sends reference current commands to the inverters which regulate the currents in the windings of the machine to control the suspension and rotation of the rotor.

This multi-controller architecture has a number of drawbacks such as an underutilization of the secondary controller, increased wiring complexity and cost, and most importantly a lack of access to phase current measurements which restricts possibilities for research.

Therefore, to support research on combined winding bearingless motors we developed a custom multiphase motor drive solution. This custom design integrates the controller, sensor interface, and power electronics into a single system to facilitate research on multiphase machines. By doing that we are able to simplify the previously used architecture by combining the functions of the controllers and the power electronics into a single flexible prototyping platform.

3.2   Multiphase Motor Drive Platform

3.2.1   System Overview

Figure 3.6 presents the overall system architecture of the proposed design. The system consists of a printed circuit board (PCB) assembly and an embedded controller (sbRIO-9627, National Instruments) that together form a reconfigurable motor drive platform for multiphase motor research. The PCB is laid out as shown in Figure 3.7. The design implements a multiphase half-bridge inverter topology consisting of 12-phase modules connected across a common DC bus. The high and low-voltage power supplies module provide filtered and regulated power to the isolated high and low-voltage sections of the board respectively. The DC-link voltage sense module monitors the DC-bus voltage protection purposes. The system additionally interfaces with external motion sensors enabling feedback motion control.

3.2.2   FPGA-Based Controller

Controlling the multiphase windings of a bearingless motor requires the simultaneous execution of multiple tasks with precise temporal control. These tasks include 1) sampling and filtering phase current, DC-link voltage, and
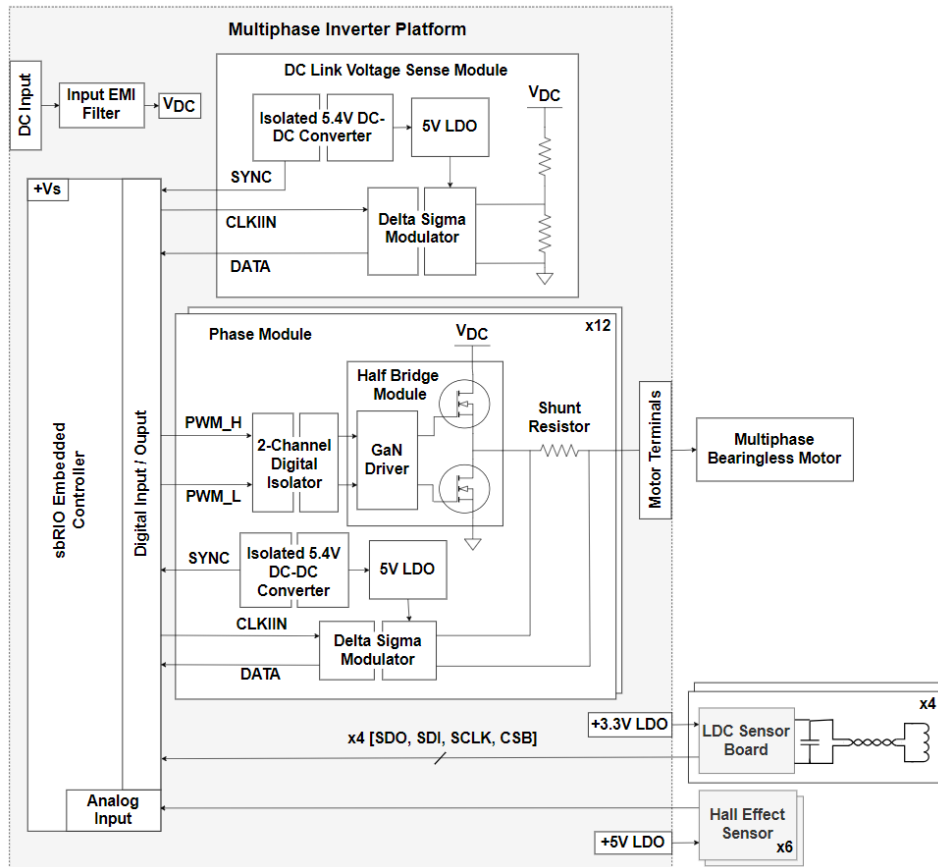
Figure 3.6: System overview.
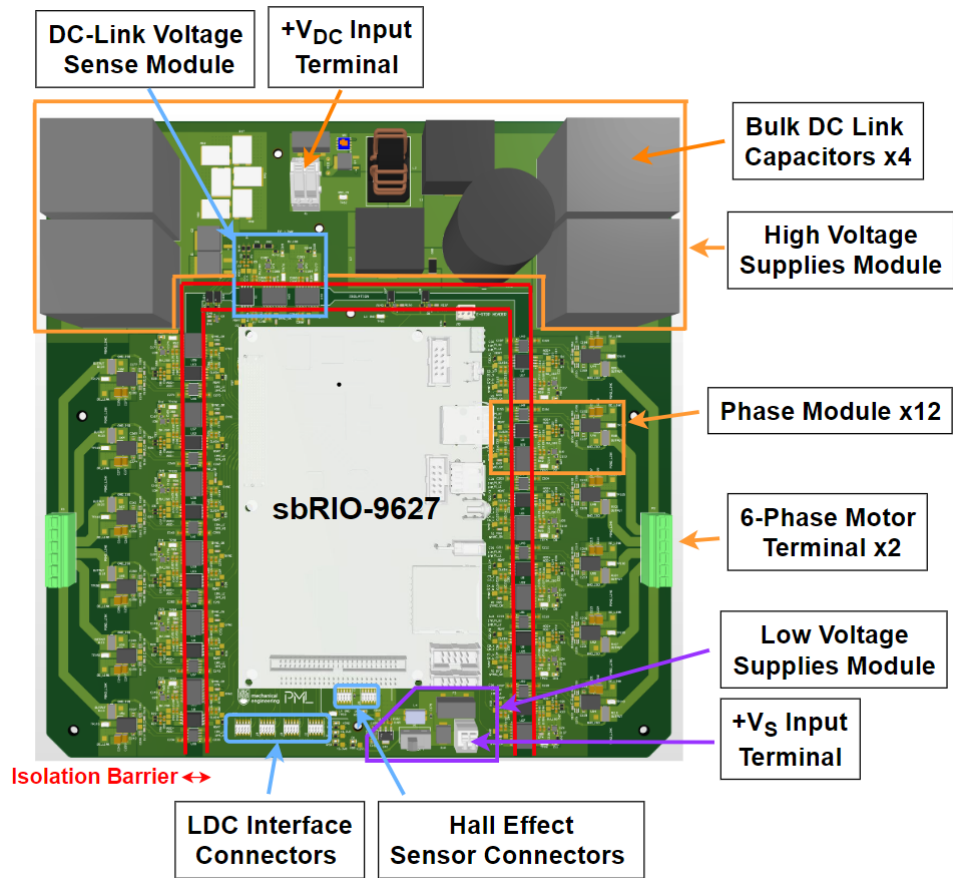
Figure 3.7: CAD rendering of motor drive platform.

motion sensor data, 2) implementing computationally intensive control algorithms, and 3) generating high-frequency PWM control signals for power switches. The FPGA embedded within the sbRIO controller enables this level of control, providing high processing speeds, true parallel capabilities, and temporal determinism.

The sbRIO interfaces with the inverter board via a high-density connector (SEAM-40-03.0-S-06-2-A-K-TR, Samtec). In addition to having pins dedicated for power and ground, the connector provides direct access to the FPGA digital I/O lines for transmitting control and clock signals and receiving digital data. To ensure signal integrity, high-speed PCB design techniques were employed due to the short rise times of these signals.

The sbRIO offers a total of 96 digital I/O pins, of which 90 are being used for the following functions

1. **12 Phase Modules:** 60 pins total (5 per phase module)

   - 2 output pins for complementary PWM signals

   - 1 input pin for phase current data

   - 1 output pin for modulator clock signal (20 MHz)

   - 1 output pin for DC/DC converter clock signal (16 MHz)

2. **DC Link Voltage Sense Module:** 2 pins

   - 1 input pin for DC link voltage data

   - 1 output pin for modulator clock signal

3. **Precharge and Discharge Modules:** 4 pins

   - 1 output pin for main MOSFET control signal

   - 1 output pin for precharge MOSFET control signal

   - 1 output pin for discharge MOSFET control signal

   - 1 input pin for e-stop status signal

4. **Radial Position Sensors Interface:** 24 pins total (6 pins per sensor)

   - 4 pins for SPI bus

   - 1 output pin for reference clock signal

   - 1 pin reserved for potential future use

Additionally, 6 analog input pins are used for interfacing with Hall effect sensors used for rotor angle estimation.

The sbRIO controller incorporates a real-time processor and an FPGA both of which can be programmed using an intuitive graphical programming language (LabVIEW). Time-critical tasks running at high loop rates are implemented on the FPGA to ensure reliable and deterministic execution. Low-priority tasks running at lower sampling rates such as data acquisition, and user interface are offloaded to the real-time processor to free up FPGA resources.

3.2.3   Power Distribution and Conversion

As shown in Figure 3.7, the board is partitioned into two sections separated by an isolation barrier. The low-voltage section positioned inside the barrier houses the controller and sensing peripherals for interfacing with external motion sensors. The high-voltage section, located outside the isolation barrier, contains the DC link filter stage and the power electronics. This barrier serves as a safety mechanism by isolating parts of the system that operate on different common-mode voltage levels to protect lower-voltage components from potential damage. It also helps improve immunity against noise sources like ground loops and switching transients from motor control circuitry which may cause errors in data communication. The isolation barrier is made possible through the use of components with on-chip digital isolation. These components require two separate supplies on either side of the barrier to power the isolated circuitry within the IC.

Low Voltage Supplies Module

The low-voltage side of the board accepts an external 10-30V input (V_s) used for powering the sbRIO controller. A common mode choke and a transient voltage suppressor are connected to the voltage rails as per the guidelines outlined in the controller datasheet. The sbRIO device filters and regulates the supplied power and provides 5V and 3.3V for powering digital devices on the low-voltage side of the board. An LDO regulator (UA78M05, Texas Instruments) is used to generate a separate analog 5-V rail from V_s. Another LDO regulator (TPS70933, Texas Instruments) is used to generate a 3.3-V rail from the 5-V rail. These derived voltage rails are used to provide power to angular and radial position sensors external to the board. A schematic of the low voltage supplies module is presented in Figure 3.8.
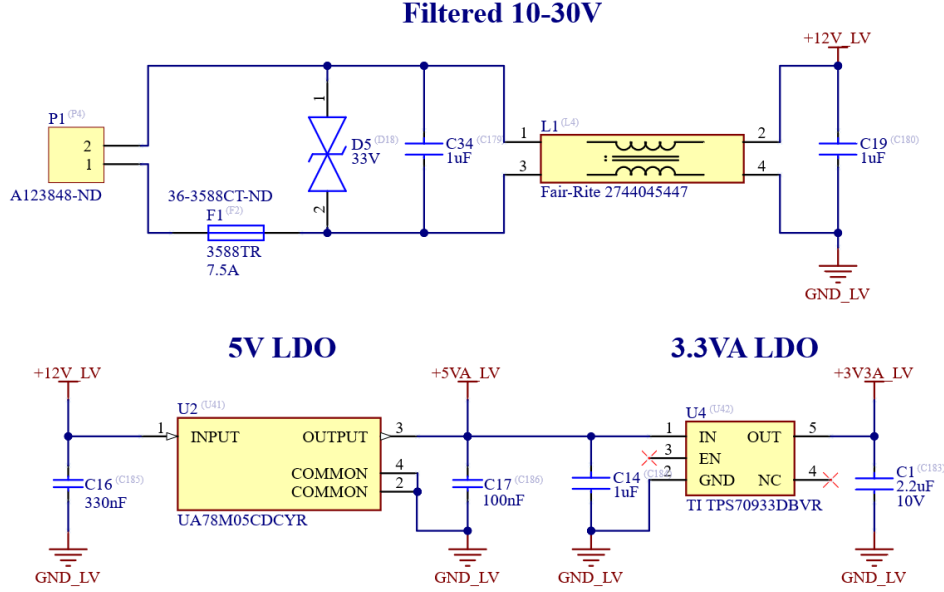
Figure 3.8: Low voltage supplies schematic.

High Voltage Supplies Module

The high-voltage side of the board features a primary high-voltage rail supplied by an external DC voltage source, providing a variable DC bus voltage for the inverter DC-link stage. An input filter connects to the high-voltage rails serving two primary purposes. Firstly, it helps supply the high-frequency components present in the discontinuous DC link current, thereby smoothing out the current draw from the power source. Secondly, the filter helps stiffen the DC bus voltage by minimizing voltage fluctuations caused by transient load changes and PWM switching actions.

In order to prevent large inrush currents when charging the downstream DC bus capacitors during startup a precharge circuit is used. This circuit plays a critical role in high-voltage systems by preventing premature tripping of any protection devices and thereby extending the lifetime of the system. A discharge circuit is also used to safely discharge the energy built up in the capacitor allowing for a controlled shutdown procedure.

Additionally, a 5.4-V isolated DC-DC converter (R05CT05S-R, Recom) supplies power to an LDO regulator (LP5912, Texas Instruments), generating
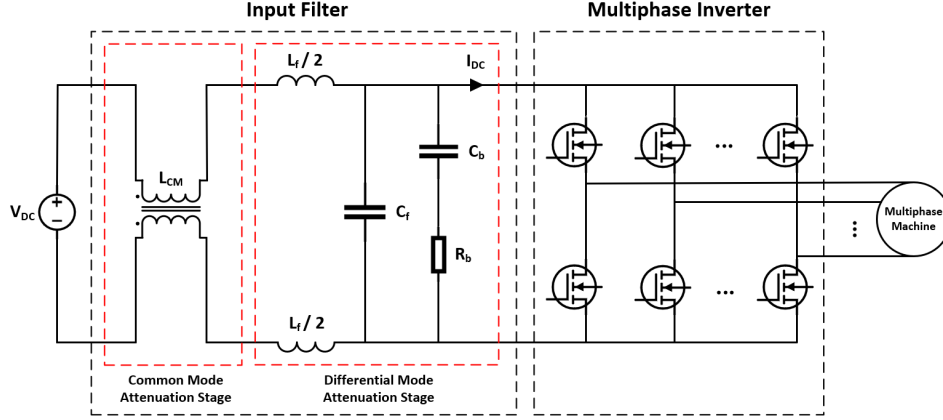
Figure 3.9: Input EMI filter topology.

an auxiliary 5-V rail with reference to the DC-link ground. This rail is utilized to power the digital isolators and gate drives of the half-bridge power stages, as well as an isolated delta-sigma modulator (AMC1306M25, Texas Instruments) employed for measuring the DC link voltage. The combination of the DC/DC converter and the LDO is replicated twice to meet the power demands of 12 digital isolators and 12 half-bridge power stages, with each instance providing power to half of these components.

Input Filter The input filter topology is presented in Figure 3.9. The filter consists of two stages designed to filter high-frequency differential mode and common mode currents respectively. Differential mode currents flow in opposite directions in the forward and return paths of the power supply and are responsible for power transfer. On the other hand, common mode currents flow in the same direction in both paths. These are unwanted currents that arise due to the rapid switching actions of the power electronic switches and flow through parasitic capacitances within the circuit. The presence of these currents may lead to electromagnetic interference issues with neighboring circuits and should be attenuated.

To suppress these undesired common mode currents, a common mode choke L_{cm} (7448042001, Wurth Elektronik) is used. This component presents high impedance to common mode currents, attenuating them, while allowing differential mode currents to pass through unaffected. The common mode choke has a 20 A current rating and a low DC resistance of 2.4 mΩ for low power dissipation during operation.

Suppression of the high-frequency differential mode current components is achieved using a second-order LC low-pass filter with a parallel damping branch consisting of a series RC network. The purpose of the parallel damping branch is to suppress the resonance and limit the peak output impedance of the filter in compliance with the Middlebrook stability criterion [19].

The filter capacitance C_f is comprised of the bulk DC link capacitors. This component plays a crucial role in providing a low-impedance path for conducting the high-frequency components present in the discontinuous DC link current. As such, these components must be rated to withstand the ripple current demands of the inverter. Attempts at arriving at analytical expressions describing the ripple currents of a switching inverter are presented in [41]. However, that approach is not practical and gets increasingly more complex for multiphase systems. As such we adopted a simulation-based approach where we used MATLAB to simulate the DC link current of a multiphase inverter in order to estimate the ripple current requirements needed for sizing the capacitors accordingly. The DC link current of an inverter is computed as the dot product of the phase current vector and the switching state vector as

$$I_{dc} = [i_1 \ldots i_{12}]^T \cdot [S_1 \ldots S_{12}]^T$$

where the switching state S_k of phase leg k is either 1 or 0 when the high-side switch is on or off respectively. The switching states are generated using a sinusoidal pulse width modulation technique. This entails comparing a set of multiphase sinusoidal reference signals with a high-frequency triangular wave ranging between -1 and 1. The amplitude of the reference signals is known as the duty cycle d which refers to the ratio between the phase voltage amplitude V_0 and half the available DC link voltage V_{dc}. Assuming a balanced load the corresponding multiphase sinusoidal phase voltages and currents are given as

$$v_k = V_0 \cos\left(\omega_e t - \frac{2\pi k}{n}\right) = d\frac{V_{dc}}{2}\cos\left(\omega_e t - \frac{2\pi k}{n}\right)$$
$$i_k = I_0 \cos\left(\omega_e t - \frac{2\pi k}{n} - \phi\right)$$

where I_0 and ω_e are the phase current's amplitude and frequency respectively, and ϕ is the phase difference between the phase voltage and current
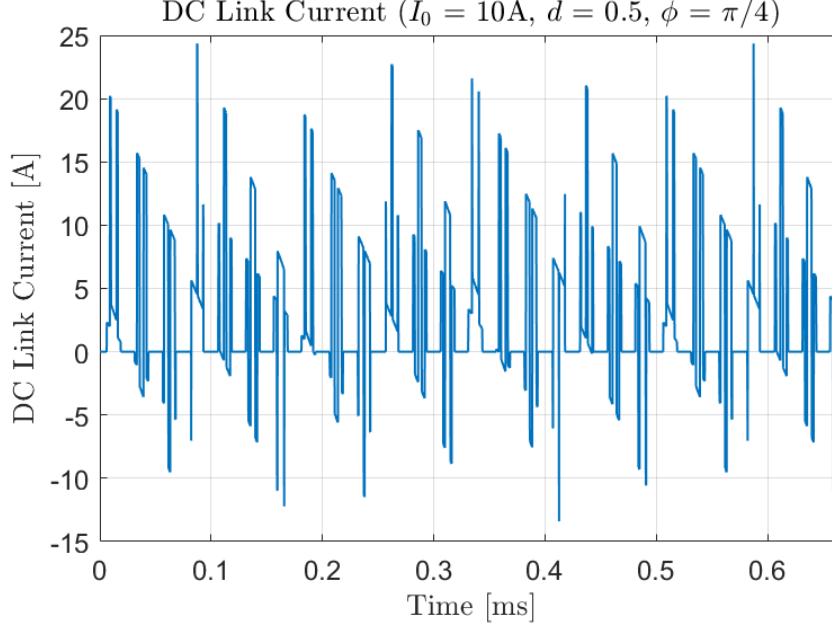
Figure 3.10: Simulated DC link current for 12-phase inverter.

waveforms.

Carrying out this procedure in MATLAB, an example plot of the DC link current for a 12-phase inverter is presented in Figure 3.10. This plot demonstrates the highly complex nature of the DC link current and the need for a simulation-based approach for its estimation.

Assuming the capacitor conducts the AC portion of this current we can arrive at a worst-case ripple current rating for selecting the capacitors. Assuming operation under fully loaded conditions where $I_0 = I_{max} = 10$ A, we can plot the RMS ripple currents for varying duty cycles and phase differences. This plot is presented in Figure 3.11. The worst-case conditions occur at a phase difference of $\phi = \pi/2$ and a duty cycle of approximately 0.55 where the capacitors can conduct up to 17 A. Therefore, our DC link capacitors must be able to withstand that.

Another important consideration in the selection of the capacitor is the allowable DC link voltage ripple during operation. Reference [79] proposes a simple guideline for sizing the DC link capacitance for a worst-case scenario that exhibits the highest peak-to-peak voltage ripple Δv_{pp}^{max} as
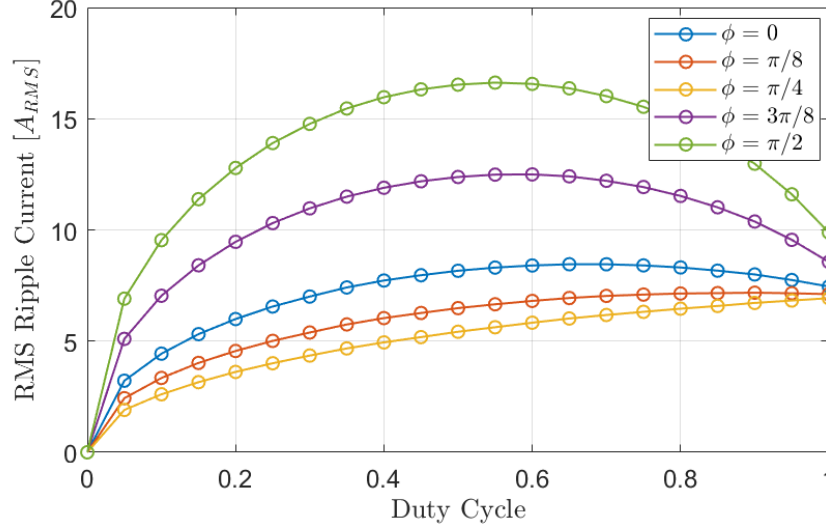
Figure 3.11: Simulated RMS ripple current for 12-phase inverter.

$$C_f \geq \frac{I_0}{4\Delta v_{pp}^{max} f_{pwm}}$$

Evaluating this expression for the maximum load current condition of 1 0A, a target PWM frequency of 20 kHz, and a maximum allowable voltage ripple of 0.5 V yields a lower bound of 250 μF for the DC link capacitance. It is important to note that this expression was derived for a three-phase inverter, but the analysis was extended to more phases in later publications from the same authors [77, 78]. Their findings indicated that increasing the number of phases decreases the size of the voltage ripple, suggesting that the calculated minimum capacitance is slightly oversized and safe.

Another important criterion in the selection of the capacitor is its voltage rating. In addition to being able to support the maximum voltage rating of the power switches, the capacitor must be able to withstand any voltage surges arising from transient load changes that cause energy to flow back into the DC bus. This is particularly important during flux weakening operation, where the occurrence of a fault results in a scenario in which the back emf of the motor exceeds the DC bus voltage causing energy to flow back into the capacitors.

The final capacitance of $C_f = 360$ μF was realized using 4 identical film capacitors in parallel (C4AQLBW5900A3OK, Kemet). Each capacitor has a voltage rating of 500 V and a ripple current rating of 35 A_{RMS}. Film capacitors are used for their high ripple current ratings, high voltage ratings, low parasitics, and long lifetimes. Although film capacitors are more expensive and have a lower capacitance per unit volume (energy density) than the more widely accepted aluminum electrolytic capacitors on a part-by-part basis, using them in a capacitor bank to meet the high ripple current demands of inverters results in designs that are overall smaller, lighter, and more cost-efficient. That said, exclusively relying on a single technology often leads to oversized and suboptimal designs. For instance, capacitor banks consisting of only film capacitors are usually well within the ripple current requirement while marginally satisfying the ripple voltage requirement, while the opposite is true for electrolytic capacitor banks. To address this, hybrid capacitor bank designs that combine the advantages of both technologies can be considered.

Having selected the capacitance C_f, the inductance $L_f = 200$ μH was chosen to realize a filter with an approximate -3dB bandwidth of 1400 rad/s, providing 60dB of attenuation of the current harmonics at the target PWM switching frequency (20 kHz). The total inductance is distributed evenly on the forward and return paths as shown in Figure 3.9. This is done to maintain balance between the two lines which aids in the attenuation of common mode noise. The individual inductors (74437529203101, Wurth Elektronik) have an inductance of 100 μH, a DC resistance of 22.9 mΩ and a maximum current rating of 11.2 A.

The parallel branch consists of the series combination of a damping resistor R_b and a large blocking capacitor C_b. The damping resistor serves to limit the peak output impedance of the filter at the cutoff frequency, while the blocking capacitor prevents DC currents from flowing through the damping resistor to prevent power dissipation in the resistor. The components of the parallel damping branch are selected according to the design procedure outlined in Chapter 10 of [19].

The Middlebrook stability criterion states that the output impedance of the input filter $Z_o(j\omega)$ should be less than the input impedance of the switching converter. Assuming the inverter has the same input impedance characteristic as a buck converter, this condition can be expressed as follows

$$Z_o(j\omega) < \frac{R_s}{d^2}$$

where R_s is the winding resistance and d is the duty cycle ratio. It is important to note that there is some uncertainty regarding the validity of this assumption, which may necessitate further investigation and potential revision.

Using the measured phase winding resistance of 0.4 Ω and a worst-case scenario where $d = 1$ sets our maximum possible output impedance as 0.4 Ω. Aiming for a maximum filter output impedance of $||Z_o||_\infty = 0.3$ Ω the ratio between the capacitors $n = {C_b}/{C_f}$ can be computed as

$$n = \frac{L_f}{C_f||Z_o||_\infty^2}\left(1 + \sqrt{1 + 4\frac{C_f||Z_o||_\infty^2}{L_f}}\right) = 18.3$$

The blocking capacitor C_b is therefore required to have a value of $nC_f = 6.6$ mF. Finally, the damping resistance R_b can be computed as

$$R_b = \sqrt{\frac{L_f}{C_f}}\sqrt{\frac{(2+n)(4+3n)}{2n^2(4+n)}} = 0.244\Omega$$

The final damping resistor (CSRL3-0R2F8, Riedon) and blocking capacitor (SLPX682M100H9P3, Cornell Dubilier Electronics) were chosen as $R_b = 200$ mΩ and $C_b = 6.8$ mF. An aluminum electrolytic capacitor was used owing to its large capacitance per unit volume and its relatively high equivalent series resistance (39 mΩ) which contributes to the overall damping resistance value. This parallel branch conducts minimal currents during operation and thus the power rating of the resistor and the ripple current rating of the capacitor were less critical during selection.

The final filter schematic is presented in Figure 3.12. LTspice circuit simulations were used to validate the performance of the finalized filter. The simulation setup is shown in Figure 3.13. The current source denoted as I1 in the figure represents the DC link current and is modeled using the phase leg switching functions, identical to the approach carried out in MATLAB. Moreover, the simulation accounted for the effects of component parasitics on the high-frequency performance of the filter to ensure the filter performs as intended in practice.
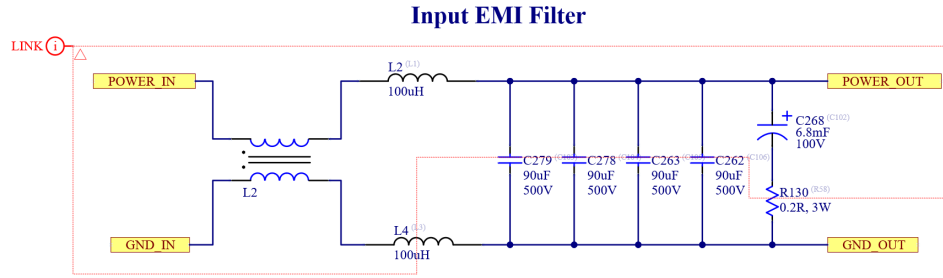
Input EMI Filter

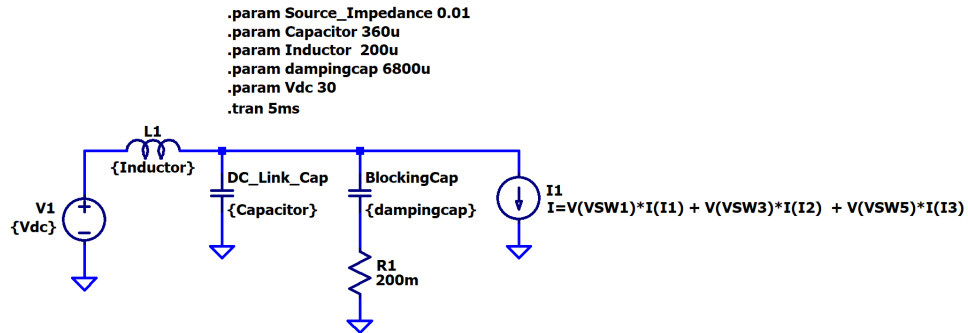Figure 3.12: Input EMI filter circuit schematic.

Figure 3.13: Input filter circuit LTspice simulation setup.

Precharge and Discharge Modules   The precharge circuit is presented in Figure 3.14. It consists of two parallel paths feeding the inverter: a main path and a precharge path. Both paths contain power MOSFETs acting as switches. The precharge path additionally contains a positive temperature coefficient (PTC) thermistor which acts as a current-limiting resistor that slows down the rate at which the capacitors charge during the precharge procedure. The precharge path is bypassed during normal operation. The key selection criteria for choosing the power MOSFETs are their voltage and current ratings and their drain-source on-resistance (R_{dson}). The main path MOSFET (XPW6R30ANB, Toshiba), responsible for conducting the power supply currents during normal operation, is rated for 100V and 45A and features a low (R_{dson} of 5 mΩ enabling efficient operation with low power dissipation. The precharge MOSFET (STD11N60DM2, STMicroelectronics) is only on for short durations of time making efficiency less critical in its selection.

The discharge path uses a bank of resistors with a dual depletion type MOSFET (IXTA3N50D2, IXYS) configuration for redundancy. That way if a single MOSFET fails shorting the source to the drain the second MOSFET maintains an open circuit to prevent unwanted discharge and power dissipation. The resistor power bank consists of 6 parallel 45 W, 200 Ω resistors (TKH45P200RFE-TR, Ohmite), and is capable of safely dissipating 100 W. The discharge circuit is presented in Figure 3.15. The potential use of the resistor power bank to dissipate regenerative energy during motor deceleration or braking has not been investigated but is worth consideration for preventing the DC bus voltage from reaching excessive levels and potentially causing overvoltage fault scenarios.

The operation of the precharge and discharge circuits is controlled via control signals from the FPGA. The signals are routed across the isolation barrier using photovoltaic MOSFET drivers (APV2111V, Panasonic). Since the digital I/O of the FPGA does not supply enough current to power the MOSFET drivers, additional small signal MOSFETs (2N7002ET1G, onsemi) are used for that purpose. The drains of the small signal MOSFETs are supplied by the digital 3.3V rail established by the sbRIO via an E-Stop button with normally closed contacts. The status of the E-Stop button is monitored by the controller. In the case of an emergency, the normally closed contacts open cutting off power to the small signal MOSFETs. This loss of power causes both the main and precharge paths to open and initiates a shutdown sequence.
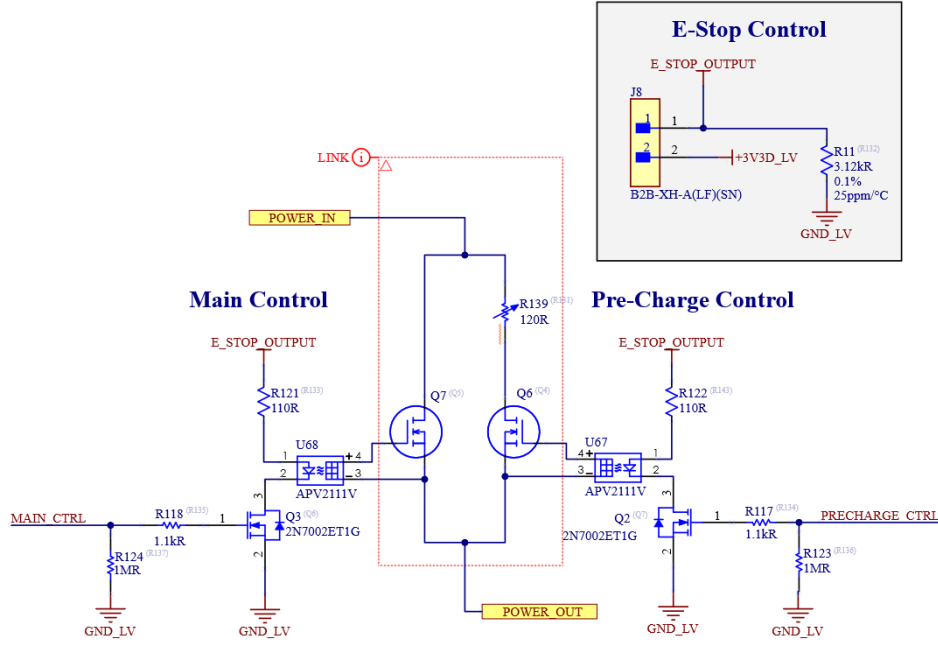
Figure 3.14: Precharge circuit.

The operation of the precharge and discharge circuits during startup and shutdown is outlined as follows:

- When the system is unpowered the depletion-type discharge MOS-FETs are in a normally closed state which discharges any residual voltage in the DC bus capacitors.

- Upon starting up the depletion type MOSFETs are opened and the precharge MOSFET is closed while the main MOSFET are kept in an open state.

- After the DC Bus capacitors are charged up to DC link voltage, the precharge MOSFET is opened shortly followed by the closing of the main MOSFET bypassing the precharge path.

- Upon shutdown the precharge MOSFET is opened and the discharge MOSFETs are returned to the normally closed state to discharge the bus capacitors through the resistor bank.
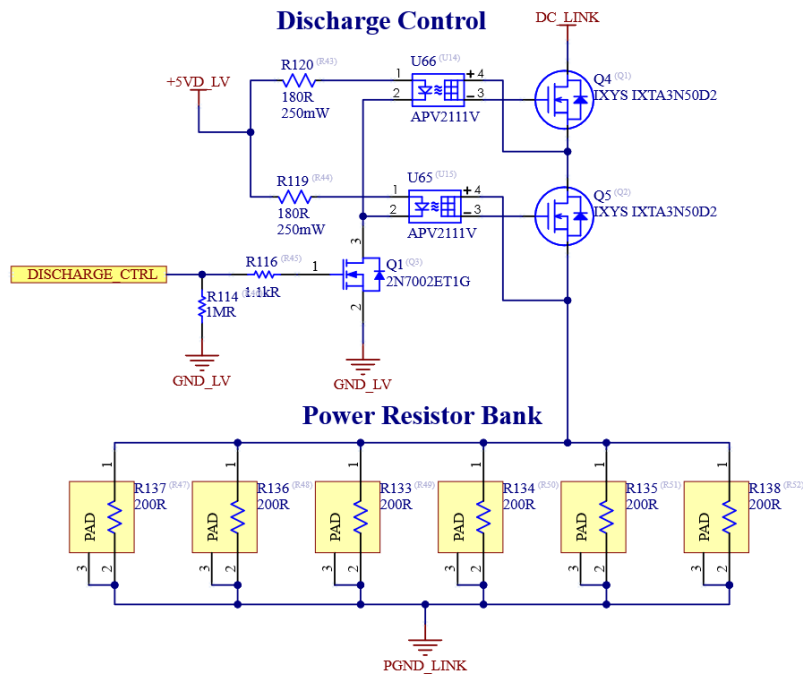
Figure 3.15: Discharge circuit.
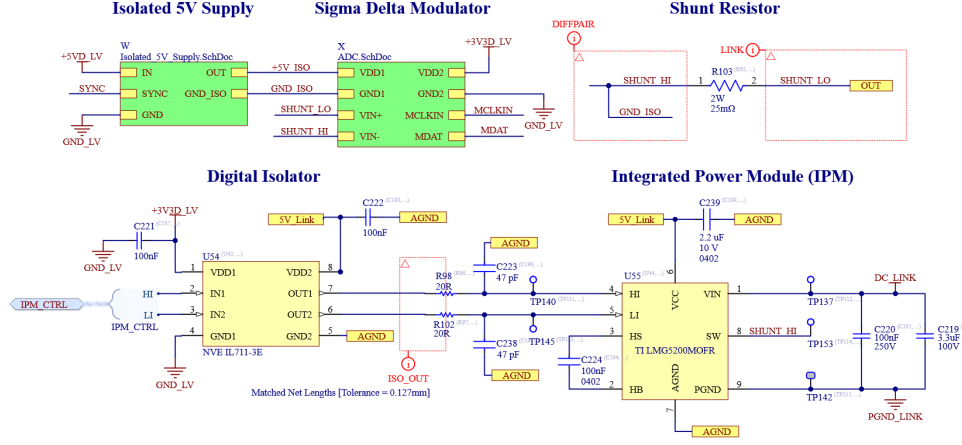
Figure 3.16: Phase module schematic.

Phase Module

The phase module combines all the necessary components to form a single phase of the half-bridge inverter and to monitor the current through that phase for control and protection purposes. An integrated 80-V, 10-A GaN half-bridge power stage (LMG5200, Texas Instruments) is used as the primary building block for this module. The choice of GaN-based power devices was motivated by their recent commercial availability and distinct advantages over traditional silicon-based alternatives.

Within each phase module, key components include the GaN power stage, a 25 mΩ, 0.1% tolerance, 2 W, current shunt (FCSL64R025DER, Ohmite), a 2-channel digital isolator (IL 711-3E, NVE Corp), a second-order isolated delta-sigma modulator (AMC1306M25, Texas Instruments), an isolated 5.4-V DC-DC converter (R05CT05S-R, Recom), and a 5-V LDO regulator (LP5912, Texas Instruments). A schematic of the phase module and the corresponding PCB layout are presented in Figures 3.16 and 3.17 respectively.

Wide bandgap semiconductor devices such as GaN transistors are capable of very high switching speeds resulting in reduced switching losses and higher overall efficiencies and power densities than traditional silicon FETs which typically require large heatsinks to dissipate excess heat [42]. However, the very fast slew rates of GaN devices (up to 50 V/ns) present a number of engineering challenges concerning circuit layout and electromagnetic com-
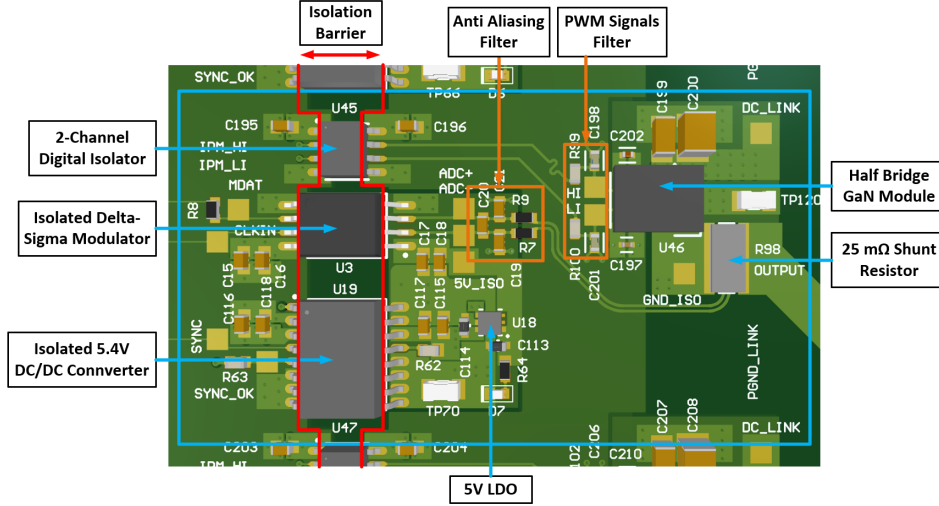
Figure 3.17: Phase module PCB layout.

patibility (EMC) that make this technology difficult to adopt and work with. The LMG5200 helps mitigate these challenges by encapsulating the GaNFETs along with all the necessary gate drive electronics in a single optimized package that simplifies layout design. The LMG5200 features a built-in bootstrap circuit to generate the high-side bias voltage needed for driving the high-side FETs. It additionally incorporates a number of protection features such as an under-voltage lockout feature that ignores the input PWM signals when the voltage of the gate drive supply rails falls below a certain threshold. Further details can be found in the product data sheet.

The 2-channel digital isolator transmits the PWM signals across the isolation barrier to the high and low-side gate drive circuits contained within the half-bridge power stage. The complementary PWM signals are low-pass filtered using a passive RC network to reject high-frequency noise and avoid the possibility of false switching. The traces for these signals are also carefully length-matched in the PCB layout to ensure signal timing consistency and minimize propagation delay differences (i.e., skew) between the complementary signals.

In order to prevent the possibility of shoot-through, a dead time is introduced by delaying the rising edge of the PWM signals. Minimizing this dead time is particularly important for GaNFETs to minimize third-quadrant conduction losses which are comparatively higher than traditional silicon-

based FETs [71]. The deadtime resolution is dictated by the top-level PWM timer clock which is 100 MHz in our implementation resulting in a deadtime resolution of 10 ns. A dead time of 30 ns is used throughout our testing. This is sufficient to account for the maximum reported channel-to-channel skew (3 ns) of the digital isolator and the maximum propagation delay mismatch (8 ns) between the complementary PWM signals reported in the GaN power stage datasheet. Additionally, the digital isolators have a default low state to prevent shoot-through in the event of a component failure.

The isolated delta-sigma modulator is used to sense the phase currents by sampling the voltage across the 25 mΩ inline shunt resistor at a rate set by the externally provided reference clock signal (20 MHz). The output of the modulator is sent back to the controller where it is processed and used for feedback.

A resistance of 25 mΩ is chosen to ensure that at the nominal current operating range (± 10 A), the input voltage measured across the resistor lies within the linear operating range of the modulator (± 250 mV). The resistor is additionally rated to safely withstand thermal dissipation losses during peak current conditions ($I^2 R < 3$ W). Due to the small value of resistance (on the order of PCB trace resistances), a four-wire Kelvin connection is used to bypass the resistance of the current-carrying traces to minimize its effect on the current measurement.

An anti-aliasing filter is placed on the input terminals of the modulator to restrict the bandwidth of the input signal prior to sampling. The filter consists of passive components forming a low pass filter with an approximate cutoff frequency of 3.6 MHz.

In order to measure the differential voltage across the resistor while rejecting the common mode component, the isolated modulator is supplied by a floating 5 V rail which rides on the common mode voltage between the resistor terminals. To accomplish this, the isolated DC-DC converter generates a 5.4 V rail referenced to the half-bridge power stage output switch node. This floating 5.4 V rail is fed to an LP5912 LDO regulator which generates a low-noise floating 5 V reference used to power the high-voltage side of the isolated modulator.

The output switch node of the half-bridge power stage switches between V_{dc} and 0 V at a maximum slew rate of 50 V/ns and at a frequency set by the PWM switching rate. The high dv/dt transients of the floating reference bring about concerns regarding stresses on the isolation barrier of the dc/dc

converter and modulator. As such an important parameter in the selection of these components is their common mode transient immunity (CMTI) rating. This rating signifies the maximum tolerable rate of rise or fall of the common mode voltage applied between two isolated circuits. The isolated dc/dc converter and the isolated modulator both have a CMTI rating of 100 V/ns to withstand the 50 V/ns slew rates of the switch node.

We also investigated the possibility of using the bootstrap rails of the half-bridge power stage as the floating reference for the isolated modulator. However, concerns regarding its potential effects on the bootstrap operation discouraged us from pursuing this idea further. In future board revisions, reconsidering this idea could lead to reduced hardware complexity by eliminating the need for dedicated components to establish the floating reference. This change would result in substantial cost and footprint savings.

The phase module is replicated 12 times across the board. In order to address a concern we had during the design stage regarding beat frequencies resulting from slight variations in the switching frequencies of different DC/DC converters across different phase modules, we selected a DC/DC converter with a synchronization capability. Multiple converters can be synchronized using an external clock reference signal from the controller. This overrides the converter's internal oscillator and enables synchronization. However, during testing, this issue did not arise, likely because the converter outputs are isolated from one another. As a result, 12 digital pins reserved for the synchronizing clock signals are currently unused, and in future board revisions, these pins could be allocated for other purposes.

3.2.4   Sensing System

Effective control of bearingless motors relies on precise measurements of different quantities, including the currents flowing through the motor windings and the radial and angular positions of the rotor. To accomplish this, a shunt resistor coupled with an isolated delta-sigma modulator is used to precisely measure the motor phase currents. Additionally, the board provides connectors for interfacing with external radial and rotational position sensors, enabling feedback motion control. Furthermore, to monitor the DC bus voltage level and safeguard against fluctuations, our system incorporates DC link voltage sensing.

Inline Phase Current Sensing

Accurate phase current information is crucial for achieving good motor drive performance and protection. The two most common measurement methods for isolated current sensing are either using a shunt resistor or a Hall-effect sensor. The latter provides inherent galvanic isolation and a higher current measurement range but suffers from nonlinearity over that wide range and is more susceptible to external noise and temperature-induced drift as compared to the shunt resistor approach [39]. The main drawback of the shunt resistor approach is the thermal dissipation and power loss which can distort the measurements at higher currents. However, the isolated modulator has a small input range of $\pm 250\,\mathrm{mV}$ which allows the selection of a small valued resistor with minimal thermal dissipation without having to compromise the resolution and dynamic range of the measurement. All these factors make the shunt resistor approach the optimal choice for a relatively low-power multi-phase inverter with a limited current range ($\pm 10\,\mathrm{A}$).

Inline phase current sensing is achieved by inserting the shunt resistor between the output switch node of the half-bridge power stage and the terminals of the motor. This inline measurement approach is favorable as it outputs a continuous signal that is directly proportional to the phase current. On the other hand, measuring current in other locations, such as the low side of each phase, requires additional processing to produce meaningful phase current data needed for feedback control.

The isolated sigma-delta modulator (AMC1306M25, Texas Instruments) oversamples the voltage across the shunt resistor at a rate set by the externally provided reference clock signal ($f_s = 20$ MHz) and synchronously generates a bitstream whose temporal distribution is correlated with the measured input. The high-frequency bitstream is routed to the FPGA where a digital decimation filter is used to reconstruct the measured voltage signal.

The combination of the sigma-delta modulator and the digital decimation filter is referred to as a sigma-delta ADC. This architecture is particularly advantageous for performing isolated current measurements in multiphase systems as we are able to achieve true simultaneous sampling of all phase currents using relatively cheap digital I/O without the need for expensive multi-channel simultaneous analog input modules. Additionally, this architecture performs the functions of an amplifier and an ADC while transferring the processing stage to the digital domain. This offers improved flexibility and precise temporal control which is useful for prototyping. However, it
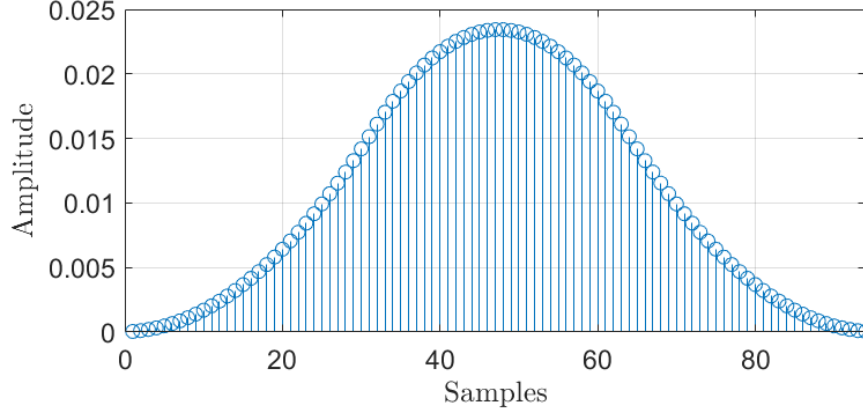
Figure 3.18: SINC^3 filter impulse response $M = 32$.

should be noted that compared to the more commonly known successive-approximation-register (SAR) ADCs, sigma-delta ADCs exhibit a latency equal to half of the digital filter impulse response length.

A digital filter that is commonly used in conjunction with the second-order sigma-delta modulator is the SINC^3 filter where the superscript refers to the order of the filter. The filter gets its name from its frequency response which resembles a sinc function. This filter has the following transfer function

$$H(z) = \left(\frac{1}{M} \cdot \frac{1 - z^{-M}}{1 - z^{-1}} \right)^3 \qquad (3.1)$$

where M is the downsampling or decimation ratio between the modulator sampling frequency ($f_s = 20$ MHz) and the desired output data rate. Although not immediately obvious, this is an FIR filter with an impulse response length of $L = 3M - 2$. The impulse response of a SINC^3 filter with a decimation ration of $M = 32$ is presented in Figure 3.18. This filter can be implemented in software using a linear convolution sum followed by a downsampling stage by carrying out the following difference equation

$$y[k] = \sum_{n=0}^{3M-1} h[n] \, x[k - n]$$

where $x[\cdot]$ is the modulator output data bitstream, $h[n]$ are the filter coef-

65

M

x(n)	Integrator $1/(1-z^{-1})$	Integrator $1/(1-z^{-1})$	Integrator $1/(1-z^{-1})$		Differentiator $1-z^{-1}$	Differentiator $1-z^{-1}$	Differentiator $1-z^{-1}$	y(m)

1 f_S

p $F = f_S/M$

Figure 3.19: SINC^3 filter topology [27].

ficients, and $y[k]$ is the decimated output. The effective resolution of the output $y[k]$ is dependent on the filter's impulse response length and thus on the decimation ratio. A high decimation ratio results in a high-resolution measurement at the expense of a higher latency.

Alternatively, the filter can more simply be realized as a cascaded network of three integrators and three differentiato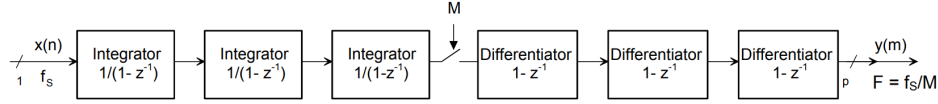rs as interpreted by the filter's transfer function. This is also known as a cascaded integrator comb (CIC) filter and can be efficiently implemented without multipliers, utilizing only adders and subtractors. The integrators are running at the modulator sampling rate f_s. The output of the integration stage is then downsampled by a factor equal to the decimation ratio M and fed to the cascaded differentiators. In doing so the filter converts the over sampled 1-bit modulator data stream into a higher resolution digital word at a lower data rate (f_s/M). The filter structure is presented in Figure 3.19.

The phase current in a load driven by a PWM inverter features a switching-induced ripple. The presence of this ripple component in the measured current is undesirable as it may degrade the performance of the closed-loop current regulation. A widely accepted technique to reject this PWM switching-induced component while retaining the fundamental component of the current is the synchronized sampling method [20, 70]. This method works by synchronizing the current sampling instant with the midpoint of the zero voltage vector. In a triangle-comparison PWM scheme, this corresponds to the peaks and valleys of the triangle carrier waveform. Doing so not only ensures that the current is being sampled at a point that is representative of its average over the switching period but also occurs at a point where the phase winding terminals are at the same potential, either zero or V_{dc}. This prevents abrupt transitions in the phase voltage from distorting the measurement.

This method works well for an ideal sample and hold ADC where we have precise control of the sampling instant. With a sigma-delta ADC, we can attempt to replicate this synchronized sampling performance by carefully

66
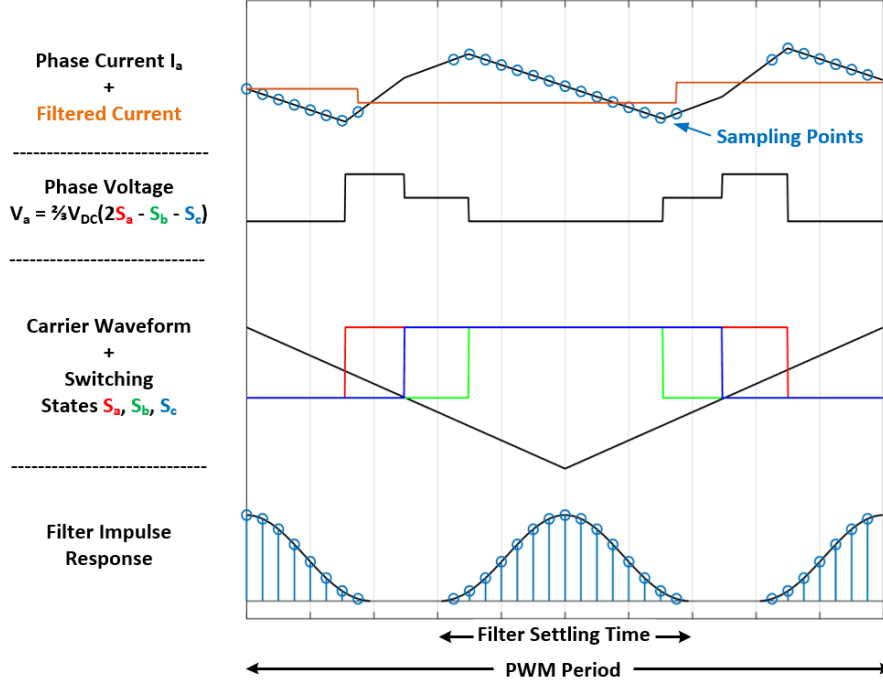
Figure 3.20: Intermittent SINC^3 filter operation.

operating the digital decimation filter in an intermittent manner to maintain synchronization with the inverter switching frequency. This operation is illustrated in Figure 3.20.

The filter is configured to only run for 3 decimation cycles (i.e. the filter's settling time or the length of its impulse response) around peaks and valleys of the triangle carrier waveform. This theoretically eliminates the switching harmonics from the measured current while retaining the average component needed to implement feedback control. The measurements are obtained twice per PWM period to extend the maximum achievable current control bandwidth. The effective resolution of the current measurement depends on the length of the filter's impulse response which is computed as $L = 3M - 2$ where the decimation ratio M is computed from the PWM frequency f_{pwm} such that $M = \mathrm{floor}\,(20\mathrm{MHz}/(2f_{\mathrm{pwm}})/3)$ to fit the filter's impulse response within a half PWM period. For instance, a 20 kHz PWM frequency results in an impulse response length of $L = 496$ and an ideal ENOB of approximately 16. Doubling the PWM frequency reduces the resolution by 2.5 bits.

The effectiveness of this approach in rejecting the PWM ripple is highlighted in Figure 3.21. The figure presents a comparison between two filter implementations: a continuously running filter that is not synchronized to the inverter switching frequency, and the intermittent implementation described earlier. The test was conducted with a 5 kHz PWM switching frequency, resulting in an impulse response length of $L = 1996$ for the intermittent filter implementation. The continuously running filter is configured with the same impulse response length for a fair comparison. The intermittent implementation provides a new current measurement at twice the PWM switching rate (10 kHz) while the continuous implementation does so at the filter's decimation rate i.e. 20 MHz$/M \approx 30$ kHz. Both current measurements were sampled in an acquisition loop running at 40 kHz to accommodate the different throughput rates of the two implementations. The results clearly show that the intermittent operation significantly reduces the noise levels in the measurement, effectively suppressing the PWM switching-induced ripple. However, this improvement comes at the expense of a lower throughput rate and an inherent tradeoff between the PWM switching frequency and measurement resolution. In contrast, the filter properties of the continuous implementation can be set independently of the switching frequency.

DC-Link Voltage Sensing

Feedback of the DC-link voltage is necessary to ensure that it remains within acceptable tolerances and to protect against overvoltage and undervoltage conditions. A high-impedance voltage divider network consisting of a series combination of resistors gradually scales down the DC-link voltage to fall within the input voltage range of the isolated delta-sigma modulator. The voltage divider is constructed using a single 309 Ω and two 49.9 kΩ 0.1% tolerance resistors. These values are chosen to ensure that at the maximum DC bus voltage condition of 80V the input voltage measured across the 309 Ω sense resistor lies within the linear operating range of the modulator ± 250 mV. The same antialiasing filter used with the modulators in the phase module is used to limit the bandwidth of the measured signal. To compensate for offset errors introduced by input bias current, an additional 309 Ω resistor is placed at the negative input terminal of the modulator, as recommended by the modulator datasheet. The scaled voltage is sampled using the isolated sigma-delta modulator and converted into a high-frequency serial bitstream. The output data bitstream is fed back to the FPGA where an identical SINC^3 filter reconstructs the sampled signal. The schematic of the DC link voltage sensing circuit is presented in Figure 3.22. Figure 3.23
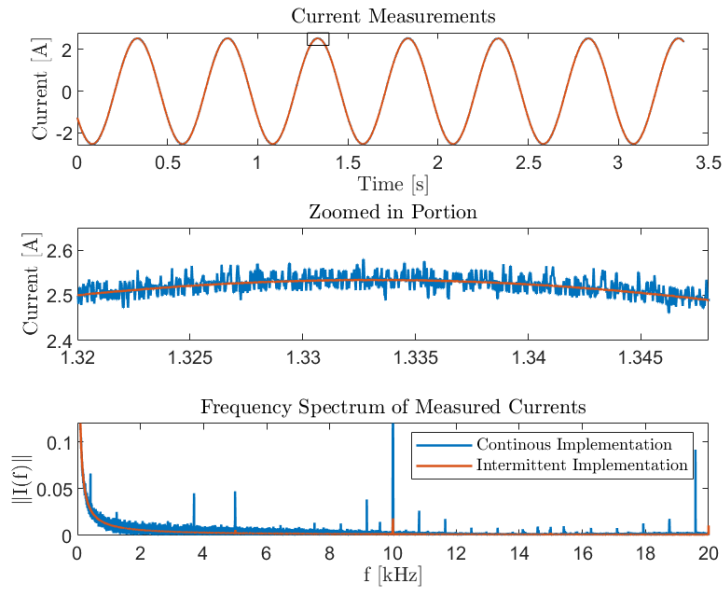
Figure 3.21: Current measurement comparison between continuous and intermittent implementations of the SINC^3 filter.
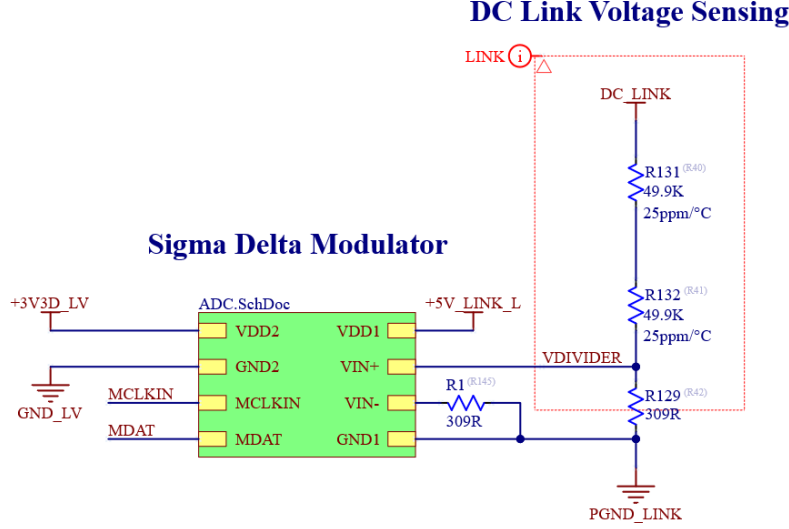
Figure 3.22: DC link voltage sensing schematic.

shows a sample voltage measurement during the precharge routine with a DC bus voltage of 30V.

Motion Sensing

Real-time sensing of the rotor's angular and radial position is achieved using linear Hall effect sensors and digital eddy current sensors respectively. Identical position sensing schemes are used in [52, 72]. The sensor arrangement from [52] is presented in Figure 3.24. Here h_i denotes a Hall effect sensor and c_i denotes a sensing coil used in conjunction with an inductance to digital converter to measure the radial position of the rotor. Although the presented schematic is for a different stator configuration, the same sensing principles still apply. Further details regarding the motion sensing scheme can be found in the referenced works.

Radial Position Sensing   The x-y radial position measurements of the rotor are acquired using a digital eddy current sensing scheme. This is realized using a programmable inductance to digital converter (LDC1101, Texas Instruments) in conjunction with a sensing coil (WR111180-36F5-B1, TDK).

The LDC chip regulates and maintains the oscillations of an LC oscillator
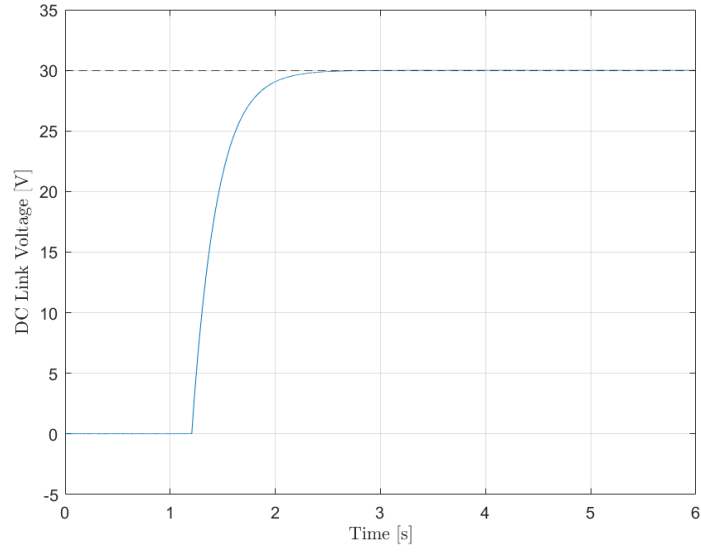
Figure 3.23: DC link voltage measurement during the precharge routine.
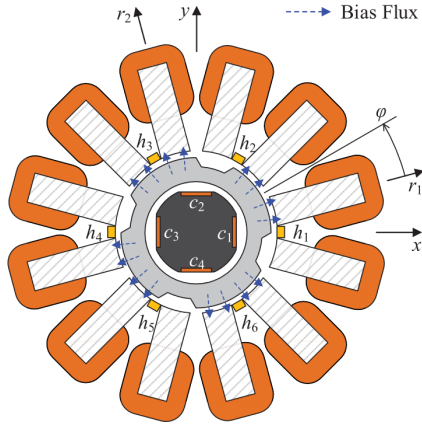
(a) Schematic [52]
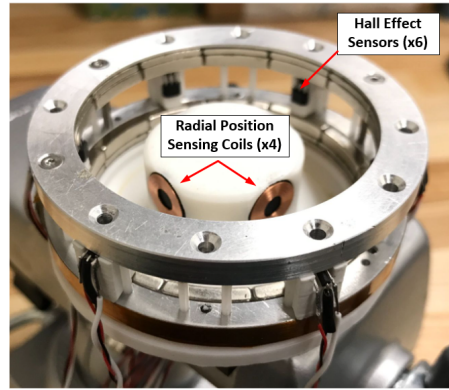
(b) Disassembled view

Figure 3.24: Sensor arrangement layout.

while measuring its resonant frequency by comparing it to an externally provided reference clock. The LC oscillator consists of the sensing coil in parallel with a chip capacitor whose value was selected in accordance with recommended guidelines in the LDC datasheet. As the rotor moves towards the sensing coil eddy currents are induced on the surface of the rotor. The eddy currents generate their own alternating magnetic field which opposes that of the sensing coil and thereby reduces its net inductance. The shift in inductance alters the resonant frequency of the LC oscillator as a function of the rotor's distance. The LDC converts this measured resonant frequency into a high-resolution digital word and communicates the information back to the controller via a 4-wire SPI protocol at a user-programmable sampling rate. The effective resolution of the frequency measurement is dependent on the chosen sampling rate. A higher sampling rate decreases the resolution of the frequency measurement and consequently the radial position measurement but allows for a higher achievable motion control bandwidth. A 5 kHz sampling rate is used throughout testing.

A total of 4 LDCs and sensing coils are used to measure the radial displacement of the rotor along orthogonal axes. The placement of the sensing coils is illustrated in Figure 3.24. Each LDC is assembled onto a dedicated PCB, shown in Figure 3.25, containing all the necessary passive components and connectors required for operation. The sensor PCB directly connects to the inverter board via a multipin connector which routes power and data lines to and from the board. It also features a breakout connector to interface with the sensing coils. The sensing coils are affixed to a 3D-printed mounting piece concentrically positioned to the stator structure using fasteners.

The SPI protocol is programmed in the FPGA. A single master single slave configuration is duplicated for all four LDCs for a simple and convenient implementation. The data from all four LDCs is processed on the FPGA to generate the x and y signals required for levitation control. Data from diametrically opposing sensing coils are subtracted from each other to improve the sensitivity and extend the linear range of the measurement. An offset is introduced to the x-y measurements to establish a zero reference position at the geometric center of the stator. The offsets are obtained by recording the averaged sensor measurements when the rotor is centered using a 3d printed plastic shim. A detailed characterization of this sensor response is presented in [55].
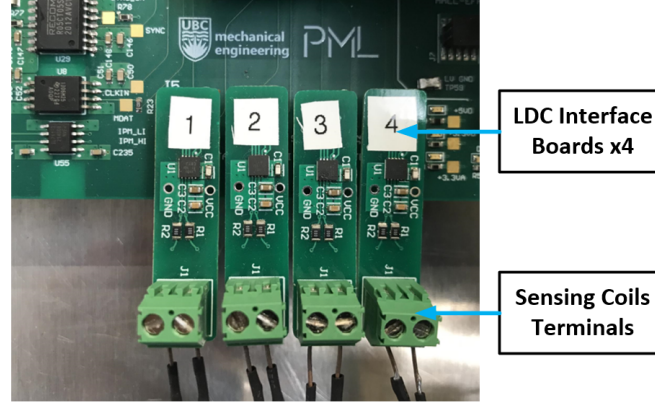
Figure 3.25: LDC sensor board.

Angular Position Sensing   The absence of a shaft in a bearingless slice motor rules out the possibility of using conventional mechanical shaft sensors such as encoders and resolvers for rotor angle detection. Instead, analog linear Hall effect sensors are used for this purpose.

The air gap flux field is modulated by the rotor teeth saliencies. The resulting air gap field can be thought of as the superposition of a homopolar and 8-pole field component rotating synchronously with the rotor. Using a Hall effect sensor we can detect this 8-pole component and subsequently extract the rotor angle information.

The angle information is estimated by processing signals from 6 Hall effect sensors (SS49E, Honeywell) distributed evenly along the perimeter of the stator. The sensors are glued onto a 3D-printed holder which wedges in between stator slots with the help of plastic alignment dowel pins. The arrangement of the Hall effect sensors on a disassembled permanent magnet array is presented in Figure 3.26. Each analog Hall effect sensor features three connections: Vcc (5V voltage rail), GND (ground), and Vout (analog output). The power and ground connections are sourced from the inverter board, whereas the sensor's analog output (Vout) is directly connected to the analog input of the controller where they are sampled at 10kHz.

The signals from diametrically opposing sensors are summed up to cancel out the effects of any two pole field components picked up by the sensors. This is done to desensitize the angle measurement to disturbances induced by the rotor radial displacements and the superimposed two-pole suspension
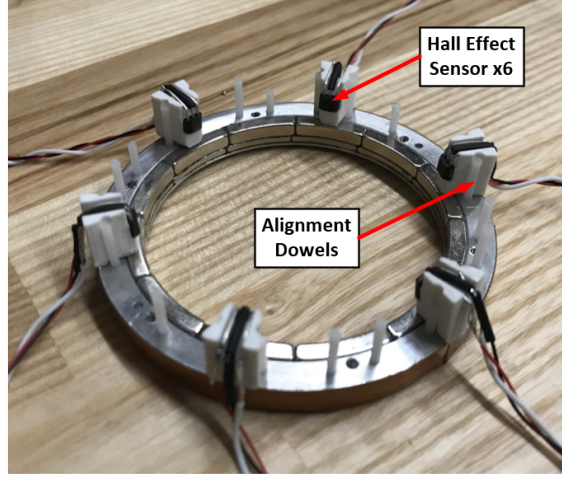
Figure 3.26: Hall effect sensor arrangement.

fields ensuring a more robust and reliable estimate. The resulting signals, assumed to be three-phase sinusoidal in nature, are then passed to a Clarke transformation matrix transforming the signals to an equivalent two-phase representation. The transformed signals vary in proportion to the sine and cosine of the electrical angle. These quadrature signals are fed to the same PLL structure discussed in Section 2.3.1 to estimate the rotor speed and angle. Previous works [53, 72] employed a numerical derivative method for rotor speed estimation. However, this approach encountered issues with aliasing and a non-linear, speed-dependent calibration. The adoption of the PLL method effectively resolves these challenges and enables closed-loop speed control even at high operational speeds.

3.2.5   PCB Design

Maintaining the integrity of high-speed digital lines is important to ensure repeatable and reliable performance of the motor drive. As such, careful consideration was given to ensure good signal and power integrity. The design and layout of the PCB were made in accordance with best practices and guidelines outlined in [6] and [57]. The layout of the PCB excluding the controller is repeated in Figure 3.27.

The PCB employs a 1.3 mm, 6-layer stack up with three signal layers, two ground planes, and a single power plane. Each of the signal layers is adjacent to a reference plane (either ground or power) to minimize loop inductance
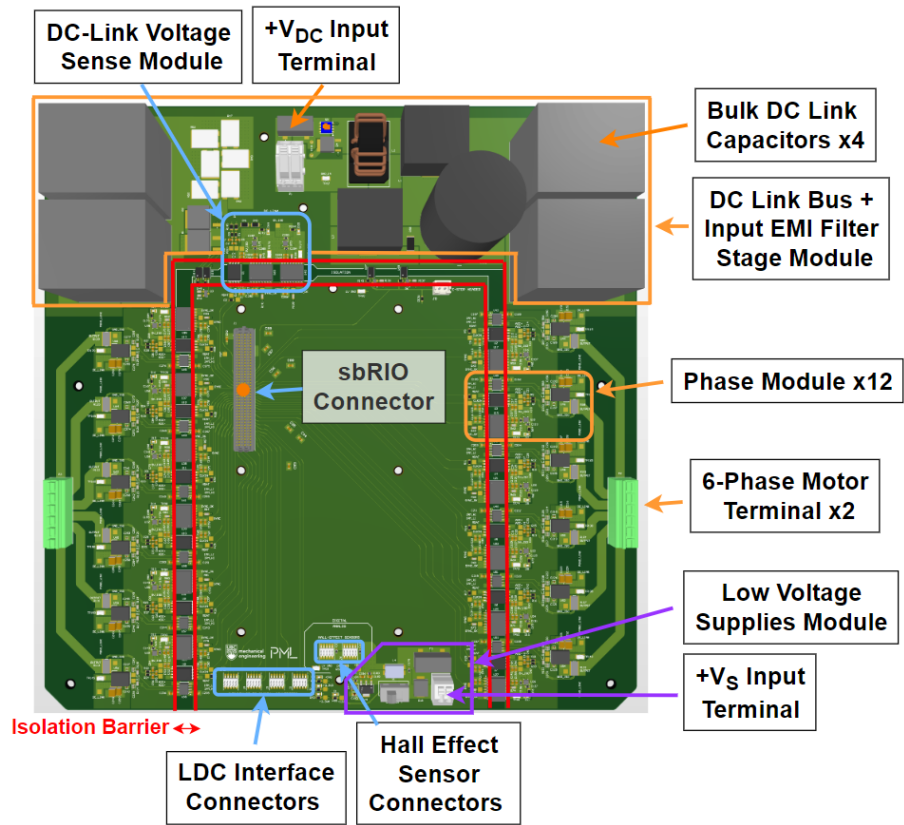
Figure 3.27: PCB layout.
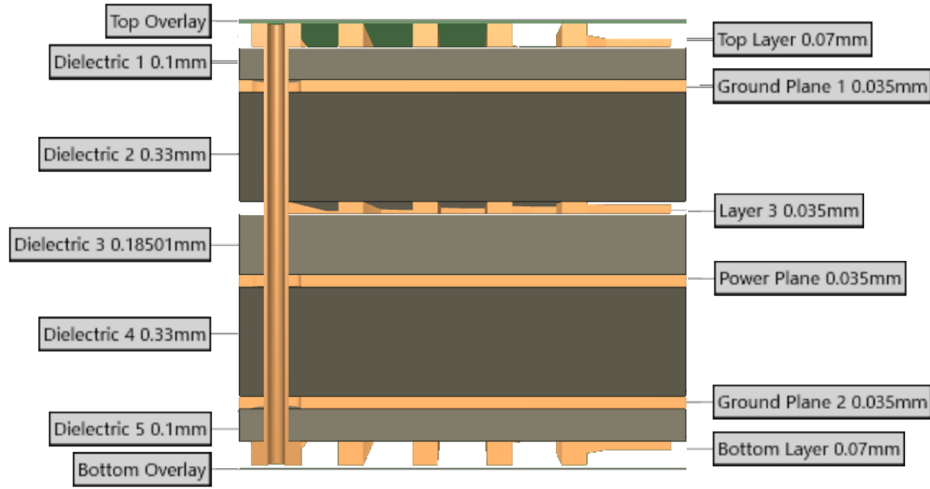
Figure 3.28: PCB stackup.

of the signal forward and return paths and eliminate broadside crosstalk between traces on different signal layers. An illustration of the stack up is presented in Figure 3.28.

Power Distribution Network

As opposed to signal layers that consist of conductive paths that primarily carry data, the plane layers consist of continuous copper regions providing stable reference potentials for the onboard components. The power plane plays an important role in establishing a low-impedance power distribution network for powering the components on the PCB while the ground planes provide a stable reference point for the components and signals on the board, acting as a return path for power and signal traces.

The isolation barrier marks where the individual ground and power planes were split in order to achieve galvanic isolation between the high- and low-voltage sides. The copper distribution within the separate ground and power planes is presented in Figure 3.29.

Power is supplied to the low-voltage side components via a large continuous copper pour connected to the 3.3V rails of the sbRIO. Similarly, on the high voltage side, the drains of the high side GaNFETs are connected to the DC link voltage rails via a separate copper pour on the power plane. The high voltage side additionally features a 5V rail referenced to DC link ground.

The gate driver circuits and the high voltage sides of the 2 channel digital isolators are powered through this rail via a wide copper trace located on the internal signal layer (layer 3).

The onboard components are effectively decoupled from the effects of parasitic inductances in the power distribution network by placing local decoupling capacitors adjacent to their power pins. The capacitors are connected to the internal planes using multiple vias and to the devices using short and wide traces. This is done to reduce the contributions of parasitic inductances from the vias and traces. Furthermore, the power plane is adjacent to a ground plane providing some interplane capacitance which aids in high-frequency power decoupling in addition to the local decoupling capacitors.

Three different grounds are employed on the high-voltage side. First, a signal ground (SGND) which acts as a ground reference for the gate driver circuits in the power stages. Second, a power ground (PGND) which acts as a ground reference for the DC link voltage and connects to the source terminal of the low side FETs. The SGND and PGND are left unconnected in the board to prevent switching noise in the PGND from shifting the ground potential of the SGND and possibly interfering with the gate driver operation. The two grounds are electrically connected within the half-bridge power stage chip. Third is a floating ground reference which is electrically shorted to the switch node of the half-bridge power stages. This floating reference is used by the isolated modulators for measuring the voltage across an inline shunt resistor, as discussed in Section 3.2.4. Copper underneath the switch node was emptied to minimize its overlap with the internal plane players. This is done to reduce parasitic capacitances on the switch node that contribute to losses as per recommendations in the power stage datasheet.

DC link voltages exceeding 30 V were not used during testing as a safety precaution against a switch node undervoltage concern. During the operation of the inverter, we observed negative spikes on the output switch node of the half-bridge power stage when it transitions from $+V_{dc}$ to 0 V. This occurs as the high side switch is opened forcing the current to commutate from the high side switch to the low side switch. These negative spikes exceed the minimum voltage rating (-5 V) specified in the product datasheet. The main contributor to this transient negative overshoot are the parasitics on the power commutation loop. We attempted to address this using the layout techniques outlined earlier. However, despite these attempts the issue was not resolved and requires further investigation.
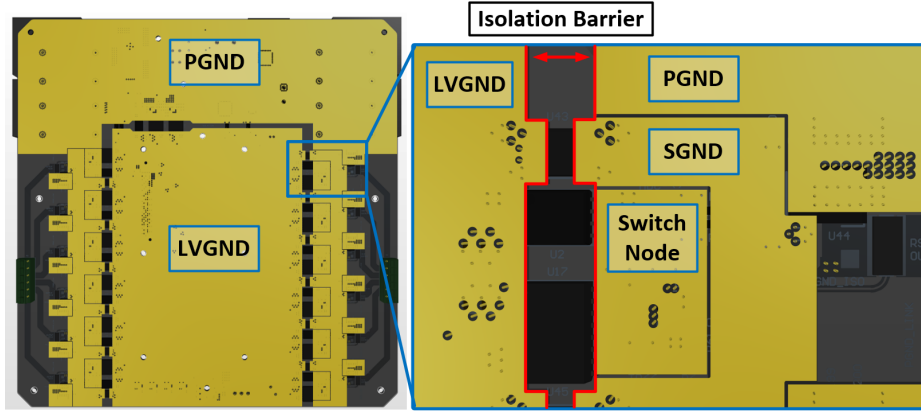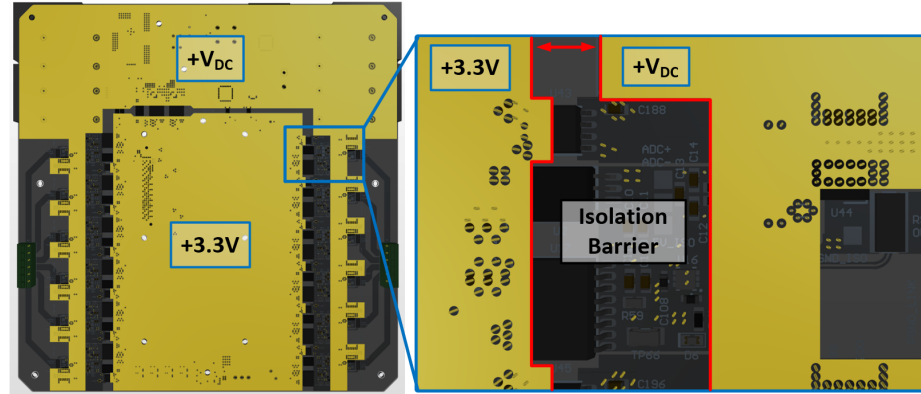
(a) Ground plane 1

(b) Power plane
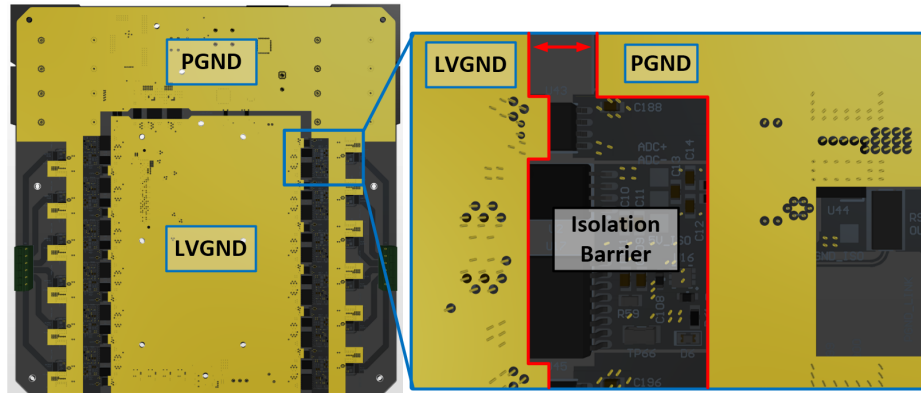
(c) Ground plane 2

Figure 3.29: Copper distribution on plane layers.

High-Speed PCB Routing Considerations

The low-voltage side includes an interface to the sbRIO controller board. Signals carrying high-frequency content, as characterized by fast edge rates ($\leq 1\,\text{ns}$) are routed to and from the controller board on the top and inner signal layers. The bottom layer is primarily used for routing power to the controller board and some components on the low-voltage side.

Signals routed on the top layer include the modulator clock and data signals, the DC/DC converter synchronizing clock signals, and the LDC clock signals. Signals routed on the inner signal layer include the complementary PWM signals for the power stages, the precharge and discharge circuit control signals, and the SPI data bus lines. A large uninterrupted copper pour is used for the ground plane on the low-voltage side of the board to provide a low-impedance return path for these high-speed signals. The copper distribution within the different signal layers is presented in Figure 3.30.

To ensure the integrity of these signals, they are routed using $55\,\Omega$ characteristic impedance traces as recommended in the sbRIO controller datasheet. The characteristic impedance of a trace is determined by several factors, including its width, thickness, and dielectric constant of the PCB material. By consulting with the PCB manufacturers the dimensions of the signal traces on different layers were determined to achieve the desired characteristic impedance values. Additionally, the traces are spaced apart as much as possible to minimize crosstalk between adjacent traces. Moreover, these signals are routed on a single layer to avoid impedance variations and discontinuities introduced by vias and to avoid switching reference planes which significantly increases the loop inductance. Stitching capacitors, connecting the power and ground planes, are placed in the vicinity of the controller connector providing a low-impedance return path for signals on inner layers. $20\,\Omega$ termination resistors are placed in series with the modulator output data lines. This is done to correct for impedance mismatches between the characteristic impedance of the transmission line $Z_c = 55\,\Omega$ and the output impedance of the driver $Z_o = 35\,\Omega$ to minimize signal reflections that may distort the signal. The output impedance of the modulator is obtained from the component IBIS model file.
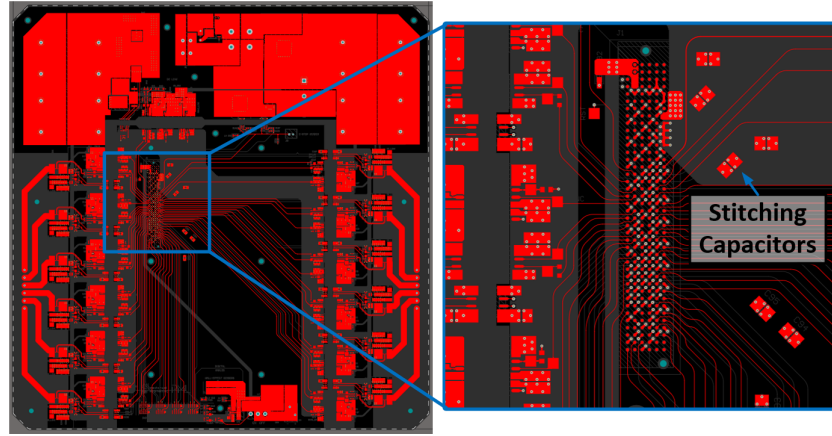
(a) Top layer
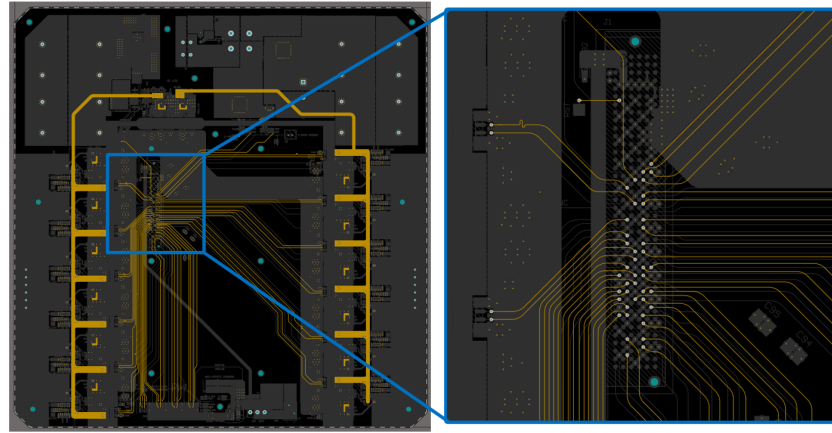
(b) Inner signal layer
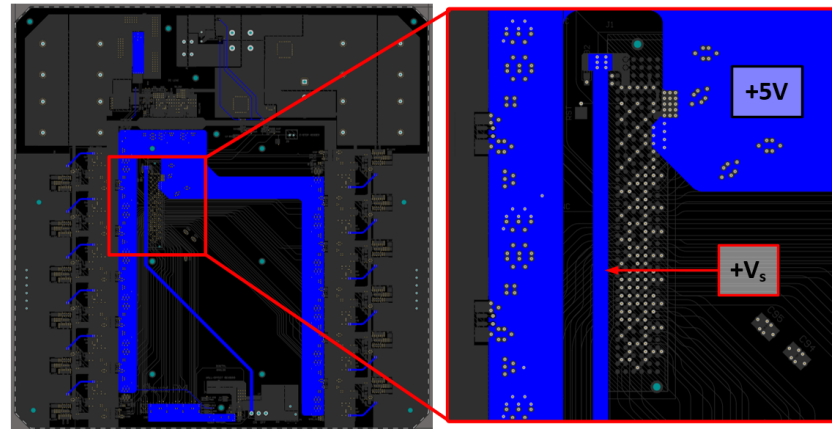
(c) Bottom layer

Figure 3.30: Copper distribution on signal layers.

Chapter 4

Implementation and Experimental Validation

This chapter highlights the successful validation of our design and its potential for future prototyping. Details of the control scheme and its implementation are covered followed by testing results. The experimental setup is presented in Figure 4.1. Not shown in the figure are the external power supplies powering the board. A 1200W TDK power supply provides DC link voltage and another power supply powers the low voltage side using 15V.

4.1   Control Scheme

The overall system control structure is presented in figure 4.2. The system consists of a nested control structure with an inner current regulation loop and outer motion control loops. The outer motion control loops receive measurement signals of the rotor's radial position and angular velocity and generate reference current commands to actively control the rotation and levitation of the rotor. The inner current regulation loops are used to realize the requested current references by receiving current measurement feedback and generating voltage reference commands which are transformed and sent to a triangle carrier-based PWM generation block.

Such a cascaded control scheme allows us to separately design and tune the inner and outer control loops provided that their bandwidths are sufficiently far apart. A general rule of thumb is to select the bandwidth of the inner loop to be at least five times higher than the bandwidth of the outer loop [2]. This ensures that the dynamics of the inner current regulation loop are sufficiently decoupled from the slower dynamics of the outer motion control loop.

A synchronous notch filter is used in the feedback path of the radial position control loop to selectively attenuate mass unbalance-induced bearing
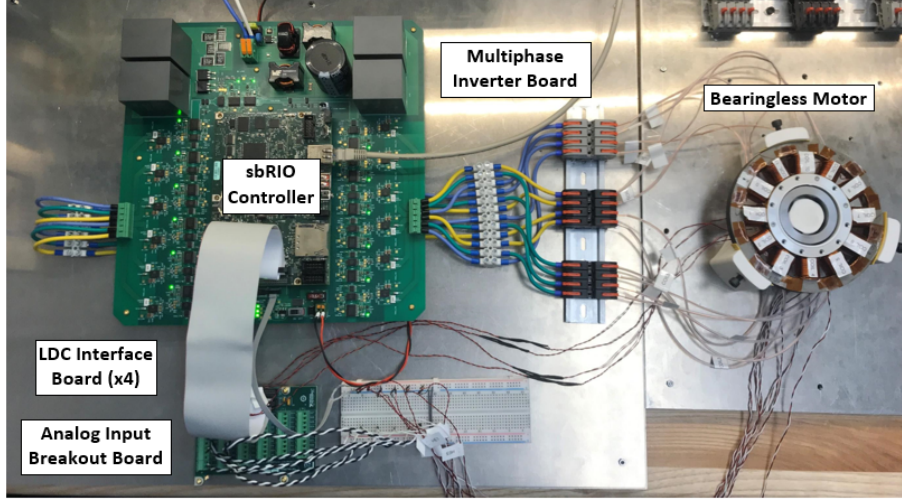
Figure 4.1: Testing setup.

forces allowing for smoother operation and reduced actuator control effort. Additionally, in order to overcome limitations encountered when using the Hall effect sensors, the observer-based sensorless control schemes covered in Chapter 2 are used to estimate the rotor's angular displacement and velocity from the input voltage references and the measured currents. The estimated signals are used in the speed control and the rotational coordinate transformations. A dynamic current and voltage allocation procedure is used to saturate the motion and current controller reference commands in a way that prioritizes the stable operation of the safety-critical rotor suspension. Key motor specifications used in developing and tuning the different control strategies are summarized in table 4.1.

Table 4.1: Relevant motor specifications.

Symbol	Quantity	Value
R_s	Phase winding resistance	0.43 Ω
L_{α_1}	Suspension winding α-axis inductance	1.2 mH
L_{β_1}	Suspension winding β-axis inductance	1.2 mH
L_{d_4}	Rotation winding d-axis inductance	2.3 mH
L_{q_4}	Rotation winding q-axis inductance	2.3 mH
m	Rotor mass	0.12 kg
J	Rotor inertia	4.8e-5 kg m^2
K_x	x-axis radial negative stiffness	-15.2 kN/m
K_y	y-axis radial negative stiffness	-15.2 kN/m
K_{ix}	x-axis suspension force constant	2.88 N/A
K_{iy}	y-axis suspension force constant	2.88 N/A
K_e	Motor back EMF constant	7.175 mWb
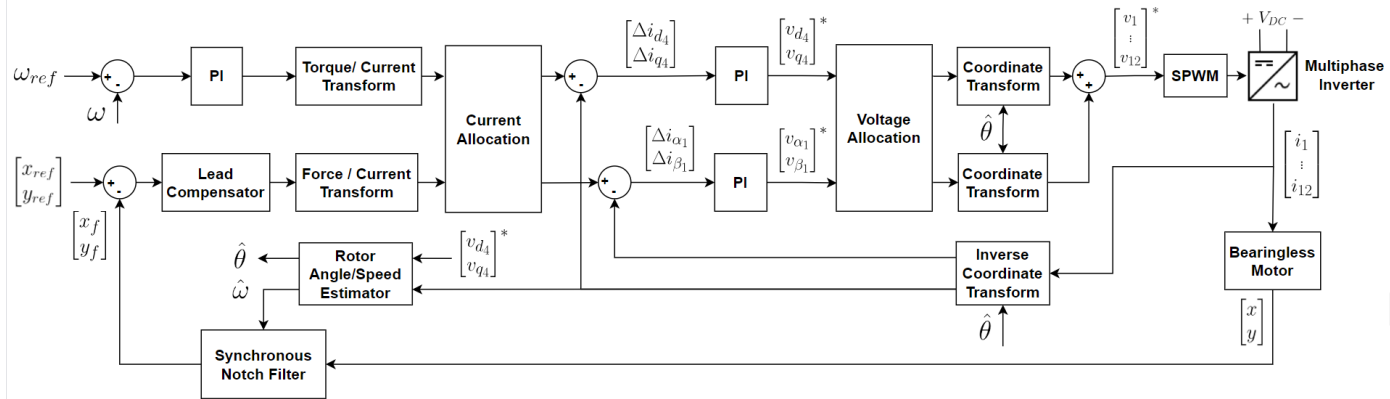
Figure 4.2: Control scheme.

4.1.1 Current Control

To achieve independent control of rotation and suspension the decoupling procedure outlined in chapter 2 is employed. This involves the use of a generalized Clarke transformation to conceptually decompose the multiphase currents i_{1-12} into a pair of independent two-dimensional space vectors in decoupled subspaces $\alpha_1\beta_1$, and $\alpha_4\beta_4$. Generation of the 8 and 2-pole field components is achieved by regulating the current vector components in the $\alpha_4\beta_4$ and $\alpha_1\beta_1$ subspaces, respectively. Additionally, to eliminate steady-state errors in the rotational current regulation, a rotational transformation is used to transform the rotating space vector in the stationary $\alpha_4\beta_4$ frame to an equivalent stationary vector expressed in the rotating d_4q_4 frame. The current transformations are carried out as follows

$$\begin{bmatrix} i_{\alpha_1} & i_{\beta_1} & i_{d_4} & i_{q_4} \end{bmatrix}^T = [T_r]\ [T_c]\ i_{1-12}$$

where T_c and T_r are matrices of dimension 4×12 and 4×4 as follows

$$T_c = \frac{2}{12} \begin{bmatrix} 1 & \cos\phi & \cos 2\phi & \dots & \cos 2\phi & \cos\phi \\ 0 & \sin\phi & \sin 2\phi & \dots & -\sin 2\phi & -\sin\phi \\ 1 & \cos 4\phi & \cos 8\phi & \dots & \cos 8\phi & \cos 4\phi \\ 0 & \sin 4\phi & \sin 8\phi & \dots & -\sin 8\phi & -\sin 4\phi \end{bmatrix}$$

$$T_r = \begin{bmatrix} 1 & 0 & 0 & 0 \\ 0 & 1 & 0 & 0 \\ 0 & 0 & \cos 4\theta_m & \sin 4\theta_m \\ 0 & 0 & -\sin 4\theta_m & \cos 4\theta_m \end{bmatrix}$$

The matrix T_c, where $\phi = {}^{2\pi}/_{12}$, represents the generalized Clarke transformation responsible for the decoupling of the multiphase variables into different subspaces. Matrix T_r represents the rotational transformation matrix.

A pair of two-axis PI controllers are used to regulate the 2 and 8-pole flux-inducing current components. Tuning of the controller gains is done in accordance with the pole-zero cancellation method. Using this method we are able to effectively simplify the dynamics of the current control loop to that of a first-order system with a single parameter (bandwidth) to tune.

We first examine this tuning procedure for the suspension current control loop by expressing the corresponding open loop transfer function as

$$G_o(s) = C_\alpha(s)\,P(s) = K_{p\alpha}(1 + \frac{K_{i\alpha}}{s})\,\frac{1}{sL_\alpha + R_s} = \frac{K_{p\alpha}}{sL_\alpha}\left(\frac{s + K_{i\alpha}}{s + R_s/L_\alpha}\right)$$

Here we restrict our analysis to a single axis since the dynamics of both axes are decoupled and similar. The integral gains K_i are chosen to cancel out the effects of the plant pole while the proportional gain K_p are tuned to achieve the desired current control bandwidth ω_{bw} as

$$K_{i\alpha} = R_s/L_\alpha \qquad K_{i\beta} = R_s/L_\beta$$
$$K_{p\alpha} = 2\pi f_{bw}L_\alpha = \omega_{bw}L_\alpha \qquad K_{p\beta} = 2\pi f_{bw}L_\beta = \omega_{bw}L_\beta$$

Utilizing these gains we can express the closed-loop transfer function as that of a first-order system given by

$$G_{cl}(s) = \frac{i_{\alpha\beta}(s)}{i^*_{\alpha\beta}(s)} = \frac{G_o(s)}{1 + G_o(s)} = \frac{\omega_{bw}}{s + \omega_{bw}}$$

This pole-zero cancellation scheme works well for regulating currents expressed in a stationary reference frame. However, it is not as effective when regulating currents in a rotating frame where the plant dynamics vary with rotation speed. This limitation is made evident when expressing the rotation winding voltage equations using complex vector notation.

In complex vector notation, a two-dimensional vector is represented as a complex quantity with real and imaginary parts, such as $f_{dq} = f_d + jf_q$. This notation allows us to simplify a multiple-input multiple-output (MIMO) system into a single-input single-output (SISO) system that can be easily analyzed using classical control techniques. Rewriting the rotation winding voltage equations using complex vector notation yields

$$v_{dq} = R_s i_{dq} + L\frac{di_{dq}}{dt} + j\omega_e L i_{dq}$$

taking the Laplace transform we obtain the admittance transfer function as

$$\frac{i_{dq}(s)}{v_{dq}(s)} = \frac{1}{sL + j\omega_e L + R_s}$$

Note that the disturbance back emf term $\omega\lambda_{pm}$ is omitted from the voltage equation for simplicity and the dq axes inductances are assumed to be equal ($L_d = L_q = L$) as is the case with the reference motor. From this, we observe that the plant pole varies as a function of rotation frequency, specifically as $j\omega_e + R_s/L$ due to the cross-coupled speed-induced voltage terms. Failing to compensate for this effect will lead to a degradation in the control loop performance at high speeds. To overcome this limitation, [10] proposes the complex vector regulator structure. This approach modifies the conventional (PI) controller structure by introducing a compensation term that adjusts the controller zero accordingly in response to the changing speed. This ensures pole-zero cancellation in theory, regardless of the rotor speed. The resulting block diagram of the complex vector regulator is depicted in Figure 4.3. Similar to the suspension current controller the gains of the rotation current controller are tuned as

$$K_{id} = R_s/L_d \qquad K_{iq} = R_s/L_q$$
$$K_{pd} = 2\pi f_{bw} L_d = \omega_{bw} L_d \qquad K_{pq} = 2\pi f_{bw} L_q = \omega_{bw} L_q$$

The final transfer function matrix of the suspension and rotation current regulators is as follows.

$$\begin{bmatrix} v^*_{\alpha_1\beta_1} \\ v^*_{d_4q_4} \end{bmatrix} = \begin{bmatrix} C_{\alpha_1\beta_1}(s) & 0 \\ 0 & C_{d_4q_4}(s) \end{bmatrix} \begin{bmatrix} \Delta i_{\alpha_1\beta_1} \\ \Delta i_{d_4q_4} \end{bmatrix}$$

where the suspension current controller matrix $C_{\alpha_1\beta_1}(s)$ consists of the PI regulators in series with a first-order low-pass filter

$$C_{\alpha_1\beta_1}(s) = \begin{bmatrix} K_{p\alpha}\left(1 + K_{i\alpha}/s\right) & 0 \\ 0 & K_{p\beta}\left(1 + K_{i\beta}/s\right) \end{bmatrix} \frac{\omega_c}{s + \omega_c}$$

A low pass filter with a cutoff frequency ω_c is used to enhance the noise rejection capabilities of the controller. The cutoff frequency ω_c is set as
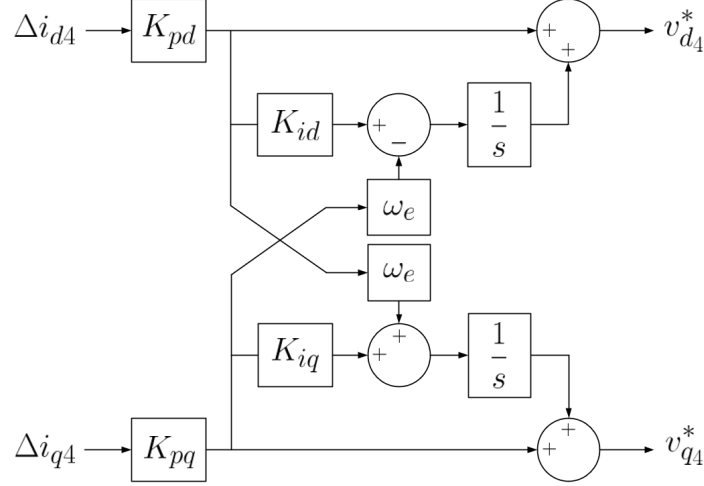
Figure 4.3: Complex vector regulator block diagram.

3.5 times the suspension current control bandwidth ($3.5 \times \omega_{bw}$) throughout testing. The rotation current controller matrix is given as

$$
C_{d_4q_4}(s) = \begin{bmatrix} K_{pd}\left(1 + K_{id}/s\right) & -K_{pq}\omega_e/s \\ K_{pd}\omega_e/s & K_{pq}\left(1 + K_{iq}/s\right) \end{bmatrix}
$$

The PI controllers are discretized via the Tustin method at twice the PWM switching frequency for implementation in the FPGA. Additionally, integrator anti-windup is realized using a clamping method. The integral action is halted if both of the following conditions are met 1) The controller output is saturated and 2) the sign of the controller output matches that of the error, i.e., the error causes the control signal to become even more saturated [2]. The second condition allows the integral action to resume if the controller is trying to get out of saturation making the unwinding process quicker than it would otherwise be.

The inverse generalized Clarke and rotation transformations are used to obtain multiphase pole voltage reference signals $[v_1^* \dots v_{12}^*]$ expressed in the stator fixed frame. The reference commands are compared with a high-frequency triangular carrier wave, whose frequency equals the PWM switching frequency, to determine the switching states for the power switches in each inverter leg. A center-aligned PWM scheme with a triangular carrier wave is used despite having a slightly more complicated timer implemen-

tation and half the PWM resolution of the alternative edge-aligned PWM scheme with a sawtooth carrier wave. The center-aligned scheme was favored primarily for its compatibility with the synchronized sampling technique for phase current measurement. Additionally, the symmetric nature of the output signal allows for lower harmonic distortions.

4.1.2 Radial Position Control

Slice motors are characterized by a small rotor axial length-to-diameter ratio. Initially proposed in [65], these motors use reluctance forces to passively stabilize axial and tilting motions, leaving only the inherently unstable radial degrees of freedom (DOFs) requiring active control.

To stabilize the radial motions, lead compensators are employed. In addition to compensating for the destabilizing negative stiffness, this controller is designed to provide sufficient damping and disturbance rejection capabilities. Two identical decoupled SISO controllers are used for regulating the x and y-axis motions. The transfer functions of the discrete-time lead controllers are given as

$$C(s) = K_{xy}\frac{1+Ts}{1+\alpha Ts} \xrightarrow{Tustin} C(z) = K_{xy_d}\frac{z+b}{z+a}$$

Controller parameters were tuned using a model-based loop-shaping technique. Using the linearized plant model we design a lead compensator in the continuous time domain to shape the suspension loop transfer function to achieve an approximate gain crossover frequency of 60 Hz and a corresponding phase margin of 50°. The controller is discretized via the tustin method at a sampling rate equal to the programmed output data rate of the radial position sensors (5 kHz). The controller outputs a set of reference current commands $[i^*_{\alpha_1} \ i^*_{\beta_1}]^T$ in response to the rotor's radial position tracking error.

4.1.3 Rotation Control

Two different operation modes were tested for rotation control: Closed loop speed control and open-loop torque control.

Closed loop speed control is achieved using a discrete-time PI controller running at a 1kHz loop rate. The controller gains were initially designed using a model-based loop-shaping strategy and further refined using a trial-and-error approach to improve the time domain specifications.

The output torque reference of the speed controller is converted into a two-dimensional current reference vector $[i_{d4}^* \; i_{q4}^*]^T$ using the MTPA control strategy. For nonsalient motors such as our motor, this is simply realized by setting the d_4-axis current reference at zero and computing the q_4-axis current using the following torque equation

$$T_e = \frac{np}{2} \left(K_e i_{q4} \right)$$

where λ_f is the permanent magnet flux linkage, $n = 12$ is the numder of phases, and $p = 4$ is the number of rotor pole pairs.

It was observed that at high speeds the dynamic performance of the closed-loop speed regulator was significantly impacted due to an insufficient voltage margin for current regulation. Operation and testing at these high speeds is done using open-loop torque control. In this control mode, the speed controller is bypassed and open loop current references $[i_{d4}^* \; i_{q4}^*]^T$ are directly fed to the rotation current control loop.

4.1.4 Current and Voltage Allocation

Contrary to bearingless motors with separated winding schemes, motors with combined winding schemes are characterized with the ability to utilize the entire winding slot space for both torque and radial force production. However, to fully realize this capability, a proper current and voltage saturation procedure is required to allocate the limited available resources (i.e. DC link voltage and winding current) between the rotation and suspension subsystems. To the best of our knowledge, studies on combined winding machines so far do not detail this allocation procedure and thus we aim to address this here.

In our implementation, we propose a variable/dynamic allocation procedure that prioritizes the allocation of resources to the safety-critical suspension and assigns the remaining to the rotation in real-time. This dynamic approach allows us to fully utilize the available resources without compromising the stability of the levitation. In contrast, the approach taken in [72] relies on a static allocation of resources predefined beforehand. With this conservative approach, the available resources will only be fully utilized if both the rotation and suspension systems simultaneously require all their allocated resources. As a result, the motor's dynamic performance may be suboptimal. By implementing the variable allocation procedure, we aim to achieve

superior dynamic performance, making the most use of available resources and enhancing the overall capabilities of the bearingless motor system.

To ensure the motor operates reliably within safe operating limits we first establish the maximum allowable current and voltage constraints, representing the available resources for torque and radial force production.

Current Allocation

Current constraints arise from the motor winding construction. Excessive current flowing through the motor windings generates heat which may exceed the thermal limits of the winding insulation and lead to permanent damage. For a wire gauge of 22 AWG and an allowable current density of $10 \ \mathrm{A/mm^2}$ the maximum phase current limit for continuous operation is evaluated as

$$ i_{max} = 10\frac{\mathrm{A_{RMS}}}{\mathrm{mm^2}} \cdot 0.33\mathrm{mm^2} \cdot \sqrt{2} = 4.7\mathrm{A_{pk}} $$

This translates into a constraint on the sum of the magnitudes of the suspension and rotation current reference vectors expressed as

$$ \sqrt{i_{\alpha_1}^{*}{}^2 + i_{\beta_1}^{*}{}^2} + \sqrt{i_{\alpha_4}^{*}{}^2 + i_{\beta_4}^{*}{}^2} < i_{max} $$

Having established this constraint, the next step is to determine how much of this maximum allowable winding current is assigned to rotation and suspension.

Instead of statically allocating a portion of the total winding current to suspension and rotation, as was done in [72], we propose a dynamic allocation that prioritizes the suspension and assigns the remaining current margin to rotation in real-time. The suspension takes precedence in obtaining the required current for stable levitation. Once the suspension needs are fulfilled, any remaining current is allocated to the rotation. This dynamic allocation approach ensures the safety-critical suspension operates reliably while utilizing the available resources efficiently. The allocation procedure is illustrated in Figure 4.4. The procedure is explained in the following steps

- The suspension controller requests some current reference vector $[i_{\alpha_1}^{*} \ \ i_{\beta_1}^{*}]^T$ based on the radial position tracking error
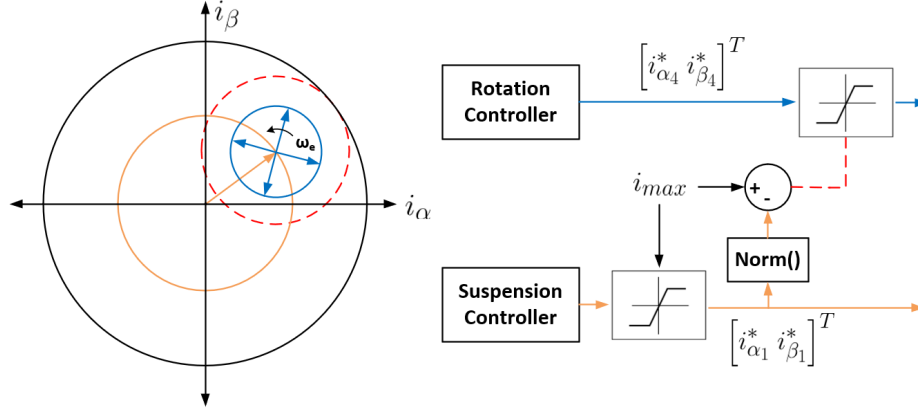
Figure 4.4: Reference current allocation procedure. The solid black circle/line represents the maximum allowable winding current i_{max}. The solid orange and blue circles/lines represent the magnitude of the requested rotation and suspension current vectors respectively. The dashed red circle/line represents the remaining current margin that can be used for rotation.

- The requested current vector passes through a vector saturation block that bounds the vector's magnitude to $\pm i_{max}$. The saturation is carried out as follows to preserve the orientation of the vector

$$
i_{\alpha\beta}^* = \begin{cases} i_{\alpha\beta}^* & \text{if } \sqrt{i_\alpha^{*\,2} + i_\beta^{*\,2}} \leq i_{max} \\ i_{\alpha\beta}^* \frac{i_{max}}{\sqrt{i_\alpha^{*\,2} + i_\beta^{*\,2}}} & \text{if } \sqrt{i_\alpha^{*\,2} + i_\beta^{*\,2}} > i_{max} \end{cases}
$$

- The magnitude of the bounded suspension current vector is subtracted from the maximum allowable current i_{max} to obtain the remaining current margin that can be used by the rotation system

- The remaining current margin is used to bound the requested rotation current reference vector $[i_{\alpha_4} \ i_{\beta_4}]^T$ using the same vector saturation procedure

Voltage Allocation

Voltage constraints in an inverter-driven load are determined by the available DC link voltage V_{dc} and the chosen PWM scheme. The pole voltage reference v_n^* used to produce the switching states of inverter leg n is expressed as

the sum of the contributions from the rotation and suspension pole voltage components as

$$v_n^* = v_{n_r}^* + v_{n_s}^*$$

The suspension $v_{n_s}^*$ and rotation pole voltage $v_{n_r}^*$ components are obtained by performing the inverse generalized Clarke transformation on the rotation and suspension voltage reference vectors respectively as

$$[v_1^* \dots v_{12}^*]_s^T = \begin{bmatrix} 1 & \cos\phi & \cos 2\phi & \dots & \cos 2\phi & \cos\phi \\ 0 & \sin\phi & \sin 2\phi & \dots & -\sin 2\phi & -\sin\phi \end{bmatrix}^T \cdot \begin{bmatrix} v_{\alpha_1}^* \\ v_{\beta_1}^* \end{bmatrix}$$

$$[v_1^* \dots v_{12}^*]_r^T = \begin{bmatrix} 1 & \cos 4\phi & \cos 8\phi & \dots & \cos 8\phi & \cos 4\phi \\ 0 & \sin 4\phi & \sin 8\phi & \dots & -\sin 8\phi & -\sin 4\phi \end{bmatrix}^T \cdot \begin{bmatrix} v_{\alpha_4}^* \\ v_{\beta_4}^* \end{bmatrix}$$

Following the transformations, the pole voltage components are of the following form

$$v_{n_s}^* = \left(\sqrt{v_{\alpha_1}^{*\,2} + v_{\beta_1}^{*\,2}} \right) \cos\left(\phi_s\right) = m_s \cdot \frac{V_{dc}}{2} \cos\left(\phi_s\right)$$

$$v_{n_r}^* = \left(\sqrt{v_{\alpha_4}^{*\,2} + v_{\beta_4}^{*\,2}} \right) \cos\left(\omega_e t + \phi_r\right) = m_r \cdot \frac{V_{dc}}{2} \cos\left(\omega_e t + \phi_r\right)$$

where m_s and m_r are the suspension and rotation modulation indices respectively, ω_e is the electrical frequency, and ϕ_s and ϕ_r are the phases of the suspension and rotation pole voltage references. Using a triangle comparison PWM scheme the reference pole voltage signals v_n^* should not exceed $v_{max} = V_{dc}/2$ to stay within the linear modulation range where the relationship between the reference pole voltage and the output phase voltage or line to neutral voltage is linear. Operation beyond that range is known as over-modulation and entails a loss of linearity and increased harmonic distortion of the phase output voltages. Moreover, it negatively impacts suspension performance by distorting the requested suspension voltage vector, possibly leading to instabilities.
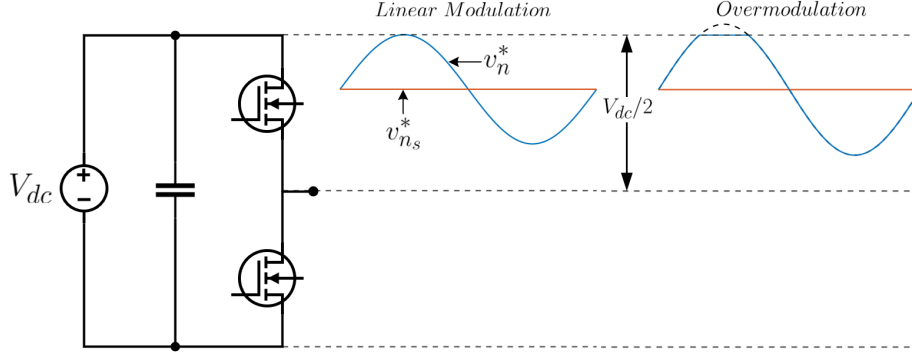
Figure 4.5: Illustration of overmodulation.

We further impose a constraint on the maximum duty cycle to allow proper operation of the bootstrap circuit. The bootstrap circuit has inherent limitations concerning the maximum duty cycle it can effectively support. When the high-side FET remains continuously closed for an extended period, such as in the case of a 100% duty cycle, the bootstrap capacitor discharges without the opportunity to recharge, leading to a loss of gate drive voltage and triggering the undervoltage lockout (UVLO) feature of the LMG5200. To overcome this we avoid operation in the overmodulation region $(v_n^* > V_{dc}/2)$ where the duty cycle is held at 100% when the pole voltage references are clipped as shown in Figure 4.5.

Assuming worst-case conditions where $\phi_s = 0$, operation in the linear modulation region translates into a constraint on the sum of the modulation indices as $0 \leq m_s + m_r \leq 1$. This can be equivalently expressed using the magnitudes of the suspension and rotation voltage reference vectors as

$$\sqrt{{v_{\alpha_1}^*}^2 + {v_{\beta_1}^*}^2} + \sqrt{{v_{\alpha_4}^*}^2 + {v_{\beta_4}^*}^2} < V_{dc}/2$$

Similar to the current allocation procedure, the voltage required for regulating the suspension currents is given precedence. Once the suspension needs are fulfilled, any remaining voltage margin is allocated for regulating the rotation currents. This voltage allocation procedure ensures there is always some voltage margin to regulate the suspension currents and avoid rotor touchdown at the expense of torque generation. The voltage allocation procedure is illustrated in Figure 4.6. The procedure is explained in the following steps
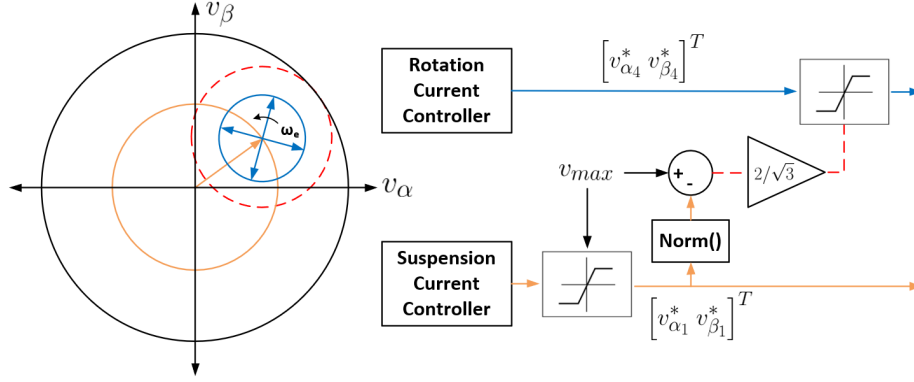
Figure 4.6: Reference voltage allocation procedure.

- The suspension current controller requests some voltage reference vector $[v_{\alpha_1}^* \; v_{\beta_1}^*]^T$ based on the suspension current tracking error.

- The requested voltage vector passes through a vector saturation block that bounds the vector's magnitude to $\pm V_{dc}/2$.

- The magnitude of the bounded suspension voltage vector is subtracted from the maximum allowable pole voltage $v_{max} = V_{dc}/2$ to obtain the remaining voltage margin that can be used by the rotation system.

- The utilization of the remaining voltage margin is improved by a factor of $2/\sqrt{3}$ by supplementing the sinusoidal rotation pole voltage references with a zero sequence voltage component as

$$v_{n_r}^* = v_{ph} + ZSV = MI_r \cdot \frac{V_{dc}}{2} \cos\left(\omega_e t + \phi_r\right) + ZSV$$

By injecting a zero sequence voltage ZSV, the fundamental component of the rotation phase voltage v_{ph} can be increased without violating the $v_n^* \leq V_{dc}/2$ constraint. This injected voltage is common across all phases and has no effect on the phase and line-to-line voltages for a load with a floating neutral point. Using a min/max zero sequence injection technique [30] the linear modulation range of the rotation component is extended by a maximum factor of $2/\sqrt{3}$. This allows us to increase the utilization of the available DC bus voltage, allowing for higher output phase voltage levels. An illustration of the zero sequence injection technique is presented in Figure 4.7. The zero sequence voltage is
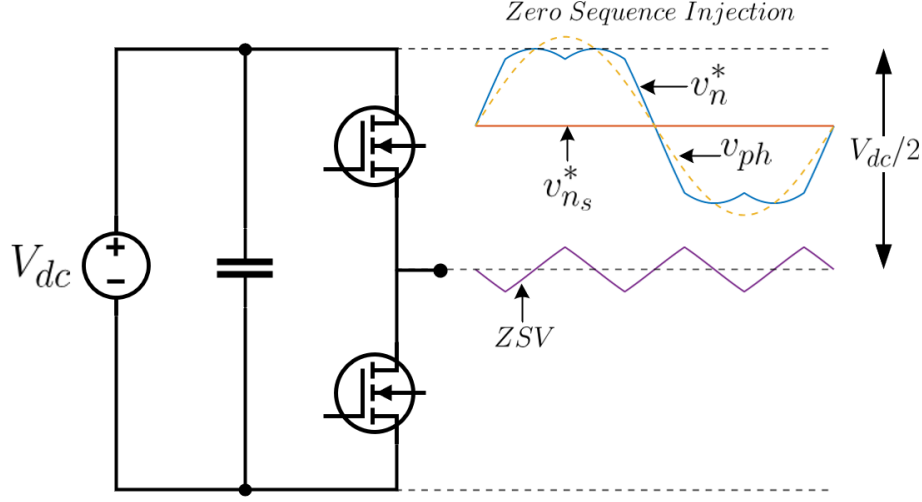
Figure 4.7: Zero sequence voltage injection.

computed from the unmodified rotation pole voltage references $[v^*_{1-12}]_r$ as

$$ZSV = -0.5 \left(\mathbf{max} \left([v^*_{1-12}]_r \right) + \mathbf{min} \left([v^*_{1-12}]_r \right) \right)$$

This is a general zero sequence injection procedure for a 12-phase winding with a single neutral point. The maximum improvement in DC bus utilization is achieved for a three-phase system. As the number of phases increases the improvement in the DC bus utilization by zero-sequence injection decreases. In our implementation, we use 4 sets of three-phase windings with 4 different isolated neutral points. As such we can benefit from the maximum possible improvement in DC bus utilization by separately computing the zero sequence voltage for each winding set k, where $k \in [1, 2, 3, 4]$, as follows

$$ZSV = -0.5 \left(\mathbf{max} \left([v^*_k, \ v^*_{4+k}, \ v^*_{8+k}]_r \right) + \mathbf{min} \left([v^*_k, \ v^*_{4+k}, \ v^*_{8+k}]_r \right) \right)$$

- The resulting voltage margin is used to bound the requested rotation voltage reference vector $[v_{\alpha_4} \ v_{\beta_4}]^T$ using the same vector saturation procedure

4.1.5 Sensorless Control

We encountered a number of limitations arising from the Hall effect sensor, such as a susceptibility to switching noise, high quantization error at elevated speeds due to a limited sampling rate, and a cross-coupling to armature-induced air gap flux components, which leads to an erroneous angle estimate. Additionally, simplifying assumptions made in processing the sensor signals leads to noticeable distortions in the Hall-based angle estimate. These challenges have motivated us to use angle sensorless control techniques to replace the function of the Hall effect sensor.

A few of these issues are demonstrated in Figures 4.8 and 4.9. Figure 4.8 highlights the stair-case-like distortions in the Hall-based angle measurement while the rotor is levitating and rotating at a speed of 1 kRPM. The measurement was sampled at 10 kHz. These distortions arise from simplifications made in processing the Hall effect sensor signals and may lead to uneven torque production and increased torque ripple.

In an ideal scenario, the Hall effect sensor would only measure the radial component of the rotor flux. However, due to the armature reaction, the air gap field is significantly affected by the stator winding current flow, leading to an erroneous angle measurement. This effect is presented in the first plot of Figure 4.9. Here, the rotor is centered and constrained at the $0°$ position using a 3D-printed plastic shim while a rotation current reference vector $[i^*_{d_4} \ i^*_{q_4}]^T$ of magnitude 0.5 A is injected into the windings. The phase of the reference vector is swept from 0 to $360°$ in increments of $30°$. Angle errors of up to $12°$ can be seen for a $90°$ phase vector. Such errors can deteriorate the performance of the field-oriented control strategy, leading to suboptimal torque production.

Moreover, imperfections in the physical placement and alignment of the sensors, along with mismatches between the stator geometric and magnetic centers due to fabrication and assembly imperfections, diminish the effectiveness of the two-pole field compensation strategy discussed in section 3.2.4. These issues introduce additional errors to the angle measurement, as shown in the second plot of Figure 4.9. In this case, a similar angle sweep was conducted for a suspension current reference vector $[i^*_{\alpha_1}; i^*_{\beta_1}]^T$ of magnitude 0.5 A. Slight errors of up to $0.5°$ can be seen in the measurement. Despite being small, these errors are further exacerbated by rotor eccentricities that result in an uneven change in the airgap flux distribution sensed by the diametrically opposing sensors.
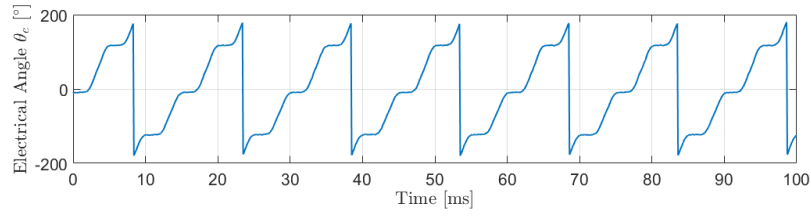
Figure 4.8: Hall-based angle estimate distortion.
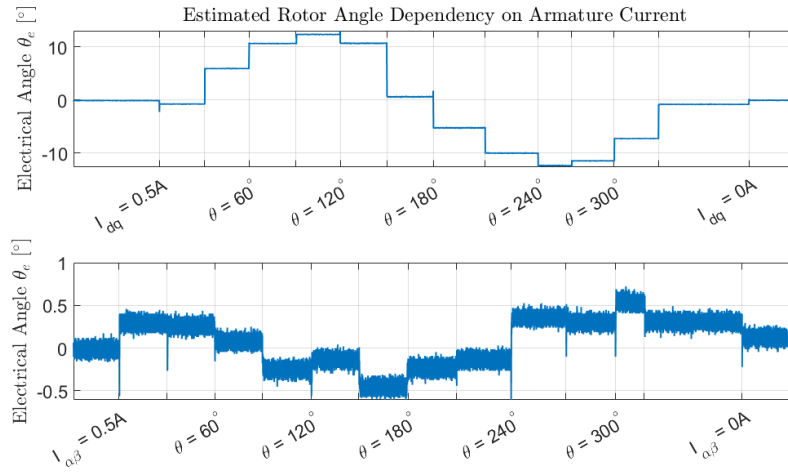

Figure 4.9: Dependency of Hall-based angle estimate on armature current.

To address these issues we implemented both variants of the back emf observer described in Chapter 2. The input values to the state observer are the transformed rotation current components $[i_{\alpha_4} \; i_{\beta_4}]^T$ and the reference rotation voltage commands $[v_{\alpha_4}^* \; v_{\beta_4}^*]^T$. Since the phase voltages applied to the motor terminals are pulse width modulated it is difficult to directly measure these voltages. Instead, the ideal voltage reference commands are used as inputs to the state observer.

A block diagram representation of the stationary and rotating frame observers are presented in Figures 2.4 and 2.5 respectively. The observers are implemented in the FPGA by replacing the continuous time integrator seen in the block diagrams with a trapezoidal integration block. The observers run at the current control loop rate i.e. twice the PWM switching frequency.

From the estimated back EMF signals the rotor angular position and speed information can be extracted using the PLL-based angle tracking scheme, described in Chapter 2. The estimated speed and angle are used in the speed feedback control loop and the rotational coordinate transformations respectively.

It should be noted that during steady-state operation the estimated angle output of the PLL seems to lead the measured angle in both simulations and reality. This phase difference grows in proportion to the rotor speed and is caused by discrete time delays in the system. This discrepancy between the estimated and actual angle causes suboptimal torque production and should be corrected to ensure optimal dynamic performance. To compensate for the effects of this discrete delay we use a simple angle prediction procedure that advances the estimated angle using the estimated steady-state speed as

$$\hat{\theta}_e[k+1] = \hat{\theta}_e[k] + \hat{\omega}_e[k] \cdot T_s$$

where T_s is the sampling time of the control loop. This simple compensation procedure ensures that in the next iteration of the control loop, the observer and PLL use an angle quantity $\hat{\theta}_e[k+1]$ that is more representative of the actual angle, rather than relying on old data from a previous iteration. By making this adjustment, we can improve the accuracy of the angle estimation and, consequently, enhance the overall performance of the system. Figure 4.10 demonstrates the effect of this procedure in correcting for the phase delay between the measured and estimated angles. The measurement is acquired while the rotor is levitated and rotating at 15 kRPM.

99
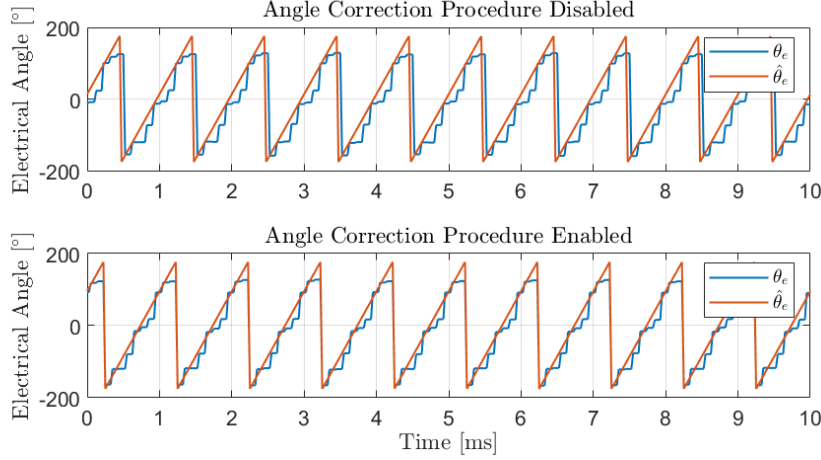
Figure 4.10: Effect of angle correction procedure.

The gain matrices L of the different observers were designed using the pole placement command **place()** in MATLAB. Due to the sinusoidal nature of the estimated back emf signals in the stationary reference frame, high bandwidth observers are required to successfully estimate these signals at high electrical speeds with a low amplitude attenuation and phase lag. However, tuning the observer to have an arbitrarily high bandwidth limits its ability to reject noise effectively. In contrast, the rotating frame observer estimates the back emf signals in the estimated rotor frame instead, where they appear as slowly varying DC quantities that are easy to track using low-bandwidth observers.

Pole locations of $p_1 = p_2 = -500$ rad/s were used for both observer implementations throughout testing. Placing the poles further left on the complex plane allows for a faster error convergence rate at the cost of larger initial estimation errors.

When testing the estimation performance of the two observer types, it was observed that large and abrupt transients in speed originating from a step change in the speed reference command would occasionally destabilize the estimated quantities. This effect was primarily observed when using the rotating frame observer.

We suspect this might be due to neglected terms in the model that have a nonnegligible effect during rapidly accelerating or transient conditions coupled with a circular dependency inherent to the rotating frame observer

implementation. The input currents and voltages to the rotating frame observer are expressed in the estimated rotor reference frame. Transforming these quantities from the stationary frame to the estimated reference frame is performed using the estimated output angle. However, large estimation errors during transients result in transformed currents and voltage which are not representative of the actual values. These inaccurate inputs are then used by the observer which further exacerbates the initial angle estimation error and could result in unpredictable behaviour which initiates an uncontrolled drift of the estimated quantities. This instability can be avoided by implementing a slew rate limit on the reference speed command. The stationary frame observer is more robust and immune to these transient conditions as the inputs to the observer are expressed in the stationary frame and does not exhibit this circular dependency on the estimated angle.

Testing at high speeds (>10 kRPM) was exclusively done using the rotating frame observer. Without altering the pole locations the stationary frame observer suffers from a degradation in performance at high speeds. Eventually, a point is reached where the estimated back emf signals are attenuated to the extent where the estimation fails altogether. Testing at low speeds was done using both variants but the stationary frame observer was often favoured due to a better transient performance for the reasons discussed earlier. A complementary usage combining the advantages of both observers may present a promising avenue for further investigation.

4.1.6   Synchronous Notch Filter

One of the advantages of an active magnetic bearing over passive solutions such as mechanical roller bearings, air foil bearings, and hydrodynamic bearings is the ability to actively alter rotor dynamics during runtime. One such use case is the ability to compensate for the effects of rotating unbalance. In rotating machines unbalance refers to the uneven distribution of mass around the axis of rotation. A rotor is said to be out of balance when its center of mass (inertia axis) is out of alignment with the center of rotation (geometric axis). This imbalance causes centrifugal forces that grow quadratically with speed, leading to unwanted mechanical stresses and vibrations.

Using active magnetic bearings we can mitigate the effects of rotor unbalance using two main approaches. The first approach aims to attenuate unbalance-induced bearing reaction forces by allowing the rotor to rotate about its inertial axis. The second approach aims to attenuate unbalance-induced vibrations by forcing the rotor to spin about its geometric axis.

The first approach is commonly used in applications that do not require precise rotation about the geometric axis provided that the available air gap is large enough to tolerate the resulting wobble. The second approach is better suited for applications requiring highly precise positioning but requires a high power demand to generate the necessary bearing forces and currents to compensate for unbalance-induced vibrations.

In our implementation, we utilize the first approach. The basic premise is to tolerate a rotor orbit instead of actively expending power to eliminate it. To achieve this we place a synchronous notch filter, similar to that proposed in [44], in the feedback path of the radial position control loop to selectively attenuate mass imbalance-induced bearing reaction forces. This allows for smoother operation and reduced actuator control effort. The continuous and discrete-time transfer functions of the implemented notch filter are given as

$$C(s) = \frac{s + \omega_0^2}{s^2 + \omega_v s + \omega_0^2} \xrightarrow{Tustin} C(z) = \frac{b_0 z^2 + b_1 z + b_2}{a_0 z^2 + a_1 z + a_2}$$

where ω_0 is the notch frequency, which is varied to match the rotor rotational frequency ω_m, and ω_v determines the Q-factor of the notch. A value of $\omega_v = 1$ rad/s was chosen through a trial and error approach and is used throughout testing. The filter coefficients are updated in real-time in the rotation control loop running at a 1kHz loop rate.

The notch filter is enabled at rotational frequencies above the designed suspension control bandwidth, i.e., for speeds above 60Hz or equivalently 3600 RPM. A brief analysis of the suspension open loop frequency response shows that enabling the notch filter at frequencies below the radial position controller crossover frequency interferes with the stability margins of the system and compromises the stability of the suspension regulation. As such, the use of the filter is limited to speeds beyond the designed suspension motion control bandwidth. In reference [23] the authors examine the effects of the notch filter on the closed-loop stability and propose a so-called generalized notch filter that maintains the stability regardless of speed. Compensation for the unbalance-induced effects can also be performed in the rotor synchronous reference frame as demonstrated in Chapter 3 of [14]. In theory, a notch filter can be realized using a high-pass filter implemented in the synchronous frame. However, this approach requires rotor angle information to transform the rotor radial position measurements to an equivalent representation in the rotating frame.

Table 4.2: Testing Conditions

Quantity	Value
DC-Link Voltage	30V
PWM Switching Frequency	20 kHz
PWM Deadtime	30 ns
Rotation Current Controller Bandwidth	1.5 kHz
Suspension Current Controller Bandwidth	0.6 kHz

4.2 Testing

We have conducted hardware tests for current regulation, rotor levitation, and rotation. Key testing conditions are listed in Table 4.2.

4.2.1 Current Regulation

The operation of the closed-loop current regulators was tested in isolation to assess their performance separately from the bearingless motor. Figure 4.11 shows the step response testing results for the rotation and suspension currents. These measurements were performed with the rotor centered and constrained using a plastic shim. The step responses were obtained with a current reference of $i_{q4}^* = i_{\alpha1}^* = 0.5$A.

To assess the rotation current regulator's behavior at different speeds, the rotation current step response was repeated at electrical speeds ω_e of 0 and 1000 Hz in an artificially rotating reference frame.

The proportional gains of the rotation and suspension current controllers were tuned to achieve current control bandwidths of 1.5kHz and 0.6kHz respectively. The first two plots of Figure 4.11 demonstrate that. The third plot shows a current fluctuation, which becomes more apparent at higher rotational speeds. We hypothesize that this is due to phase asymmetries in the manually wound phase windings.

A comparatively low suspension current control bandwidth was settled on to enhance its noise rejection capabilities and avoid unnecessary control actions leading to improved performance. For instance, detuning the suspension current controller decreased audible emissions, increased the available voltage margin for rotation enabling operation at higher speeds, and minimized large current control transients that could trigger a software-implemented
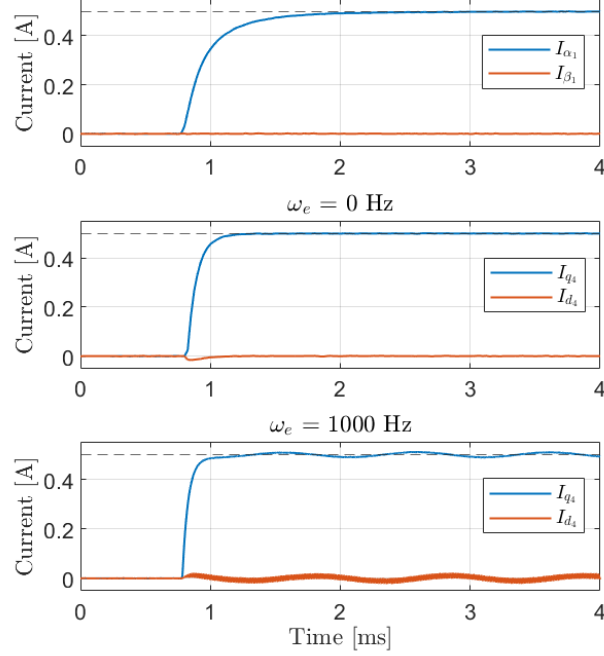
Figure 4.11: Current regulators step response test results.

overcurrent protection shutdown procedure.

We employed a simple overcurrent protection procedure that initiates a shutdown if the current exceeds some preset threshold. However, this simple approach often leads to premature triggering scenarios caused by short-lived transients. To address this issue, we considered using an "i squared t" (i2t) protection scheme that instead monitors power flow in the motor windings. This protection scheme works by continuously tracking the current flowing through the different phase windings and calculating a representation of the thermal energy generated by squaring the current (i) and integrating it over time (t). If the accumulated value exceeds a preset threshold, it triggers a shutdown mechanism to prevent the windings from overheating. However, implementing this protection scheme for all 12 measured phase currents requires significant FPGA logic resources, making it unfeasible for our specific setup. Alternatively, the same effect can be realized using physical fuses.

4.2.2 Bearingless Motor Operation

Stable levitation and rotation of the bearingless motor over a wide range of speeds has been demonstrated. Speeds of up to 36 kRPM or $\omega_e = 2400$ Hz have been achieved with a DC-Link voltage of 30 V. This represents an almost fourfold increase in the maximum no-load speed of 9500 r/min previously demonstrated using off-the-shelf power electronics and a DC-Link voltage of 48 V [72]. We believe this improvement in performance is due to a number of factors, such as decreased control loop latency, the ability to separately tune suspension and rotation current regulators, implementation of rotation current regulation in the synchronously rotating reference frame, enhanced current/voltage allocation procedure, and sensorless operation, all of which are enabled by the custom motor drive. The motor was spun up to its base speed which is limited by the available DC-link voltage. Without increasing the DC-link voltage, operation beyond those speeds requires a flux-weakening control strategy. In the following sections we demonstrate the different control strategies that were implemented.

Suspension Test

A radial position sensor calibration and rotor takeoff procedure is conducted prior to carrying out any tests. The startup procedure is outlined as follows

- The geometric center of the rotor is first established by centering the rotor using a 3d printed plastic shim. The measurements of the radial position sensors are recorded and used for a zero offset calibration

- The plastic shim is then swapped out for a thinner one leaving a sufficient air gap for the rotor to levitate. This shim serves to protect the sensors and stator iron in case of a rotor crash

- The capacitors are charged to the DC link voltage using the precharge routine described in Chapter 3

- A smooth takeoff procedure is initiated that lifts the rotor from its initial resting position to the approximate geometric center of the stator. This is done by gradually increasing the suspension lead compensator gain using a first order low pass filter with a time constant of 1 s

- Next the rotor is spun to a speed of around 1 kRPM. As the rotor is rotating and levitating the x and y reference positions are manually tuned to where the averaged suspension currents are approximately zero. This tuning process is repeated separately for each axis to ac-
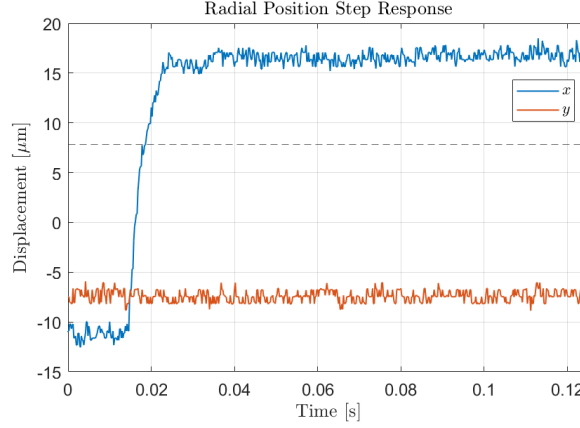
Figure 4.12: Radial displacement step response test results.

count for any offsets between the geometric center and magnetic center. The magnetic center represents an unstable equilibrium point where, in theory, no suspension currents are required to maintain the rotor position.

It is important to note that the sensor outputs were fairly consistent from day to day and that the calibration values did not require frequent updates.

A step response for the motor's radial displacement is presented in Figure 4.12. The dashed line indicates the reference command. The step response test is carried out while the rotor is not rotating. The suspension system exhibits a good transient response with an approximate 10%-90% rise time of $t_r = 5$ ms. This corresponds to a bandwidth of $f_{bw} = 50$ Hz using the approximate relation between rise time and bandwidth $2\pi f_{bw} \approx 2.2/t_r$. The absence of significant overshoot or oscillations in the response indicates sufficient stability margins.

Sensorless Operation

Use of the angle sensorless control scheme has enabled us to achieve higher speeds by freeing up voltage previously consumed to suppress noise due to Hall-based angle estimation error. This effect is clearly demonstrated in Figure 4.13. The figure plots the angle, rotation current, and rotation voltage while the motor is levitating and rotating at a speed of 15 kRPM. All measurements were sampled at the current control loop rate of 40kHz.

The first plot highlights the low sampling resolution and distortions present in the Hall-based angle measurement. The Hall-based angle measurements are updated at a 10kHz rate which corresponds to the frequency at which the Hall effect sensors are sampled. This sampling frequency is limited by the maximum aggregate sampling rate reported in the sbRIO controller datasheet (200 kHz). Since the board features a single ADC on which all of the signals are multiplexed, the maximum sampling rate per channel is obtained by dividing the maximum aggregate sampling rate by the number of channels being sampled. We are using a total of 6 differential channels which yields a maximum sampling rate per channel of approximately 33.4 kHz. This is in contrast to the observer-based angle estimate which updates at a 40kHz sampling rate.

The second and third plots demonstrate the transient response of the transformed rotation current measurements $[i_{d_4}\ i_{q_4}]$ and the rotation voltage magnitude $|v_{dq}| = \sqrt{v_{d_4}^2 + v_{q_4}^2}$ following a transition to sensorless control where the observer-based angle estimates are used for control. The transition point is marked with the dashed black line. Following the transition, a considerable reduction in the average and peak-to-peak voltage magnitude is evident. A similar reduction in the peak-to-peak currents particularly for the d-axis current can be seen. These improvements are attributed to the switch to sensorless control, which provides more accurate angle estimates, allowing for better voltage utilization and smoother motor operation at higher speeds.

Notch Filter

Figure 4.14 presents plots of the rotor orbit at various speeds, with and without the operation of the notch filter. The red dots indicate the operation with the filter enabled. Data are collected from the radial position sensors at a 5 kHz sampling rate. The notch filter restricts the suspension controller from reacting to unbalance forces synchronous to rotor speed and consequently frees up some voltage to be used for rotation. As demonstrated in Figure 4.14, the addition of the notch filter reduces the amplitude of the rotor orbit.

Figure 4.15 shows the suspension current transient response when the notch filter is enabled. Only the α- axis current is shown for visual clarity but a similar response can be seen in the β-axis current as well. The point at which the filter is enabled is marked with the dashed red line. This test was conducted at a rotor speed of 10 kRPM. The currents were sampled at

107
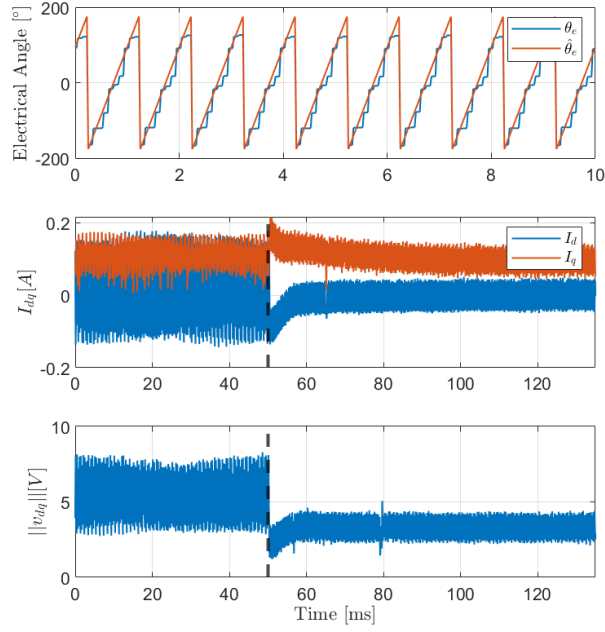
Figure 4.13: Sensorless control transient.
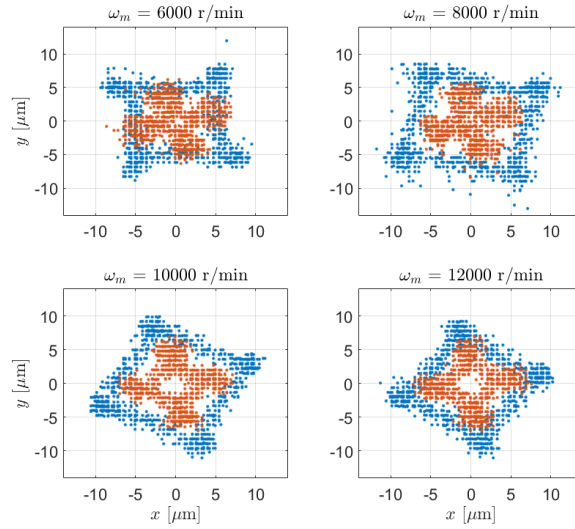
Figure 4.14: Measured rotor orbit at varying speeds. Red indicates the rotor orbit with the notch filter enabled.
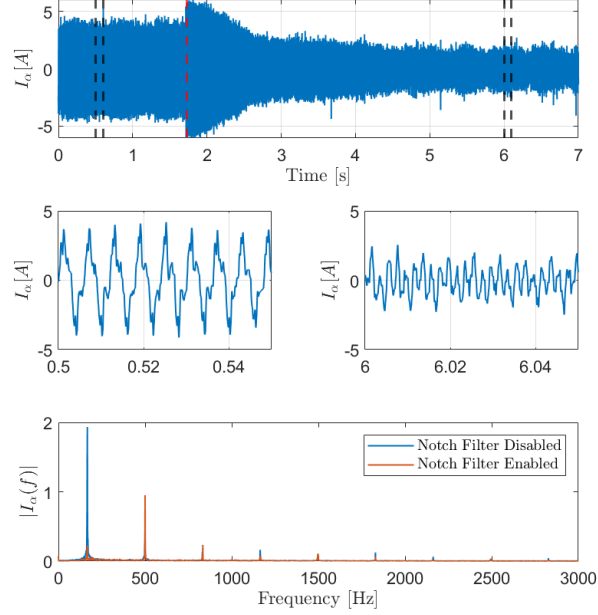
Figure 4.15: Suspension current transient response following activation of notch filter.

40 kHz. Upon enabling the filter, the peak-to-peak currents are reduced from approximately 8 A to 4 A following a transient response. The frequency spectrums of the steady state current prior to and following the activation of the filter demonstrate the attenuation of the synchronous current component at 10kRPM or equivalently 167 Hz. Interestingly, there seems to be a significant third harmonic component that requires further investigation.

The inclusion of the filter also led to a reduction in housing vibration, audible noise, and power consumption from the external DC link power supply during operation. The effects of the notch filter are less apparent at higher speeds where the limited suspension motion control bandwidth restricts its ability to respond to unbalance-induced effects.

Resource Allocation

To show the benefits of the proposed allocation procedure a rotational speed step response test was performed. The results are presented in Figure 4.16. The test was repeated using a static allocation procedure and the proposed allocation procedure. The speed reference was set to change from 3000 RPM to 4500 RPM. The maximum allowable current for this test was set at 6 A. For the static allocation, 1.25 A of the total allowable current is allocated for rotation leaving the rest for suspension. The stationary frame back emf observer was used for this test. The rotation currents were monitored during the speed transient to capture the differences in current allocation between the two methods. The rotational speed was sampled at 5 kHz while the rotation currents were sampled at 40 kHz.

With the proposed allocation procedure rotation currents of upwards to 4.7 A are conducted contrary to the static allocation procedure where the rotation current is limited to 1.25 A. This allows for a superior dynamic performance with faster rise and settling times for the rotational speed step response.

Therefore, we conclude that the proposed dynamic allocation procedure allows for a more efficient use of resources as it exploits the full potential of the combined winding scheme by maximally utilizing the entire winding slot space for torque or radial force production at all times. In contrast, using a static allocation, full utilization of the entire winding slot space is only achieved in the unlikely case when the suspension and rotation requirements are simultaneously maximized.

In addition to the improved dynamic performance, the proposed allocation procedure offers improved levitation stability under transient disturbances, albeit at the expense of torque generation.

To assess this, we conducted a test where the motor was operating close to its base speed, requiring high rotation voltages to overcome the rotational back emf voltage. The motor is then subjected to a sudden disturbance that increases the rotation voltage requirement by transitioning from angle sensorless operation to sensor-based operation. As a result of this transition, the total requested voltage exceeds the available DC link voltage. Under this circumstance, a conventional voltage limitation scheme would simply saturate the superimposed pole voltage references v_n^* in the stator fixed frame to $\pm V_{dc}/2$. However, this blind saturation approach will compromise the levitation stability as it distorts the requested suspension voltage vectors.
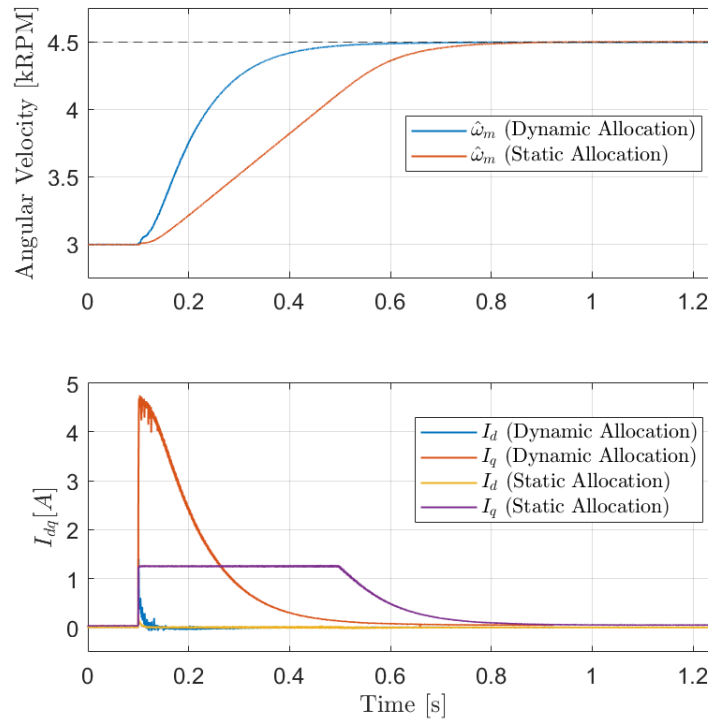
Figure 4.16: Rotational speed step response test with and without dynamic allocation procedure.

In contrast, the proposed allocation procedure separately saturates the suspension $v_{n_s}^*$ and rotation pole voltage reference $v_{n_r}^*$ components while prioritizing the suspension voltage demands. When subjected to the sudden disturbance, the proposed allocation procedure effectively limits the rotation voltage independently from the suspension voltage, preventing the superimposed pole voltage references from exceeding $\pm V_{dc}/2$. This results in decreased torque generation, as the rotation voltage falls below the rotational back emf voltage, and a subsequent drop in speed without compromising the levitation performance.

Testing confirmed these observations with the proposed allocation procedure, while the conventional voltage saturation scheme was not tested due to safety concerns regarding rotor crashes at high speeds.

Chapter 5

Conclusion and Future Work

In conclusion, this thesis presents the design of a reconfigurable motor drive that incorporates all electronic components needed for control, power, and sensing into a custom board developed for multiphase motor research.

The board features high and low-voltage sides physically separated by an isolation barrier. A 12-phase inverter topology was realized using GaNFET-based half-bridge power stages. The individual phase currents were monitored using an isolated inline sensing technique for control and protection purposes. An FPGA-based controller was used to implement a sophisticated motor control algorithm with high temporal determinism.

Successful operation of the motor drive was demonstrated with a prototype multiphase combined winding homopolar bearingless slice motor. The development of the board has enabled us to explore and implement different control strategies that would have not been possible otherwise. These strategies include the independent design and tuning of suspension and rotation current regulators as well as the use of sensorless control and synchronous notch filters to reduce actuator effort spent in suppressing sensor noise-induced artifacts and mass unbalance-induced effects respectively. Additionally, we outlined a dynamic current/voltage allocation procedure that optimizes resource utilization, thereby enhancing the overall capabilities of the bearingless motor without compromising its stability.

Use of these techniques has allowed the prototype motor to operate up to its base speed (36000 r/min) as limited by the available DC link voltage (30 V). This represents an almost fourfold increase in the maximum no-load speed of 9500 r/min reached when using off-the-shelf power electronics and a DC link voltage of 48 V.

5.1 Suggestions for Future Work

Future work will focus on extending the developed board's application to various bearingless motor architectures and leverage its flexibility to develop control strategies conducive to high-speed operation. Additionally, we aim to further explore different avenues in bearingless motor control such as sensorless control and flux weakening operation.

5.1.1 Application to Different Motor Architectures

Usage of the developed multiphase inverter board has brought about many performance improvements in the prototype bearingless slice motor, surpassing the outcomes achieved with standard off-the-shelf power electronics. However, we have tested the board only with homopolar motors where suspension operation is decoupled from the rotor angle allowing for a relatively simple and robust control strategy.

We aim to extend the application of the developed board to heteropolar bearingless motor architectures which require accurate real-time knowledge of the rotor angular position to achieve successful levitation. Specifically, we aim to use the developed board to control a dipole interior permanent magnet (IPM) bearingless slice motor developed by Taryn Loutit [38]. Several nonlinear phenomena were observed when controlling the IPM motor using off-the-shelf power electronics. The use of the multiphase inverter board offers access to crucial phase current feedback data which could aid in the investigation and mitigation of these phenomena.

5.1.2 Sensorless Control

Angle Estimation

Successful application of model-based sensorless control strategies was demonstrated at medium to high speeds. To enable complete sensorless operation we employed an open loop startup method which brings up the motor up to a speed where the model-based methods perform reliably.

However, as established earlier, heteropolar motors require accurate knowledge of the rotor's angular position across the motor's entire speed range to ensure stable levitation. Therefore, the use of an open-loop strategy is deemed unacceptable. This warrants the need for an angle estimation procedure that works reliably at low speeds and standstill conditions. To this end, saliency-based methods can be further investigated.

Radial Position Estimation

The radial position regulation also stands to benefit from a sensorless control strategy. In addition to cost savings and reduced hardware complexity brought about by eliminating the need for sensors, sensorless estimation of the radial positions would ensure a perfect collocation between the actuator and the sensor which eliminates the discrepancy between the magnetic and sensing axes.

Due to tolerances and imperfections in the fabrication process, the sensing axes do not necessarily coincide with the magnetic axes which represent the point through which the levitation forces act. If significant, this spatial discrepancy between the axes can lead to degradation in the performance and stability of the suspension control. These limitations sparked an investigation into the sensorless estimation of the rotor radial position using model-based methods. However as mentioned in Chapter 2, attempts at using the estimated signals for feedback control resulted in instability and require further investigation.

Moreover, these model-based methods are known to suffer from a number of shortcomings making them of limited practical use. For instance, they are unable to estimate the rotor's static/absolute position and are prone to instability with slight parameter variations and uncertainties. To address these issues there is ongoing research on alternative schemes providing robust estimation performance such as high-frequency injection methods.

5.1.3 Flux Weakening

The prototype bearingless motor was operated up to its base speed at which point the entire DC link voltage was fully utilized.

Operation beyond those speeds requires a flux-weakening control strategy. flux weakening is a key technique employed in motors to extend their operational range beyond their base speeds. flux weakening involves the partial cancellation of the motor's back electromotive force (EMF) by injecting negative i_d currents to reduce the flux linkage in the d-axis. This approach aims to maintain a voltage margin that allows for effective control of the stator currents. Operating in the flux weakening regime entails a trade-off between torque and speed, with a reduction in torque in exchange for increased rotational speed.

With combined winding bearingless motor the available DC link voltage

is distributed among the rotation and suspension subsystems. This makes defining a specific base speed somewhat ambiguous, as the voltage requirements for suspension are difficult to predict. Nonetheless, the base speed for some specific testing condition is assumed to occur at the point where the sum of the suspension and rotation voltage reference vectors is maximized as discussed in Chapter 4. This condition is repeated here as

$$\sqrt{{v_{\alpha_1}^*}^2 + {v_{\beta_1}^*}^2} + \sqrt{{v_{\alpha_4}^*}^2 + {v_{\beta_4}^*}^2} = V_{dc}/2$$

The development of the multiphase inverter board provides us with the capability to monitor the voltage reference signals, offering valuable insights into the point where the available DC link voltage is fully utilized. In contrast, when using standard off-the-shelf power electronics, we lack access to this information, making it more likely to surpass this point and operate in the saturation region which is detrimental to the stability of suspension operation. However, this risk is addressed by the proposed voltage allocation procedure. which enables safe operation up to the saturation point without compromising the suspension performance.

These developments represent a good initial step towards developing flux weakening control strategies for combined winding bearingless motors.

5.1.4   Digital Sensing of Rotor Angle

A digital sensing approach is used for measuring the phase currents, DC link voltage, and rotor radial position while analog hall effect sensors are used for sensing the rotor angle. A transition to an all-digital sensing approach would offer several benefits, including decreased susceptibility to noise and interference, increased processing flexibility in the digital domain, and increased sampling rates. One way to achieve this involves sampling the output voltage of the analog hall effect sensors via a sigma-delta modulator and replicating the existing digital SINC^3 filter to process the serial bitstream. However, this may require some signal conditioning to scale down the Hall sensor output voltage to a range accepted by the modulator. Alternatively, a simpler and more cost-effective solution involves replacing the analog Hall effect sensors with digital alternatives like those offered by Texas Instruments (DRV5057). However, these sensors have limited bandwidths (< 2000Hz) which could pose challenges for high-speed operation of motors with high pole numbers.

Bibliography

[1] Junichi Asama, Tadashi Fukao, Akira Chiba, Azizur Rahman, and Takaaki Oiwa. A design consideration of a novel bearingless disk motor for artificial hearts. In *2009 IEEE Energy Conversion Congress and Exposition*, pages 1693–1699, 2009.

[2] Karl Johan Åström and Tore Hägglund. *Advanced PID control*. ISA-The Instrumentation, Systems and Automation Society, 2006.

[3] Federico Barrero and Mario J. Duran. Recent advances in the design, modeling, and control of multiphase machines—part i. *IEEE Transactions on Industrial Electronics*, 63(1):449–458, 2016.

[4] Thomas Baumgartner, Ralph M. Burkart, and Johann W. Kolar. Analysis and design of a 300-w 500000-r/min slotless self-bearing permanent-magnet motor. *IEEE Transactions on Industrial Electronics*, 61(8):4326–4336, 2014.

[5] BiVACOR. This maglev heart could keep cardiac patients alive. https://spectrum.ieee.org/this-maglev-heart-could-keep-cardiac-patients-alive. Accessed Jul. 19, 2023.

[6] Eric Bogatin. *Signal and power integrity, simplified*. Prentice Hall, 2018.

[7] R. Bojoi, M. Pastorelli, J. Bottomley, P. Giangrande, and C. Gerada. Sensorless control of pm motor drives — a technology status review. In *2013 IEEE Workshop on Electrical Machines Design, Control and Diagnosis (WEMDCD)*, pages 168–182, 2013.

[8] S. Bolognani, L. Tubiana, and M. Zigliotto. Ekf-based sensorless ipm synchronous motor drive for flux-weakening applications. In *Conference Record of the 2002 IEEE Industry Applications Conference. 37th IAS Annual Meeting (Cat. No.02CH37344)*, volume 1, pages 112–119 vol.1, 2002.

[9] Łukasz Breńkacz, Łukasz Witanowski, Marta Drosińska-Komor, and Natalia Szewczuk-Krypa. Research and applications of active bearings: A state-of-the-art review. *Mechanical Systems and Signal Processing*, 151:107423, 2021.

[10] F. Briz, M.W. Degner, and R.D. Lorenz. Analysis and design of current regulators using complex vectors. *IEEE Transactions on Industry Applications*, 36(3):817–825, 2000.

[11] Jiahao Chen, Jingwei Zhu, and Eric L. Severson. Review of bearingless motor technology for significant power applications. *IEEE Transactions on Industry Applications*, 56(2):1377–1388, 2020.

[12] Zhiqian Chen, M. Tomita, S. Doki, and S. Okuma. An extended electromotive force model for sensorless control of interior permanent-magnet synchronous motors. *IEEE Transactions on Industrial Electronics*, 50(2):288–295, 2003.

[13] Song Chi, Zheng Zhang, and Longya Xu. Sliding-mode sensorless control of direct-drive pm synchronous motors for washing machine applications. *IEEE Transactions on Industry Applications*, 45(2):582–590, 2009.

[14] A. Chiba, Tadashi Fukao, Osamu Ichikawa, Masahide Oshima, Masatsugu Takemoto, and David G. Dorrel. *Magnetic Bearings and Bearingless Drives*. Newnes, Burlington, MA, 2005.

[15] Daniel J Clark, Mark J Jansen, and Gerald T Montague. An overview of magnetic bearing technology for gas turbine engines. 2004.

[16] Daniel Dietz and Andreas Binder. Comparison between a bearingless pm motor with separated and combined winding for torque and lateral force generation. In *2019 21st European Conference on Power Electronics and Applications (EPE '19 ECCE Europe)*, pages P.1–P.10, 2019.

[17] Mario J. Duran and Federico Barrero. Recent advances in the design, modeling, and control of multiphase machines—part ii. *IEEE Transactions on Industrial Electronics*, 63(1):459–468, 2016.

[18] Dan Eaton, John Rama, and Sumit Singhal. Magnetic bearing applications economics. In *2010 Record of Conference Papers Industry Applications Society 57th Annual Petroleum and Chemical Industry Conference (PCIC)*, pages 1–9, 2010.

[19] Robert W Erickson and Dragan Maksimovic. *Fundamentals of power electronics*. Springer Science & Business Media, 2007.

[20] Filip Filipovic, Milutin Petronijevic, Nebojsa Mitrovic, Bojan Bankovic, and Vojkan Kostić. Current sampling techniques for digitally controlled inverters. 09 2019.

[21] Wolfgang Gruber. Bearingless slice motors: General overview and the special case of novel magnet-free rotors. In *Innovative Small Drives and Micro-Motor Systems; 9. GMM/ETG Symposium*, pages 1–6, 2013.

[22] Jiangbiao He, Tiefu Zhao, Xin Jing, and Nabeel A.O. Demerdash. Application of wide bandgap devices in renewable energy systems - benefits and challenges. In *2014 International Conference on Renewable Energy Research and Application (ICRERA)*, pages 749–754, 2014.

[23] R. Herzog, P. Buhler, C. Gahler, and R. Larsonneur. Unbalance compensation using generalized notch filters in the multivariable feedback of magnetic bearings. *IEEE Transactions on Control Systems Technology*, 4(5):580–586, 1996.

[24] Hideo Hoshi, Tadahiko Shinshi, and Setsuo Takatani. Third-generation blood pumps with mechanical noncontact magnetic bearings. *Artificial organs*, 30 5:324–38, 2006.

[25] Yizhou Hua and Huangqiu Zhu. Sensorless control of bearingless permanent magnet synchronous motor based on ls-svm inverse system. *Electronics*, 10(3):265, 2021.

[26] O. Ichikawa, A. Chiba, and T. Fukao. Inherently decoupled magnetic suspension in homopolar-type bearingless motors. *IEEE Transactions on Industry Applications*, 37(6):1668–1674, 2001.

[27] Texas Instruments. Combining the ads1202 with an fpga digital filter for current measurement in motor control applications. https://www.ti.com/lit/an/sbaa094/sbaa094.pdf?ts=1686753456202. Accessed Jul. 19, 2023.

[28] Rafal P. Jastrzebski, Pekko Jaatinen, Olli Pyrhönen, and Akira Chiba. Design of 6-slot inset pm bearingless motor for high-speed and higher than 100kw applications. In *2017 IEEE International Electric Machines and Drives Conference (IEMDC)*, pages 1–6, 2017.

[29] ME F Kasarda. An overview of active magnetic bearing technology and applications. *The shock and vibration digest*, 32(2):91–99, 2000.

[30] J.W. Kelly, E.G. Strangas, and J.M. Miller. Multi-phase inverter analysis. In *IEMDC 2001. IEEE International Electric Machines and Drives Conference (Cat. No.01EX485)*, pages 147–155, 2001.

[31] W. K. S. Khoo, K. Kalita, and S. D. Garvey. Practical implementation of the bridge configured winding for producing controllable transverse forces in electrical machines. *IEEE Transactions on Magnetics*, 47(6):1712–1718, 2011.

[32] Myoungho Kim and Seung-Ki Sul. An enhanced sensorless control method for pmsm in rapid accelerating operation. In *The 2010 International Power Electronics Conference - ECCE ASIA -*, pages 2249–2253, 2010.

[33] E. Levi, R. Bojoi, F. Profumo, H. A. Toliyat, and S. Williamson. Multiphase induction motor drives – a technology status review. *IET Electric Power Applications*, 1(4):489–516, Jul 2007.

[34] Emil Levi, Radu Bojoi, Francesco Profumo, HA Toliyat, and S Williamson. Multiphase induction motor drives–a technology status review. *IET Electric Power Applications*, 1(4):489–516, 2007.

[35] Levitronix. Ultrapure fluid handling integrated pump system series. https://www.levitronix.com/media-center/technical-brochure-bps-i600-2/. Accessed Jul. 19, 2023.

[36] Zongwei Liu, Akira Chiba, Yusuke Irino, and Yuji Nakazawa. Optimum pole number combination of a buried permanent magnet bearingless motor and test results at an output of 60 kw with a speed of 37000 r/min. *IEEE Open Journal of Industry Applications*, 1:33–41, 2020.

[37] Taryn Loutit and Minkyun Noh. Design of a dipole internal permanent magnet bearingless motor for flux-weakening control. In *2022 IEEE Energy Conversion Congress and Exposition (ECCE)*, pages 1–8, 2022.

[38] Taryn Elizabeth Loutit. Design and implementation of a dipole bearingless slice motor for flux-weakening applications. Master's thesis, University of British Columbia, 2022.

[39] Krunal Maniar. Comparing shunt- and hall-based isolated current-sensing solutions in hev/ev. Available at `https://www.ti.com/lit/an/sbaa293b/sbaa293b.pdf?ts=1610006777503` (2021/01/20).

[40] Eric H Maslen, Gerhard Schweitzer, Hannes Bleuler, and Matthew Cole.

Magnetic bearings: theory, design, and application to rotating machinery. Springer, 2009.

[41] Brendan Peter McGrath and Donald Grahame Holmes. A general analytical method for calculating inverter dc-link current harmonics. *IEEE Transactions on Industry Applications*, 45(5):1851–1859, 2009.

[42] Narendra Mehta. Gan fet module performance advantage over silicon. Available at `https://www.ti.com/lit/wp/slyy071/slyy071.pdf?ts=1609996598044` (2021/01/20).

[43] José Millán, Philippe Godignon, Xavier Perpiñà, Amador Pérez-Tomás, and José Rebollo. A survey of wide bandgap power semiconductor devices. *IEEE Transactions on Power Electronics*, 29(5):2155–2163, 2014.

[44] Hubert Mitterhofer, Wolfgang Gruber, and Wolfgang Amrhein. On the high speed capacity of bearingless drives. *IEEE Transactions on Industrial Electronics*, 61(6):3119–3126, 2014.

[45] T Mizuno and H Bleuler. Self-sensing magnetic bearing control system design using the geometric approach. *Control Engineering Practice*, 3(7):925–932, 1995.

[46] S. Morimoto, K. Kawamoto, M. Sanada, and Y. Takeda. Sensorless control strategy for salient-pole pmsm based on extended emf in rotating reference frame. *IEEE Transactions on Industry Applications*, 38(4):1054–1061, 2002.

[47] Ajay Kumar Morya, Matthew C. Gardner, Bahareh Anvari, Liming Liu, Alejandro G. Yepes, Jesús Doval-Gandoy, and Hamid A. Toliyat. Wide bandgap devices in ac electric drives: Opportunities and challenges. *IEEE Transactions on Transportation Electrification*, 5(1):3–20, 2019.

[48] Gabriel Munteanu, Andreas Binder, and Tobias Schneider. Loss measurement of a 40 kw high-speed bearingless pm synchronous motor. In *2011 IEEE Energy Conversion Congress and Exposition*, pages 722–729, 2011.

[49] Heng Nian, Yikang He, Dong Chen, and Lei Huang. Self-sensing of the rotor position and displacement for an inset permanent magnet type bearingless motor. In *2007 International Conference on Electrical Machines and Systems (ICEMS)*, pages 1508–1512, 2007.

[50] Heng Nian, Yu Quan, and Jiawen Li. Rotor displacement sensorless control strategy for pm type bearingless motor based on the parameter identification. In *2009 International Conference on Electrical Machines and Systems*, pages 1–5, 2009.

[51] FNU Nishanth, Anvar Khamitov, and Eric L. Severson. Design of multiphase motor windings for control of multiple airgap fields. In *2022 IEEE Energy Conversion Congress and Exposition (ECCE)*, pages 1–8, 2022.

[52] M. Noh and D. L. Trumper. Homopolar bearingless slice motor with flux-biasing halbach arrays. *IEEE Transactions on Industrial Electronics*, 67(9):7757–7766, 2020.

[53] Minkyun Noh. Homopolar bearingless slice motor for improved power density. Master's thesis, Massachusetts Institute of Technology, 2018.

[54] Minkyun Noh, Wolfgang Gruber, and David L. Trumper. Hysteresis bearingless slice motors with homopolar flux-biasing. *IEEE/ASME Transactions on Mechatronics*, 22(5):2308–2318, 2017.

[55] Minkyun Noh, Wolfgang Gruber, and David L. Trumper. Low-cost eddy-current position sensing for bearingless motor suspension control. In *2017 IEEE International Electric Machines and Drives Conference (IEMDC)*, pages 1–6, 2017.

[56] Ryohei Oishi, Satoshi Horima, Hiroya Sugimoto, and Akira Chiba. A novel parallel motor winding structure for bearingless motors. *IEEE Transactions on Magnetics*, 49(5):2287–2290, 2013.

[57] Henry W. Ott. *PCB Layout and Stackup*, page 622–655. Wiley-Blackwell, 2009.

[58] Mario Pacas. Sensorless drives in industrial applications. *IEEE Industrial Electronics Magazine*, 5(2):16–23, 2011.

[59] L. Parsa. On advantages of multi-phase machines. In *31st Annual Conference of IEEE Industrial Electronics Society, 2005. IECON 2005.*, pages 6 pp.–, 2005.

[60] L. Parsa and H.A. Toliyat. Five-phase permanent-magnet motor drives. *IEEE Transactions on Industry Applications*, 41(1):30–37, 2005.

[61] Tonghao Pei, Dawei Li, Jiayun Liu, Jian Li, and Wubin Kong. Re-

view of bearingless synchronous motors: Principle and topology. *IEEE Transactions on Transportation Electrification*, 8(3):3489–3502, 2022.

[62] Pascal Puentener, Marcel Schuck, Daniel Steinert, Thomas Nussbaumer, and Johann Walter Kolar. A 150 000-r/min bearingless slice motor. *IEEE/ASME Transactions on Mechatronics*, 23(6):2963–2967, 2018.

[63] K. Raggl, J. W. Kolar, and T. Nussbaumer. Comparison of winding concepts for bearingless pumps. In *2007 7th Internatonal Conference on Power Electronics*, pages 1013–1020, 2007.

[64] Seppo E. Saarakkala, Victor Mukherjee, Maksim Sokolov, Marko Hinkkanen, and Anouar Belahcen. Analytical model including rotor eccentricity for bearingless synchronous reluctance motors. In *2018 XIII International Conference on Electrical Machines (ICEM)*, pages 1388–1394, 2018.

[65] Reto Schoeb and Natale Barletta. Principle and application of a bearingless slice motor. *Jsme International Journal Series C-mechanical Systems Machine Elements and Manufacturing*, 40:593–598, 1997.

[66] Eric Severson, Srikant Gandikota, and Ned Mohan. Practical implementation of dual purpose no voltage drives for bearingless motors. In *2015 IEEE Applied Power Electronics Conference and Exposition (APEC)*, pages 819–826, 2015.

[67] Eric Severson, Robert Nilssen, Tore Undeland, and Ned Mohan. Design of dual purpose no voltage combined windings for bearingless motors. In *2016 IEEE Energy Conversion Congress and Exposition (ECCE)*, pages 1–10, 2016.

[68] Eric L Severson. Bearingless motor technology for industrial and transportation applications. In *2018 IEEE Transportation Electrification Conference and Expo (ITEC)*, pages 266–273, 2018.

[69] Maksim Sokolov, Wolfgang Gruber, Seppo E. Saarakkala, and Marko Hinkkanen. Modeling of a bearingless synchronous reluctance motor with combined windings. In *2019 IEEE Energy Conversion Congress and Exposition (ECCE)*, pages 7084–7090, 2019.

[70] Seung-Ho Song, Jong-Woo Choi, and Seung-Ki Sul. Current measurements in digitally controlled ac drives. *IEEE Industry Applications Magazine*, 6(4):51–62, 2000.

[71] Bingyao Sun. Third quadrant operation of gan. Available at `https://www.ti.com/lit/an/snoaa36/snoaa36.pdf`.

[72] Simon Szoke. Homopolar bearingless slice motor for improved power density. Master's thesis, University of British Columbia, 2022.

[73] Simon Szoke and Minkyun Noh. Homopolar bearingless slice motor with quadruple three-phase windings. In *2022 IEEE Energy Conversion Congress and Exposition (ECCE)*, pages 1–6, 2022.

[74] M. Takemoto, A. Chiba, and T. Fukao. A method of determining advanced angle of square-wave currents in bearingless switched reluctance motors. In *Conference Record of the 2000 IEEE Industry Applications Conference. Thirty-Fifth IAS Annual Meeting and World Conference on Industrial Applications of Electrical Energy (Cat. No.00CH37129)*, volume 1, pages 241–248 vol.1, 2000.

[75] T. Tera, Y. Yamauchi, A. Chiba, T. Fukao, and M.A. Rahman. Performances of bearingless and sensorless induction motor drive based on mutual inductances and rotor displacements estimation. *IEEE Transactions on Industrial Electronics*, 53(1):187–194, 2006.

[76] Dieter Vischer. A new approach to sensorless and voltage controlled ambs based on network theory concepts. In *Proc. 2nd Int. Symp. on Magnetic Bearings, 1990*, 1990.

[77] Marija Vujacic, Obrad Dordevic, and Gabriele Grandi. Evaluation of dc-link voltage ripple in seven-phase pwm voltage source inverters. In *2018 IEEE International Telecommunications Energy Conference (INTELEC)*, pages 1–6, 2018.

[78] Marija Vujacic, M Hammami, O Dordevic, and Gabriele Grandi. Evaluation of dc-link voltage ripple in five-phase pwm voltage source inverters. *The Journal of Engineering*, 2019(17):3709–3714, 2019.

[79] Marija Vujacic, Manel Hammami, Milan Srndovic, and Gabriele Grandi. Analysis of dc-link voltage switching ripple in three-phase pwm inverters. *Energies*, 11(2):471, 2018.

[80] Gaolin Wang, Zhuomin Li, Guoqiang Zhang, Yong Yu, and Dianguo Xu. Quadrature pll-based high-order sliding-mode observer for ipmsm sensorless control with online mtpa control strategy. *IEEE Transactions on Energy Conversion*, 28(1):214–224, 2013.

[81] Bernhard Warberger, Remo Kaelin, Thomas Nussbaumer, and Johann W. Kolar. 50-N · m/2500-w bearingless motor for high-purity pharmaceutical mixing. *IEEE Transactions on Industrial Electronics*, 59(5):2236–2247, 2012.

[82] Xiaoting Ye and Zebin Yang. Development of bearingless induction motors and key technologies. *IEEE Access*, 7:121055–121066, 2019.

[83] Yue Zhao, Chun Wei, Zhe Zhang, and Wei Qiao. A review on position/speed sensorless control for permanent-magnet synchronous machine-based wind energy conversion systems. *IEEE Journal of Emerging and Selected Topics in Power Electronics*, 1(4):203–216, 2013.